Czech Technical University in Prague

Faculty of Electrical Engineering
Department of Electromagnetic Field

Interference of Coherent Signals in Microwave Measurements

Doctoral Thesis

Martin Haase

Prague, January 2020

Ph.D. Programme: (P2612) Electrical Engineering and Information Technology
Branch of study: (2601V010) Radioelectronics

Supervisor: *Prof. Ing. Karel Hoffmann, CSc.*

Declaration

I hereby declare I have written this thesis independently and quoted all the sources of information used in accordance with methodological instructions on ethical principles for writing an academic thesis. Moreover, I state that this thesis has neither been submitted nor accepted for any other degree.

In Prague, January 2020

.....
Martin Haase

Acknowledgements

I would like to thank prof. Ing. Karel Hoffmann, CSc. for allowing me to participate in his scientific activities, which highly broadened mine expert knowledge in the field of microwave measurements, and most importantly for supporting me on my way towards the Ph.D. degree. Further, a special gratitude belongs to my family, especially to my wife, without whose support I would not probably finish the thesis. At last but not least, I would like to thank all members and students of the Department of Electromagnetic Field for friendly environment.

Abstrakt

Práce se primárně zabývá mikrovlnnými měřeními, která jsou ovlivněna interferencemi koherentních signálů. Konkrétně se věnuje dvěma typům mikrovlnných měření – měření interferenčních filtrů (EMI/RFI) a měření extrémních impedancí založeném na interferometrických měřicích přístupech. Nová metoda pro charakterizaci nejmenšího možného útlumu EMI/RFI filtrů v jejich závěrném pásmu na vyšších megahertzových a gigahertzových kmitočtech je vyvinuta a experimentálně ověřena na profesionálním EMI/RFI filtru. Dále, je odvozena originální nejistotní analýza interferometrických měření extrémních impedancí, odhalující základní limity ovlivňující dosažitelnou přesnost měření. Výsledky analýzy jsou ověřeny pomocí synteticky vygenerovaných měření v prostředí programu MATLAB.

Klíčová slova: Aditivní šum, diferenční vid, elektromagnetický interferenční filter (EMI), extrémní impedance, interferometrická metoda, mikrovlnné měření, Monte Carlo simulace, multiplikativní šum, nejistotní analýza, potlačení nejistoty, radio-frekvenční interferenční filtr (RFI), Souhlasný vid, S-parametry.

Abstract

The thesis is primarily focused on microwave measurements that are influenced by the interference of coherent signals. Specifically, it investigates two different microwave measurements – measurements of electromagnetic interference (EMI) or radio-frequency interference (RFI) filters and measurements of extreme impedances based on interferometric measurement approaches. A new method for characterization of lowest possible insertion loss of EMI/RFI filters in their stop bands at high megahertz or gigahertz frequencies is developed and experimentally verified on a professional EMI/RFI filter. Further, an uncertainty analysis of interferometric measurements of extreme impedances, revealing fundamental limits influencing achievable measurement accuracy and precision, is presented and verified using synthetically generated measurements in MATLAB environment.

Keywords: Additive noise, common mode (CM), differential mode (DM), electromagnetic interference (EMI) filter, extreme impedances, interferometric method, microwave measurement, mixed-modes, Monte Carlo simulation, multiplicative noise, radio-frequency interference (RFI) filter, S-parameters, uncertainty analysis, uncertainty suppression.

List of Author's Publications

Unless explicitly noted, the authorship is divided equally among the listed authors.

Papers in journals with impact factor

- **M. Haase [34 %]**, K. Hoffmann [33 %], and P. Hudec [33 %], "General Method for Characterization of Power-Line EMI/RFI Filters Based on S-Parameter Evaluation", *IEEE Trans. Electromagn. Compat.*, vol. 58, no. 5, pp. 1465-1474, July 2016, IF: 1.658

- **M. Haase [34 %]**, K. Hoffmann [33 %], and P. Hudec [33 %], "Advanced Evaluation of Minimum Insertion Loss of Power-Line EMI/RFI Filters in RF and Microwave Frequency Bands", *IEEE Trans. Electromagn. Compat.*, vol. 59, no. 6, pp. 1887-1896, May 2017, IF: 1.52

Conference papers

- **M. Haase** and K. Hoffmann, "Study of calibration standards for extreme impedances measurement," *83rd ARFTG Microw. Meas. Conf.*, Tampa, FL, pp. 1-6, Jun. 2014.

- **M. Haase [34 %]**, K. Hoffmann [33 %], and Z. Skvor [33 %], "Microstrip open — Problematic calibration standard," *85th ARFTG Microw. Meas. Conf.*, Phoenix, AZ, pp. 1-4, May 2015.

- **M. Haase** and K. Hoffmann, "Mikrovlnná měření extrémních impedancí," *42. Seminář Pravidelné setkání zájemců o mikrovlnnou techniku*, Praha, Květen 2015.

- **M. Haase** and K. Hoffmann, "Calibration/Verification Standards for Measurement of Extremely High Impedances," *86th ARFTG Microw. Meas. Conf.*, Atlanta, GA, pp. 83-86, Dec. 2015.

- **M. Haase [34 %]**, K. Hoffmann [34 %], and M. Hudlicka [32 %], "Traceable high impedance calibration standards," *87th ARFTG Microw. Meas. Conf.*, San Francisco, CA, May 2016.

Conference paper not related to this work

- **M. Haase** and K. Hoffmann, "Transistor oscillator 24.7 GHz stabilized by HEM221 mode of rectangular dielectric resonator," *COMITE Conf. on Microw. Techniques*, Pardubice, pp. 62-64, Apr. 2013.

Paper being currently reviewed in journal with an impact factor

- **M. Haase** and K. Hoffmann, "Uncertainty Analysis of Microwave Measurement of Extreme Impedances," *IEEE Trans. Microw. Theory Techn.*.

Financial support acknowledgement

The research presented in the listed papers was conducted under partial financial support of these projects:

- European Metrology Research Programme (EMRP) - Project 'SIB62 Metrology for New Electrical Measurement Quantities in High-frequency Circuits'. The EMRP is jointly funded by the EMRP participating countries within EURAMET and the European Union. (http://projects.npl.co.uk/hf-circuits/)
- SGS13/198/OHK3/3T/13 - Artificially Prepared High-frequency Materials and Structures
- SGS16/226/OHK3/3T/13 - Investigation on High-Frequency Electromagnetic Structures

Awards

Martin Haase received an award for: The second prize in the best student paper presented, on COMITE, April 2013.

Contents

List of abbreviations

AB	Amplification box
AWR MO	AWR Microwave Office
CM	Common mode
CM→CM	Common mode to common mode transmission
CM→DM	Common mode to differential mode conversion
DM	Differential mode
DM→DM	Differential mode to differential mode transmission
DM→CM	Differential mode to common mode conversion
DUT	Device under test
EMI	Electromagnetic interference
H1, H2	Ideal 180° hybrids
IB	Interferometric box
LNA	Low noise amplifier
LUP	Law of uncertainty propagation
MCS	Monte Carlo Simulations
NSMM	Near-Field Scanning Microwave Microscopy
PD_a, PD_b	Ideal in-phase and out-of-phase power dividers
RFI	Radio-frequency interference
SM	Single-ended mode
S-matrix	Scattering matrix
S-parameters	Scattering parameters
VNA	Vector Network Analyzer

List of used symbols

Symbol	Quantity
a_i, b_i	SM standard normalized waves
a_{ci}, a_{di}	Mixed-mode a-waves
$a_{1\mathrm{R}}$	SM wave in VNA reference channel
A	losses of the Γ_x path inside the **IB**
A_i, B_i	SM standard normalized waves
b_{ci}, b_{di}	Mixed-mode b-waves
C_1, C_2, C_3	Calibration/error constants
D_1, D_2, D_3, D_4	Complex constants needed for degenerated matrix $\boldsymbol{S}^{\mathrm{D41}}$ derivation
E_q, F_q, D	Complex constants needed for Γ_{Gw} and Γ_{Lw} computation
f	Frequency
G	Transmission coefficient S_{21}^{AB} of the **AB**
G_t	Transducer gain
G_{tmax}	Maximum available gain
H_t, H_s, H_{st}, H_{ts}	Auxiliary complex constants needed for derivation of general degenerated matrix $\boldsymbol{S}^{\mathrm{D}ji}$
IL_{50}	Insertion loss corresponding to $Z_\mathrm{G} = Z_\mathrm{L} = 50\ \Omega$
IL, IL^{ji}	Operational insertion loss
$IL_{\mathrm{CC}}, IL_{\mathrm{DD}}$	IL of a filter in terms of CM→CM and DM→DM
$IL_{\mathrm{DC}}, IL_{\mathrm{CD}}$	IL of a filter in terms of CM→DM and DM→CM
$IL_{\mathrm{min}}, IL_{\mathrm{min}}^{ji}$	Minimum value of the insertion loss determined according to 3.1.2
$IL_{\mathrm{minCC}}, IL_{\mathrm{minDD}}$	IL_{min} of a filter in terms of CM→CM and DM→DM
$IL_{\mathrm{minCD}}, IL_{\mathrm{minDC}}$	IL_{min} of a filter in terms of CM→DM and DM→CM
IL_{minE}	Experimentally achieved minimum insertion loss
$IL_{\mathrm{minW}}, IL_{\mathrm{minW}}^{ji}$	Worst-case minimum possible value of the insertion loss determined according to 3.1.3
IL_M	Measured insertion loss
IL_{Limit}	Measured noise floor expressed in the form of maximum measurable insertion loss
$\mathbf{J}\,(Y)$	General jacobian matrix of complex quantity Y
k	Stability factor
$\boldsymbol{M}$	Transformation matrix needed for $\boldsymbol{S}^{\mathrm{mix}}$ derivation
N_H	High-level multiplicative noise
N_L	Low-level additive noise
$N_\mathrm{L}^{\mathrm{AB}}$	Noise generated at the output of the **AB**
$N_\mathrm{L}^{\mathrm{IB}}$	Noise generated at the output of the **IB**
$N_\mathrm{L}^{\mathrm{R}}, N_\mathrm{L}^{\mathrm{T}}$	Additive sources of noise in the VNA reference and test channel
$\mathrm{p}_{43\mathrm{a}}, \mathrm{p}_{43\mathrm{b}}$	Mixed-mode ports
P_{AG}	Available power from the source
P_L	Delivered power to the load
S_1, S_2, S_3	True values of calibration standards
S_{ji}^{AB}	Scattering parameters of the **AB**
S_{ji}^{cas}	Scattering parameters of $\boldsymbol{S}^{\mathrm{cas}}$
$S^{\mathrm{D}ji}$	Scattering parameters of $\boldsymbol{S}^{\mathrm{D}ji}$

Symbol	Quantity
S_{ji}^{IB}	Scattering parameters of the **IB**
$S_{21}^{\mathrm{AB}'}$	Transmission coefficient of **AB** including the impedance mismatch at its respective port 1
$S_{21}^{\mathrm{IB}'}$	Small subtractive signal created by **IB** with respect to the 50-Ω impedance at its respective port 2
S_{ref}	Interfering signal
S^{HW}	Suppression limit given by **IB** and **AB** hardware
S^{IB}	Suppression limit given by **IB** hardware
S^{VNA}, S^{Noise}	Suppression coefficient
$\boldsymbol{S}^{\mathrm{H}}$	Single-ended S-matrix of an ideal 180° hybrid
$\boldsymbol{S}^{\mathrm{IP}}$	Single-ended S-matrix of an in-phase power divider
$\boldsymbol{S}^{\mathrm{OP}}$	Single-ended S-matrix of an out-of-phase power divider
$\boldsymbol{S}^{\mathrm{filter}}$	Single-ended S-matrix of a filter
$\boldsymbol{S}^{\mathrm{cas}}$	Single-ended S-matrix of the H1-filter-H2 cascade
$\boldsymbol{S}^{\mathrm{mix}}$	Mixed-mode S-matrix
$\boldsymbol{S}^{\mathrm{D}ji}$	Degenarated S-matrix
$\boldsymbol{S}^{ji}$	S-matrix with reduced indices
T_{21}	Transmission coefficient
T_{21}^{G}	General transmission coefficient
$T_{21}^{'}$	Simplified transmission coefficient
u	"Complex" uncertainty
$u\left(a\right)$	Uncertainty in the real part of Y
$u\left(b\right)$	Uncertainty in the imaginary part of Y
$u\left(a,b\right)=u\left(b,a\right)$	Correlation between the real and imaginary parts of Y
u_{DUT}	Resulting complex DUT uncertainty
u_{MR}	Complex uncertainty given by the finite mounting repeatability of standard/DUT connection
u_{N}	Complex uncertainty caused by the phase noise N_{H}
u_{S}	Complex uncertainty caused by the characterization of calibration standards N_{H}
u_{VNA}	Complex uncertainty caused by the VNA reference channel and the VNA receiver in the test channel
U	Expanded uncertainty corresponding to coverage factor value of three
$\mathbf{V}\left(Y\right)$	General variance-covariance matrix of complex quantities Y
$\tilde{\mathbf{V}}\left(Y\right)$	Rotation of the joint probability distribution, given by variance-covariance matrix $\mathbf{V}\left(Y\right)$
$\mathbf{V}\left(a_{1\mathrm{R}}\right)$	Variance-covariance matrix characterizing the uncertainty caused by the VNA reference channel
$\mathbf{V}\left(N_{\mathrm{H}}\right)$	Variance-covariance matrix characterizing phase noise at the VNA port 1
$\mathbf{V}\left(N_{\mathrm{L}}\right)$	Variance-covariance matrix characterizing the noise floor at the VNA port 1
$\mathbf{V}\left(N_{\mathrm{L}}^{\mathrm{AB}}\right)$	Variance-covariance matrix characterizing the noise generated at the **AB** respective port 2

Symbol	Quantity
$\mathbf{V}\left(N_{\mathrm{L}}^{\mathrm{IB}}\right)$	Variance-covariance matrix characterizing the noise generated at the **IB** respective port 2
$\mathbf{V}\left(N_{\mathrm{L}}^{\mathrm{T}}\right)$	Variance-covariance matrix characterizing the uncertainty of the VNA receiver in the test channel
$\mathbf{V}\left(T_{21}^{'}\right)$	Variance-covariance matrix characterizing the uncertainty of $T_{21}^{'}$
$\mathbf{V}^{\mathrm{VNA}}$	Variance-covariance matrix characterizing the uncertainty caused by the VNA reference channel and the VNA receiver in the test channel
$\mathbf{V}\left(\Gamma_{\mathrm{x}}\right)$	Variance-covariance matrix characterizing the uncertainty of measured Γ_{x}/DUT
$\mathbf{V}^{\mathrm{MR}}\left(\Gamma_{\mathrm{x}}\right)$	Variance-covariance matrix characterizing the uncertainty caused by the finite mounting repeatability of Γ_{x}/DUT connection
$\mathbf{V}^{\mathrm{S}}\left(\Gamma_{\mathrm{x}}\right)$	Variance-covariance matrix characterizing the uncertainty caused by calibration standards characterization
W_{MR}, W_S	Sensitivity coefficients
$\mathbf{x}$	Input quantities influencing $T_{21}^{'}$
$\mathbf{x}_1$	Input quantities suffering from uncertainties $\mathbf{x}_1 \subseteq \mathbf{x}$
Y	complex quantity $Y = a + jb$
$Y \sim N_2\left(\mu, \mathbf{V}\right)$	Bivariate Gaussian distribution of Y described by mean vector μ and variance-covariance matrix $\mathbf{V}$
Z_0	Characteristic impedance of a transmission line
$Z_{\mathrm{G}}, Z_{\mathrm{L}}$	General input (source) and output (load) impedances
Z_{ref}	Reference impedance
Z_s, Z_t	Impedances connected to the unused ports of the whole H1-filer-H2 cascade
Z_{x}	Measured extreme impedance
Γ_1, Γ_2	General input and output reflection coefficients realized by a two-port
$\Gamma_{\mathrm{G}}, \Gamma_{\mathrm{L}}$	Reflection coefficients corresponding to Z_{G} and Z_{L}
$\Gamma_{\mathrm{Gw}}, \Gamma_{\mathrm{Lw}}$	Worst-case reflection coefficients
$\Gamma_{\mathrm{P1}}, \Gamma_{\mathrm{P2}}, \Gamma_{\mathrm{P3}}, \Gamma_{\mathrm{P4}}$	Reflection coefficients realized by ports connected to the filter
Γ_{ref}	Reflection coefficient corresponding to Z_{ref}
Γ_s, Γ_t	Reflection coefficients corresponding to impedances Z_s and Z_t of unused ports of the whole H1-filer-H2 cascade
Γ_{x}	Measured reflection coefficient
Δ	Subtractive signal given by interference of any interfering signal S_{ref} and the signal corresponding to measured Γ_{x}
ΔT_{21}	Measurement error at the plane of the VNA
$\Delta\Gamma_{\mathrm{x}}$	Resulting measurement error of measured reflection coefficient Γ_{x}
$\mu\left(Y\right)$	Mean vector of complex quantity Y
φ	Phase shift corresponding to the Γ_{x} path inside the **IB** structure

1 Introduction

The doctoral thesis is primarily focused on microwave measurements, based on common Scattering parameters (S-parameters) measurements using Vector Network Analyzers (VNAs), either utilizing or suffering from the phenomenon of an interference of electromagnetic waves. The interference of coherent signals is a common part of all microwave circuits and a typical example can be a standing wave on a transmission line caused by multiple reflections in the circuit. Further, all circuits enabling superposition of two correlated signals – e.g., power dividers, hybrids or couplers – create an interference that can be in limit cases either constructive or destructive. There are many cases where the interference affects functionality of microwave circuits – e.g., crosstalks inside microwave passive circuits, parasitic coupling between two transmission lines close to each other, standing wave creating an undesirable filter on a transmission line between two not properly matched circuits and so on. On the other hand, multiple reflections or mutual superposition of two electromagnetic waves, when treated properly, can bring an added value – e.g., filter design, circuits with positive or negative feedback (amplifiers, oscillators), matching circuits, balanced amplifiers and so on.

First, the problems connected to the characterization of electromagnetic interference (EMI) or radio-frequency interference (RFI) filters in their stop band at high megahertz or gigahertz frequencies are studied since the recommended measurement methods stated in standards [1–4] fail in determining the lowest possible insertion loss at these frequencies. It will be shown that interferences of modes, propagating inside the structure of a RFI/EMI filter, have negative effect on the filter performance and, therefore, must be taken into an account when evaluating the interference filters. EMI/RFI filters are amongst the most frequently used electronic components. Their primary task is to pass DC, or 50/60 Hz electric power (sometimes in the order of kilowatts), from a power-line into the required power load, and suppress all higher interfering frequencies (from kilohertz to hundreds of megahertz or even units of gigahertz) which may be coupled to the power-line from the outside environment, or arising in the power load. Simple filter versions are part of all mains-powered devices (PCs, TV sets, etc.). More robust and complex versions are, for example, installed at input ports of screened chambers, where extremely high suppression of high frequency signals radiating from or into the chamber is required to ensure information security for classified data.

Second, precise microwave interferometric measurements of extreme impedances, based on two-port VNA measurement, are analyzed by means of law of uncertainty propagation and Monte Carlo simulations (MCS). The Interferometric measurements utilize the interference of coherent signals to achieve better measurement sensitivity and thus better measurement accuracy with commonly available VNAs. This part of the thesis follows in a doctoral thesis [5], dealing with a development of a method suitable for the measurement of extreme impedances, and moves the knowledge in this field one step further. The term extreme impedances generally relates to structures/materials and passive or active microwave components whose impedance corresponds to reflection coefficient close to the unity. Such impedances/reflection coefficients cannot be accurately measured by common one-port reflection coefficient measurements mainly due to the insufficient measurement stability caused by the VNA noise.

1.1 Main Objectives

- First objective of the doctoral thesis is to examine current measurement methods for EMI/RFI filters and, subsequently, provide a unifying theory for determining the worst-case behavior (minimum insertion loss) of EMI/RFI filters in their stop band under arbitrary input and output impedances.

- Second objective is to extend already published theory, related to interferometric measurement methods, that were neither quantitatively verified nor sufficiently analyzed. The aim is to quantitatively analyze this type of measurement in terms of fundamental limits influencing both the achievable DUT measurement accuracy and precision.

2 Current Situation of Studied Problem

This chapter briefly describes currently used measurement methods, recommended by standards, for characterizing RFI/EMI filters. Further, a brief overview of used interferometric measurement approaches for extreme impedances characterization is presented and a special attention is dedicated to the most promising Nearly Balanced Bridge measurement method developed in [6]. The goal of this chapter is to present the state-of-the-art measurement methods and their limits and drawbacks in order to show possible directions for subsequent scientific research and to support objectives of the thesis stated in previous chapter.

2.1 EMI/RFI filters characterization

Commonly, the EMI/RFI filters are characterized and measured up to 30 MHz, where maxima of interferences are expected. Some (more or less problematic) measurement recommendations can be found also for frequencies up to 1 GHz. But problems connected with electromagnetic interferences get gradually onto even higher frequencies, nowadays commonly into the GHz frequency band. The main reason for that is raising number of electronic devices especially those equipped with digital circuits and radio modems, which are significant sources of interferences. Moreover, operating and clock frequencies of modern electronic devices get also constantly higher and higher. That is why demands to measure EMI/RFI filters in the microwave frequency band also become urgent.

Block diagram of EMI/RFI filter connected between a power-line and the electronic device or screened chamber can be seen in Figure 2.1. The figure does not include power sources or loads and it shows only one source of interfering signal with inner impedance Z_{G} and one interfering signal load with impedance Z_{L}. *IL* stands for operational insertion loss of the filter. With respect to the given application, the worst-case minimum value of the insertion loss IL_{min} at all concerned frequencies in the stop-band is the most important parameter. In all practical states the operational *IL* will be higher than IL_{min}. The main problem of *IL* definition and measurement is the fact that it is a strong function of Z_{G} and Z_{L}, and these values are unknown in practice.

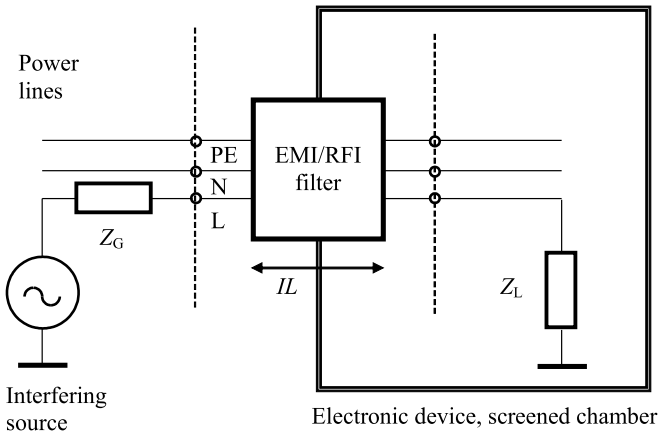

Figure 2.1: Block diagram of EMI/RFI filter connected between power-line and the electronic device or screened chamber.

Basic measurement methods for evaluating electromagnetic and radio frequency suppression capability of power-line filters are defined in the IEEE standard [2]. Two quality assurance methods, which are also described in MIL-STD.220B [3], are based on matched-impedance tests ($Z_{\mathrm{G}} = Z_{\mathrm{L}} = 50\ \Omega$) and serve particularly as a tool for qualitative evaluation of filters. The first, no-load test method ($I_{AC} = I_{DC} = 0$) is used for determination of component malfunctions or assembly errors in the frequency range from 10 kHz to 1 GHz. The second test is intended for measurement of filters under load ($I_{AC} > 0, I_{DC} > 0$) in the frequency range from 10 kHz to 20 MHz. Another no-load test method called mismatched-impedance test is used for measurement of filter *IL* under specified conditions in order to predict the filter performance in a frequency band up to 30 MHz. Wideband transformers converting 50 Ω to 0.1 Ω or 100 Ω impedances connected to the input and the output of the filter are used for these concerned measurements.

Furthermore, two current injection methods are intended for *IL* of filter under load measurements under non-50-Ω impedance conditions up to 30 MHz. The line-impedance stabilization network is employed for the filter measurements above 100 kHz and up to 30 MHz in order to precisely define the source impedance. Reference [2] also describes an aperture leak test, a completely different method, which tests the box of the filter and quality of its mounting on the wall of the shielded chamber up to 10 GHz, while offering little information about the *IL* of the filter itself. Both test methods have their origins (basics) in MIL-STD-461E [4].

Innovated European standard [1] recommends to measure power-line filters in system impedances 0.1 Ω/100 Ω in the frequency range up to 300 kHz. An extension of the mismatched-impedance method applicable up to about 1 GHz was suggested in [7] and [8]. Authors developed resistive coaxial adapters realizing 50 Ω/1 Ω and 50 Ω/100 Ω impedance transformers compatible with microwave measurement instruments. Another measurement method partially reducing measurement errors due to unmatched generator is described in [9]. In reference [10], scattering parameters (S-parameters) measured by a vector network analyzer (VNA) are used for filter characterization in a frequency band up to 30 MHz. Techniques depicted in [11] and [12] are based on voltage/current cascade parameters which are practically measurable only at relatively low frequencies.

There are several significant problems which should be mentioned with respect to the above described methods. First, most of them are focused on measurements at low frequencies below 30 MHz, with some exceptions going up to 1 GHz. However, as has been already mentioned, the need to measure filters at substantial higher frequencies (i.e., up to 10 GHz as mentioned in [2]) is growing and urgently required.

Second, with increasing measurement frequency impedances Z_{L} and Z_{G} become more arbitrary resulting in less reliable estimation of the filter *IL*. Despite the fact that [2] and [1] mention possibility of S-parameter measurements at frequencies above 30 MHz, they give no practical instructions how to determine properties of the filter for unknown terminating impedances.

Therefore, the goal will be to develop a new method able to determine the worst-case behavior (minimum insertion loss) of a EMI/RFI filter under arbitrary impedances Z_{G}, Z_{L} and at any frequency where S-parameters can be measured.

2.2 Extreme impedances - interferometric approaches

Nowadays, there are several measurement techniques employed currently in the microwave and millimeter-wave measurements of extreme impedances and all are based on commonly available VNAs [13–17]. Moreover, a need for fast measurement is growing in the area called Near-Field Scanning Microwave Microscopy (NSMM) because of the number of measurements that are required for high space resolution.

Probably the most effective methods are interferometric approaches where two electromagnetic waves mutually interfere, see [6, 18–21]. In the microwave or millimeter-wave applications special components for dividing power as power dividers, hybrids or couplers must be used. Most approaches utilize common VNAs and transform the reflected signal into an impedance area (around 50 Ω), where the VNA measurements are most sensitive, applying mutually interference of two signals (waves). One is reflected from DUT and second from reference impedance with similar reflection coefficient to DUT.

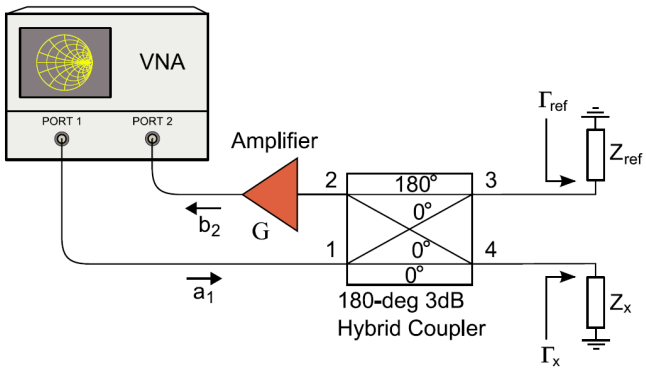

Figure 2.2: Nearly Balanced Bridge measurement method [6].

Into the group of interferometric methods belongs the pioneering Nearly Balanced Bridge measurement method which was developed in [6], see Figure 2.2.

This method is based on the transmission coefficient T_{21} measurement using commonly available VNAs and it substantially increases the precision of a high reflection DUT measurement. To achieve better measurement precision a small subtractive signal, created by the destructive interference of two similar waves inside the 180° hybrid, is amplified by factor G and, subsequently, measured. The first wave is reflected from measured impedance Z_{x} and the second one from reference impedance Z_{ref}, see the equation for T_{21}:

$$T_{21} = \frac{b_2}{a_1} = \frac{G}{2}\left(\Gamma_{\mathrm{x}} - \Gamma_{\mathrm{ref}}\right) \tag{2.2.1}$$

Subsequently, Γ_{x} is expressed from T_{21} measurements, (2.2.1), to see the resulting uncertainty of measured impedance Z_{x}. In contrast to the modern measurement evaluation approach based on uncertainty computation, the authors in [6] evaluated measurement error and derived an equation showing the resulting measurement error $\Delta\Gamma_{\mathrm{x}}$ suppression for an ideal amplifier and 180° hybrid:

$$\Delta\Gamma_{\mathrm{x}} = \frac{2\Delta T_{21}}{G}. \tag{2.2.2}$$

It can be clearly seen that the resulting $\Delta\Gamma_x$ is $G/2$ times smaller than measurement error ΔT_{21} at the plane of the VNA. Moreover, the derived measurement precision improvement given by $G/2$ depends only on the hardware used – 180° 3dB hybrid and amplifier, see explanation in [6]. Nevertheless, neither the limitation and validity of (2.2.2) nor the general meaning of parameter G were specified by the authors. It is problematic that equation (2.2.2) can lead to wrong conclusions since the resulting error $\Delta\Gamma_x \to 0$ for $G \to \infty$ and, therefore, it might seem that $\Delta\Gamma_x$ has no lower limit which is not correct. The authors experimentally verified the measurement precision improvement, however, without any relation to (2.2.2). Real T_{21} measurements are more complicated since some of the uncertainty/error sources, e.g., the phase noise and the noise floor, present in the VNA test channel, are influenced by the hardware used, especially by the amplifier. Since ΔT_{21} also depends on the 180° hybrid and amplifier used, the equation (2.2.2) is confusing and does not "say" what the real measurement precision improvement is.

Further, authors also derived error model describing the T_{21} measurement:

$$T_{21} = \frac{b_2}{a_1} = \frac{C_1 + C_2\Gamma_x}{1 - C_3\Gamma_x}. \tag{2.2.3}$$

The error model depends on three calibration/error constants C_1, C_2, and C_3, therefore, it is necessary to use three fully-known calibration standards to calibrate a real measurement setup. Since high precision does not imply high measurement accuracy, the first measurements of real DUTs [22] showed basic problems connected to the calibration process in terms of poorly characterized calibration standards properties and their limited connection repeatability. Further, they concluded that the proposed method could not be fully utilized with commonly available calibration standards (i.e., *Short*, *Match* and *Open*) and that there is a need for well-characterized calibration standards situated in the area of extreme impedances with a similar reflection coefficient to the reference impedance and DUT. They also mentioned problems/limitations connected to real hardware (amplifier and 180° Hybrid) but none of these limitations were really studied and quantified with respect to the resulting measurement accuracy of the DUT measurement.

Therefore, the goal will be to quantitatively analyze the microwave measurement of extreme impedances based on interferometric approaches in terms of fundamental limits influencing both the achievable DUT measurement accuracy and precision. Phenomena as mounting repeatability of a standard or a DUT, calibration standards characterization or selection, phase noise, noise floor, and real hardware influence will be studied in detail by means of two independent methods, Monte Carlo simulations (MCS) and the law of uncertainty propagation (LUP).

3 Theory

This chapter brings a theoretical background, developed by the author, for both studied topics – EMI/RFI filters characterization and extreme impedances measurement. A new approach for EMI/RFI filters characterization based on measured S-parameters evaluation is developed and published in [23,24]. Further, a theory needed for clarification of extreme impedances measurement in terms of fundamental limits and achievable measurement precision and accuracy is developed.

3.1 EMI/RFI filters - worst-case scenario analysis

Owing to the fact that the EMI/RFI filters are intended to be measured in the GHz frequency region, it is logical and effective to use a common microwave measurement and analytical methods, i.e., an S-parameter measurement by a standard VNA and to use microwave analytical tools based on S-parameters and reflection coefficients.

3.1.1 Γ_{opt} method

Figure 3.1 depicts the connection of a two-port characterized by S-parameters with general input and output impedances Z_{G} and Z_{L}, respectively.

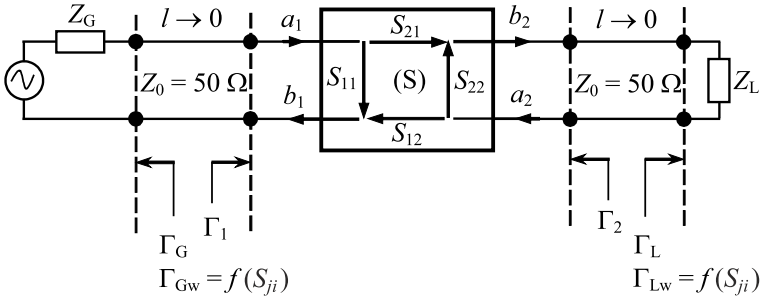

Figure 3.1: Connection of a two-port characterized by S-parameters with general input and output impedances Z_{G} and Z_{L}.

The schematic also contains two sections of zero-length transmission lines, with $Z_0 = 50\ \Omega$, to define the reflection coefficients $\Gamma_{\mathrm{G}}, \Gamma_1, \Gamma_2$, and Γ_{L}. Relations between impedances Z_{G}, Z_{L} and reflection coefficients $\Gamma_{\mathrm{G}}, \Gamma_{\mathrm{L}}$, respectively, are given by well-known formulas (3.1.1) and (3.1.2).

$$\Gamma_{\mathrm{G}} = \frac{Z_{\mathrm{G}} - Z_0}{Z_{\mathrm{G}} + Z_0} \tag{3.1.1}$$

$$\Gamma_{\mathrm{L}} = \frac{Z_{\mathrm{L}} - Z_0}{Z_{\mathrm{L}} + Z_0} \tag{3.1.2}$$

It should be emphasized that the S-parameters of the evaluated EMI/RFI filters are also referenced to $Z_0 = 50\ \Omega$ transmission lines connected to both ports.

There are two reasons for insertion loss in a filter stop-band. A significant portion of the energy from an incident electromagnetic wave is reflected, and the rest is transformed into heat inside the filter structure. In the worst case scenario, Γ_{G} and Γ_{L} correspond to

complex conjugate Γ_1 and Γ_2 values, respectively, and a simultaneous impedance matching state occurs. These Γ_{Gw} and Γ_{Lw} worst-case reflection coefficients can be calculated from equations (3.1.3) and (3.1.4):

$$\Gamma_{\mathrm{Gw}}{}^{*} = \Gamma_1 = S_{11}{}' = S_{11} + \frac{S_{12}S_{21}\Gamma_{\mathrm{Lw}}}{1 - S_{22}\Gamma_{\mathrm{Lw}}} \tag{3.1.3}$$

$$\Gamma_{\mathrm{Lw}}{}^{*} = \Gamma_2 = S_{22}{}' = S_{22} + \frac{S_{12}S_{21}\Gamma_{\mathrm{Gw}}}{1 - S_{11}\Gamma_{\mathrm{Gw}}} \tag{3.1.4}$$

This matching technique is frequently used in the design of microwave amplifiers to achieve the maximum available gain, [25]. The solution of equations (3.1.3) and (3.1.4) is commonly presented in the following form:

$$\Gamma_{\mathrm{Gw}} = F_1^{*}\left[E_1 \pm \left(E_1^2 - 4\left|F_1\right|^2\right)^{\frac{1}{2}}\right]\frac{1}{2\left|F_1\right|^2} \tag{3.1.5}$$

$$\Gamma_{\mathrm{Lw}} = F_2^{*}\left[E_2 \pm \left(E_2^2 - 4\left|F_2\right|^2\right)^{\frac{1}{2}}\right]\frac{1}{2\left|F_2\right|^2} \tag{3.1.6}$$

The complex constants E_q, $F_q (q = 1, 2)$ and D are only functions of S-parameters and can be calculated according to formulas (3.1.7)-(3.1.11):

$$E_1 = 1 + \left|S_{11}\right|^2 - \left|S_{22}\right|^2 - \left|D\right|^2 \tag{3.1.7}$$

$$E_2 = 1 - \left|S_{11}\right|^2 + \left|S_{22}\right|^2 - \left|D\right|^2 \tag{3.1.8}$$

$$F_1 = S_{11} - DS_{22}^{*} \tag{3.1.9}$$

$$F_2 = S_{22} - DS_{11}^{*} \tag{3.1.10}$$

$$D = S_{11}S_{22} - S_{12}S_{21} \tag{3.1.11}$$

The minus sign is used in (3.1.5) and (3.1.6) when $E_q > 0$ and the plus sign when $E_q < 0$, see [26]. The gain of the microwave two-port, operated into general Γ_{G} and Γ_{L} port reflection coefficients, is generally described by the transducer gain:

$$G_{\mathrm{t}} = f\left(S_{ji}, \Gamma_{\mathrm{G}}, \Gamma_{\mathrm{L}}\right) = \frac{P_{\mathrm{L}}}{P_{\mathrm{AG}}} = \frac{\left(1 - \left|\Gamma_{\mathrm{L}}\right|^2\right)\left|S_{21}\right|^2\left(1 - \left|\Gamma_{\mathrm{G}}\right|^2\right)}{\left|\left(1 - S_{11}\Gamma_{\mathrm{G}}\right)\left(1 - S_{22}\Gamma_{\mathrm{L}}\right) - S_{12}S_{21}\Gamma_{\mathrm{G}}\Gamma_{\mathrm{L}}\right|^2}, \tag{3.1.12}$$

where P_{L} stands for power delivered to the load and P_{AG} represents available power from the source, see [25].

The worst-case minimum insertion loss value IL_{min} is inversely proportional to the maximum available gain G_{tmax} and can be calculated from G_{t} under conditions $\Gamma_{\mathrm{G}} = \Gamma_{\mathrm{Gw}}$ and $\Gamma_{\mathrm{L}} = \Gamma_{\mathrm{Lw}}$. The solution is usually presented in the following form:

$$G_{\mathrm{tmax}} = \frac{1}{IL_{\mathrm{min}}} = \left|\frac{S_{21}}{S_{12}}\right|\left(k - \sqrt{k^2 - 1}\right) \tag{3.1.13}$$

Parameter k, known as the stability factor, can be calculated from S-parameters using

$$k = \frac{1 - |S_{11}|^2 - |S_{22}|^2 + |D|^2}{2\,|S_{12}S_{21}|} \tag{3.1.14}$$

Formulas (3.1.3)–(3.1.14) are well-known in microwave amplifier design techniques. However, applying the formulas to filter analysis is new and makes it possible to determine $IL_{\min}$. Since the concerned filters are reciprocal devices and $S_{12} = S_{21}$, (3.1.13) can be simplified and rewritten into (3.1.15).

$$IL_{\min} = \frac{1}{G_{\mathrm{tmax}}} = \frac{1}{k - \sqrt{k^2 - 1}} \tag{3.1.15}$$

The formulas (3.1.13)–(3.1.15) show that the desired $IL_{\min}$ values can be easily and unambiguously calculated from the S-parameters measured.

However, there is one principal limiting condition. The filters under-test must be linear, which may be slightly problematic in the case of high DC or 50/60 Hz currents with respect to the inner filter coil cores with possible current-dependent permeabilities. In such cases, repeated measurements for different DC or AC currents and the worst-case $IL_{\min}$ evaluation can be recommended.

This method (marked as "Γ_{opt} method" in the following text), [23], reliably and unambiguously determines the worst-case behavior (i.e., minimum insertion loss $IL_{\min}$) of a single-ended filter in the stop-band independent of its termination impedances.

3.1.2 Mixed mode analysis

In addition to a simple single-ended filter, Γ_{opt} method can be applied to the characterization of a professional EMI/RFI filter, see e.g., the simplified stucture of a professional SKY1FL16DMA2 (SKYBERGTECH) single-phase interference filter in Fig 3.2. This EMI/RFI single-phase 3-wire (European standard) filter is designated for the interconnection of power-line cables and power electronic devices (up to 16 A) or screened chambers. The structure of the filter corresponds to common EMI/RFI filters of this type. It has PE (Protective Earth), N (Neutral) and L (Line) terminals at the input and at the output.

As the structure employs three conductor terminals at the input and output, in principle, two modes can propagate through the filter with the common mode (CM) and the differential mode (DM) being widely used forms of these modes. Conversions between these modes can also be taken into account. Another possible representation considers the filter as a metallic box with PE terminals as a common ground, and the N and L terminals at both sides forming a four-port which can be easily measured and its S-parameters, (3.1.16), used for filter characterization.

$$\boldsymbol{S}^{\mathrm{filter}} = \begin{pmatrix} S_{11} & S_{12} & S_{13} & S_{14} \\ S_{21} & S_{22} & S_{23} & S_{24} \\ S_{31} & S_{32} & S_{33} & S_{34} \\ S_{41} & S_{42} & S_{43} & S_{44} \end{pmatrix} \tag{3.1.16}$$

For the analysis of this filter, a prevalent description based on common and differential modes is employed. Being inspired by [27, Figure 2.7], the analysis was performed in the

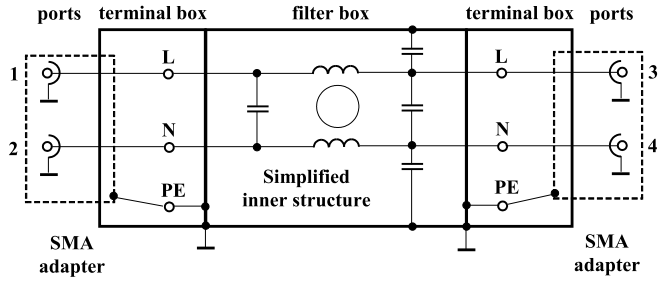

Figure 3.2: Simplified structure of a single-phase EMI/RFI filter with SMA measurement adapters.

AWR Microwave Office (AWR MO) simulator (any standard RF CAD tool can be used) by using one of its common power-divider models and a constant phase-shift model. For the determination of operational insertion loss IL and worst-case minimum insertion loss $IL_{\min}$ of the concerned filter in terms of CM ($IL_{\mathrm{CC}}, IL_{\mathrm{minCC}}$) and DM ($IL_{\mathrm{DD}}, IL_{\mathrm{minDD}}$) and their mutual CM→DM ($IL_{\mathrm{DC}}, IL_{\mathrm{minDC}}$) or DM→CM ($IL_{\mathrm{CD}}, IL_{\mathrm{minCD}}$) conversions, the four-port S-matrix $\boldsymbol{S}^{\mathrm{filter}}$ is connected between two ideal 50-Ω in-phase or out-of-phase power dividers $\mathrm{PD_a}$ and $\mathrm{PD_b}$, as seen in Figure 3.3. The applied procedure can be explained in greater detail as follows.

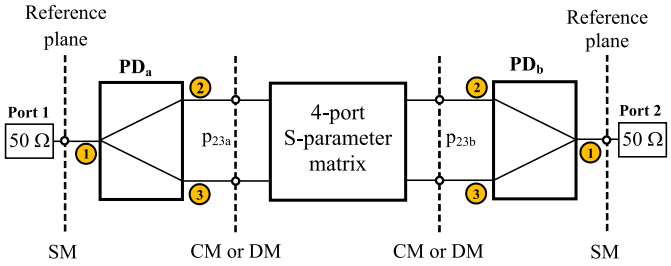

Figure 3.3: Block diagram used for the calculation of CM and DM parameters of a single-phase EMI/RFI filter.

For the CM calculations, an ideal in-phase power divider (the corresponding AWR MO model is called SPLIT2), described by standard S-parameter matrix $\boldsymbol{S}^{\mathrm{IP}}$ (3.1.17), is used. The properties of this power divider can be explained in detail by using ideas presented in [28]. The S-parameter matrix (3.1.17) of this power divider corresponds to a single-ended 3-port with 50-Ω reference impedances at all ports (port numbering corresponds to Figure 3.3).

$$\boldsymbol{S}^{\mathrm{IP}} = \frac{1}{\sqrt{2}} \begin{pmatrix} 0 & 1 & 1 \\ 1 & 0 & 0 \\ 1 & 0 & 0 \end{pmatrix} \tag{3.1.17}$$

$$\boldsymbol{S}^{\mathrm{OP}} = \frac{1}{\sqrt{2}} \begin{pmatrix} 0 & -1 & 1 \\ -1 & 0 & 0 \\ 1 & 0 & 0 \end{pmatrix} \tag{3.1.18}$$

This in-phase power divider converts the single-ended mode (SM) entering the 50-Ω port **1** into two equal in-phase SM signals at ports **2** and **3**. These ports, considered

together, form a mixed-mode port p_{23} for the CM signal. As ports **2** and **3** are connected in parallel (with respect to the CM), the impedance of this mixed-mode CM port p_{23} is 25 Ω, [29, eq. (15)]. The divider is also reciprocal with unity power transmission between SM and CM. For signals from an opposite direction, it serves as an ideal in-phase combiner.

For the DM simulations, an ideal out-of-phase power divider, described by the S-parameter matrix $\boldsymbol{S}^{\mathrm{OP}}$ (3.1.18), is used. In the AWR MO simulator it can be formed by the SPLIT2 power divider together with an ideal phase shifter PHASE2 added to port **2** and set to 180°, see the right side of Figure 3.4. The standard S-parameter matrix (3.1.18) corresponds to a single-ended 3-port with 50-Ω reference impedances at all ports (port numbering corresponds to Figure 3.3). The out-of-phase power divider converts the SM entering the 50-Ω port **1** into two equal out-of-phase SM signals at ports **2** and **3**. These two ports, considered together, form the mixed-mode port p_{23} for the DM signal. As ports **2** and **3** are connected in series (with respect to the DM), the impedance of the mixed-mode port p_{23} is 100 Ω, [29, eq. (14)]. This divider also shows unity power transmission between SM and DM. For signals from an opposite direction, it serves as an ideal out-of-phase combiner.

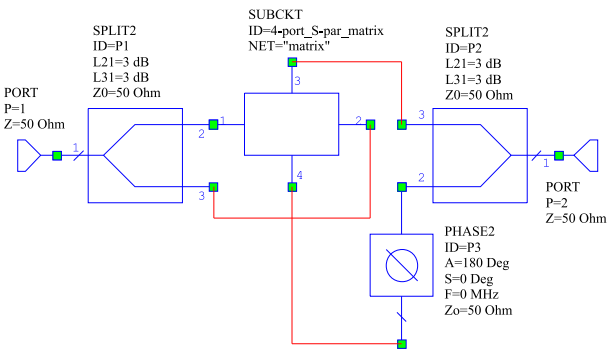

Figure 3.4: AWR MO schematic corresponding to CM→DM calculations.

There is an important question of what will happen when a DM signal enters the mixed-mode p_{23} port of the in-phase power divider/combiner, or, when a CM signal enters the mixed-mode p_{23} port of the out-of-phase power divider/combiner. In both cases, the signals can be decomposed into in-phase or out-of-phase components propagating in the form of SM into the 50-Ω ports. Due to zeroes on the main diagonal in S-matrix (3.1.17) and (3.1.18) these signals are not reflected back. Moreover, due to numbers 1 in (3.1.17) there is zero transmission between DM at the mixed-mode p_{23} and SM at port **1** in the in-phase power divider/combiner. Similarly, due to numbers 1 and -1 in (3.1.18) there is also zero transmission between CM at mixed-mode port p_{23} and SM at port **1** in the out-of-phase power divider/combiner.

Due to these ideal properties of the in-phase and out-of-phase power dividers/combiners all insertion losses of the whole cascade between SM ports Port 1 and Port 2 are equal to insertion losses between mixed-mode ports p_{23a} and p_{23b} of the lone filter, see Figure 3.3. Therefore, insertion losses IL_{CC}, IL_{DD}, IL_{DC} and IL_{CD} of the filter can be simply determined using the corresponding standard two-port S-parameters at Port 1 and Port 2 obtained by simulations in AWR MO. Minimum insertion losses IL_{minCC}, IL_{minDD}, IL_{minDC}

and IL_{minCD} can then be calculated using (3.1.15). This approach based on evaluation of measured filter S-parameters was published in [23].

3.1.3 Mixed mode analysis - advanced method

Quite surprisingly, subsequent detailed research showed that IL_{min} values can be, in some cases, even lower than those calculated according to the mentioned approach in Section 3.1.2. It is caused by the fact that the calculations based on the "Γ_{opt} method" work with impedance termination of the converted modes and do not take into account the possibility of their reflections back into the filter structure. These peculiar properties of the power divider/combiners $\mathrm{PD_a}$ and $\mathrm{PD_b}$, however, do not correspond to general impedance conditions at the filter terminals connected to real power-lines meaning that the arrangement described in Figure 3.3 is not sufficiently general and unable to set arbitrary impedances at the filter ports for any CM or DM.

To overcome the problem, a new circuit arrangement enabling the conversion of the mixed-mode structure to the SM structure was developed, as can be seen in Figure 3.5.

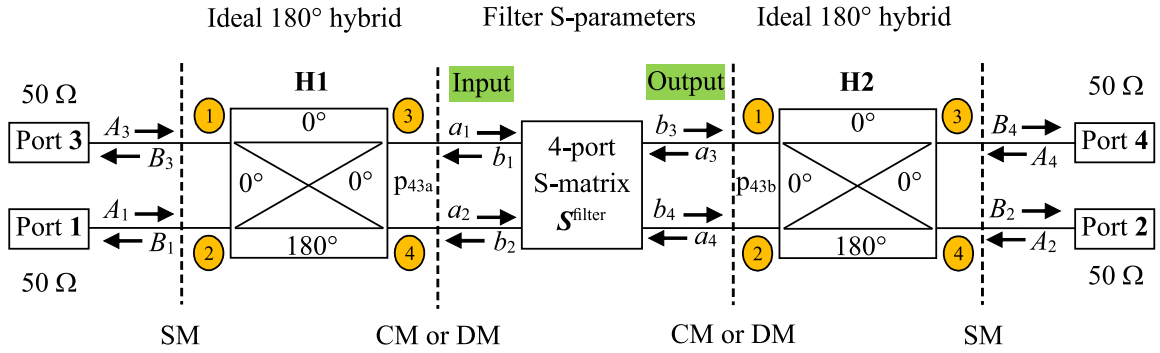

Figure 3.5: Advanced structure enabling the excitation of all CM/DM combinations.

The S-matrix of the filter under test $\boldsymbol{S}^{\mathrm{filter}}$, (3.1.16), was inserted between H1 and H2, two ideal 180° hybrids, described by S-matrix

$$\boldsymbol{S}^{\mathrm{H}} = \frac{1}{\sqrt{2}} \begin{pmatrix} 0 & 0 & 1 & 1 \\ 0 & 0 & 1 & -1 \\ 1 & 1 & 0 & 0 \\ 1 & -1 & 0 & 0 \end{pmatrix}. \tag{3.1.19}$$

Each of the 180° hybrids fully replaces the behavior of both in-phase and out-of-phase power dividers/combiners shown in Figure 3.3. Both H1 and H2 hybrids convert the SM signal entering their respective ports ② into two out-of-phase signals at ports ③ and ④ thereby behaving as ideal out-of-phase power dividers. They also convert the SM signal entering their respective ports ① into two in-phase signals at ports ③ and ④ thereby behaving as ideal in-phase power dividers. Ports ③ and ④ form mixed-mode ports $\mathrm{p_{43a}}$ and $\mathrm{p_{43b}}$, much like $\mathrm{PD_a}$ and $\mathrm{PD_b}$. Depending on which port is used for the excitation of each hybrid, mixed-mode port $\mathrm{p_{43}}$ thus forms either the CM port with impedance 25 Ω, or, the DM port with impedance 100 Ω. For signals from the opposite direction, they serve as ideal out-of-phase combiners. The hybrids are reciprocal with unity power transformation between SM and CM or DM. Moreover, due to their ideal properties, all insertion losses

of the whole H1-filter-H2 cascade between the SM ports at the input and output are equal to insertion losses between mixed-mode ports p_{43a} and p_{43b}.

Single-ended Port **1** of the entire H1-filter-H2 cascade excites the DM, and single-ended Port **3** excites the CM at input port p_{43a} of the filter under test. At the output side of the filter, single-ended Port **2** receives the DM, and single-ended Port **4** receives the CM emerging from port p_{43b}.

Table 3.1: Applied matrices – port and index relations

Transmission between ports	Measurement type	IL^{ji} to be calculated	Influenced by (unused ports)	Degenerated S-matrix $\boldsymbol{S}^{\mathrm{D}ji}$	S-matrix $\boldsymbol{S}^{ji}$ with reduced indices
Port **1** – Port **2** $i=1, j=2$	DM→DM	$IL^{21}_{\mathrm{min}}, IL^{21}_{\mathrm{minW}}$	$\Gamma_{\mathrm{P3}}, \Gamma_{\mathrm{P4}}$ $s=3, t=4$	$\boldsymbol{S}^{\mathrm{D21}}$	$\boldsymbol{S}^{21}$
Port **1** – Port **4** $i=1, j=4$	DM→CM	$IL^{41}_{\mathrm{min}}, IL^{41}_{\mathrm{minW}}$	$\Gamma_{\mathrm{P2}}, \Gamma_{\mathrm{P3}}$ $s=2, t=3$	$\boldsymbol{S}^{\mathrm{D41}}$	$\boldsymbol{S}^{41}$
Port **3** – Port **2** $i=3, j=2$	CM→DM	$IL^{23}_{\mathrm{min}}, IL^{23}_{\mathrm{minW}}$	$\Gamma_{\mathrm{P1}}, \Gamma_{\mathrm{P4}}$ $s=1, t=4$	$\boldsymbol{S}^{\mathrm{D23}}$	$\boldsymbol{S}^{23}$
Port **3** – Port **4** $i=3, j=4$	CM→CM	$IL^{43}_{\mathrm{min}}, IL^{43}_{\mathrm{minW}}$	$\Gamma_{\mathrm{P1}}, \Gamma_{\mathrm{P2}}$ $s=1, t=2$	$\boldsymbol{S}^{\mathrm{D43}}$	$\boldsymbol{S}^{43}$

In comparison with the structure illustrated in Figure 3.3, the main advantage of the new arrangement, shown in Figure 3.5, lies in the possibility of determining a transmission between any of the input ports (Port **1** or Port **3**), and any of the output ports (Port **2** or Port **4**) of the whole H1-filter-H2 cascade while leaving the unused ports to be connected to general impedances with corresponding reflection coefficients. For example, let us consider the transmission between SM Port **1** and SM Port **4** that enables the calculation of the IL^{41} DM→CM insertion loss values. The filter itself can reflect part of the input signal, in the form of a converted CM signal, at port p_{43a}. For the arrangement shown in Figure 3.3, the converted and reflected signal was absorbed in the PD_a power divider. In the new arrangement, according to Figure 3.5, this signal exits at Port **3** where, in general, any impedance can be connected. The signal can, therefore, be partially or totally reflected back towards the filter input where it can again be converted into a DM signal. A similar situation can also be considered at the output of the filter. The DM signal at the Port **2** can be partially or totally reflected back towards the filter output where it can be converted into a CM signal. Consequently, these parts of the signals reflected back to the filter terminals can significantly influence the resulting insertion loss IL^{41} whose values are dependent on reflection coefficients Γ_s and Γ_t (i.e., terminating impedances Z_s and Z_t) at Port **2** and Port **3**, as can be seen in Figure 3.6(c). Relations between reflection coefficients Γ_s and Γ_t and terminating impedances Z_s and Z_t are given by well-known formulas (3.1.20) and (3.1.21). In these formulas Z_0 stands for characteristic impedance, a standard value attains $Z_0 = 50\ \Omega$. Relations among measurement ports and measurements of individual mode transmissions are summarized in Table 3.1.

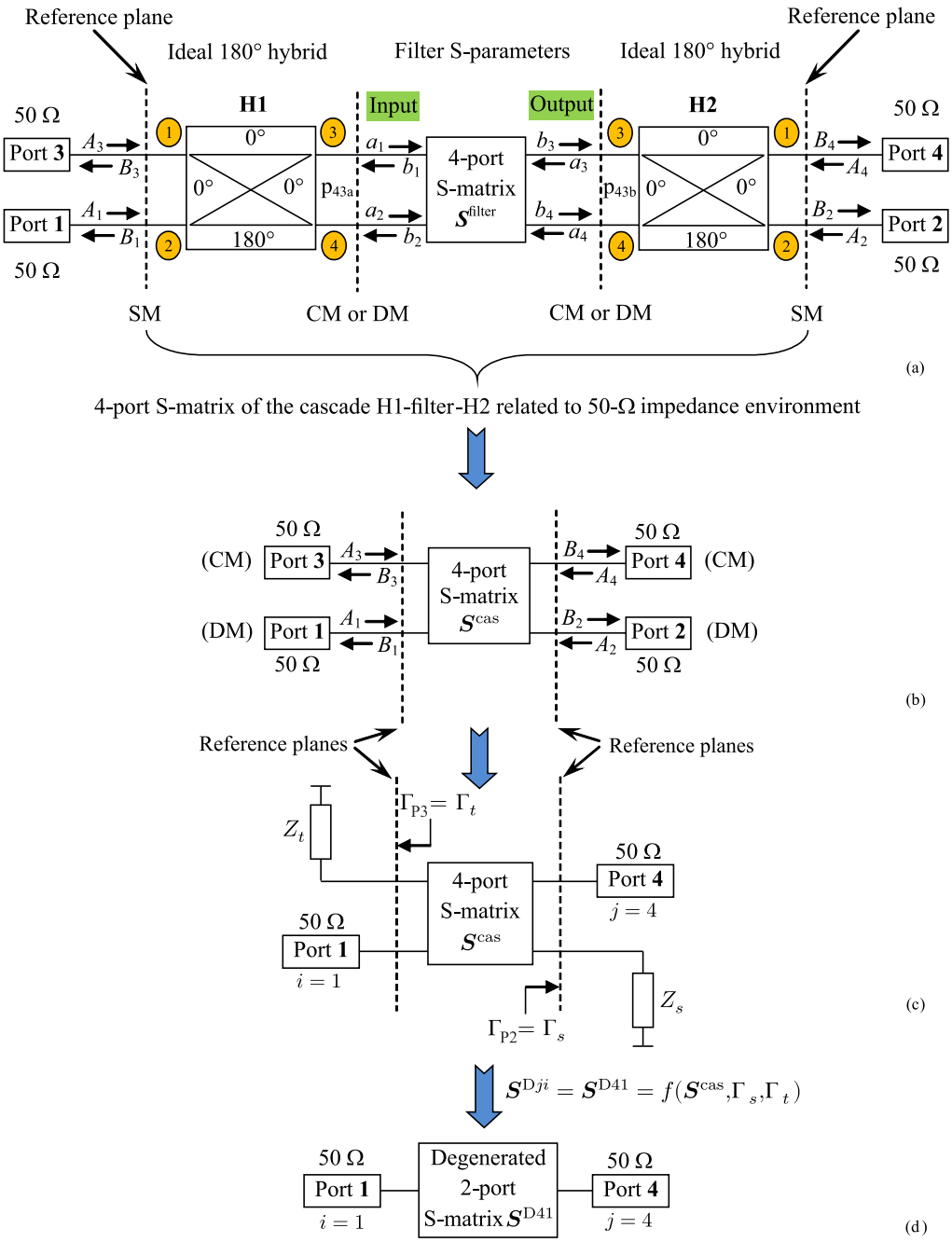

*Figure 3.6: Flow chart showing the derivation procedure of the degenerated two-port S-matrix $\boldsymbol{S}^{D41}$: a) Structure enabling the excitation of all CM/DM combinations; b) Four-port S-matrix $\boldsymbol{S}^{cas}$ of the H1-filter-H2 cascade related to a 50-Ω impedance environment; c) Four-port, described by $\boldsymbol{S}^{cas}$, terminated with general impedances/reflection coefficients at unused Ports **2** and **3**; d) Degenerated two-port, described by S-matrix $\boldsymbol{S}^{D41}$, with the Port **1** input and Port **4** output.*

$$\Gamma_s = \frac{Z_s - Z_0}{Z_s + Z_0} \tag{3.1.20}$$

$$\Gamma_t = \frac{Z_t - Z_0}{Z_t + Z_0} \tag{3.1.21}$$

For each required mode transmission, proper measurement ports corresponding to Figure 3.5 can be assigned, while the measurement is influenced by reflection coefficients at the unused ports. It can be concluded that the circuit arrangement described in Figure 3.5 enables the insertion losses of the filter under test to be analyzed under general impedance conditions with arbitrary impedances/reflection coefficients connected to its ports for all CM/DM combinations.

For further analysis, it is necessary to determine the SM S-matrix $\boldsymbol{S}^{\mathrm{cas}}$ of the whole H1-filter-H2 cascade with the four SM ports (Ports **1**, **2**, **3**, and **4**) defined according to Figure 3.5. According to [30], this matrix can be derived using transfer scattering or T-parameters, but a simpler way can also be found. In the following text it will be shown that matrix $\boldsymbol{S}^{\mathrm{cas}}$ is equal to mixed mode S-matrix $\boldsymbol{S}^{\mathrm{mix}}$, as defined in accordance with the transformation between the measured four-port single-ended S-parameters and the mixed-mode S-parameters. According to [29], the $\boldsymbol{S}^{\mathrm{mix}}$ matrix can be expressed as:

$$\boldsymbol{S}^{\mathrm{mix}} = \boldsymbol{M}\,\boldsymbol{S}^{\mathrm{filter}}\,\boldsymbol{M}^{-1} = \begin{pmatrix} S_{11\mathrm{DD}} & S_{12\mathrm{DD}} & S_{11\mathrm{DC}} & S_{12\mathrm{DC}} \\ S_{21\mathrm{DD}} & S_{22\mathrm{DD}} & S_{21\mathrm{DC}} & S_{22\mathrm{DC}} \\ S_{11\mathrm{CD}} & S_{12\mathrm{CD}} & S_{11\mathrm{CC}} & S_{12\mathrm{CC}} \\ S_{21\mathrm{CD}} & S_{22\mathrm{CD}} & S_{21\mathrm{CC}} & S_{22\mathrm{CC}} \end{pmatrix}, \tag{3.1.22}$$

where $\boldsymbol{M}$ stands for the transformation matrix given by (3.1.23).

$$\boldsymbol{M} = \frac{1}{\sqrt{2}} \begin{pmatrix} 1 & -1 & 0 & 0 \\ 0 & 0 & 1 & -1 \\ 1 & 1 & 0 & 0 \\ 0 & 0 & 1 & 1 \end{pmatrix} \tag{3.1.23}$$

In accordance with [29] and (3.1.19), mixed-mode normalized waves at mixed-mode ports $\mathrm{p_{43a}}$ and $\mathrm{p_{43b}}$ of the filter can be expressed in terms of SM standard normalized waves A_i and B_i at ports of the entire H1-filter-H2 cascade, as shown in Figure 3.5:

$$\begin{aligned}
a_{d1} &= \frac{1}{\sqrt{2}}(a_1 - a_2) = \frac{1}{\sqrt{2}}\left(\frac{1}{\sqrt{2}}A_1 + \frac{1}{\sqrt{2}}A_1\right) = A_1 \\
a_{c1} &= \frac{1}{\sqrt{2}}(a_1 + a_2) = \frac{1}{\sqrt{2}}\left(\frac{1}{\sqrt{2}}A_3 + \frac{1}{\sqrt{2}}A_3\right) = A_3 \\
b_{d1} &= \frac{1}{\sqrt{2}}(b_1 - b_2) = \frac{1}{\sqrt{2}}\left(\frac{1}{\sqrt{2}}B_1 + \frac{1}{\sqrt{2}}B_1\right) = B_1 \\
b_{c1} &= \frac{1}{\sqrt{2}}(b_1 + b_2) = \frac{1}{\sqrt{2}}\left(\frac{1}{\sqrt{2}}B_3 + \frac{1}{\sqrt{2}}B_3\right) = B_3 \\
a_{d2} &= \frac{1}{\sqrt{2}}(a_3 - a_4) = \frac{1}{\sqrt{2}}\left(\frac{1}{\sqrt{2}}A_2 + \frac{1}{\sqrt{2}}A_2\right) = A_2
\end{aligned}$$

$$a_{c2} = \frac{1}{\sqrt{2}}(a_3 + a_4) = \frac{1}{\sqrt{2}}\left(\frac{1}{\sqrt{2}}A_4 + \frac{1}{\sqrt{2}}A_4\right) = A_4$$
$$b_{d2} = \frac{1}{\sqrt{2}}(b_3 - b_4) = \frac{1}{\sqrt{2}}\left(\frac{1}{\sqrt{2}}B_2 + \frac{1}{\sqrt{2}}B_2\right) = B_2$$
$$b_{c2} = \frac{1}{\sqrt{2}}(b_3 + b_4) = \frac{1}{\sqrt{2}}\left(\frac{1}{\sqrt{2}}B_4 + \frac{1}{\sqrt{2}}B_4\right) = B_4. \tag{3.1.24}$$

This means that the mixed-mode a-waves at ports $\mathrm{p_{43a}}$ and $\mathrm{p_{43b}}$ of the filter are equal to standard SM A-waves at Ports **1**, **2**, **3**, and **4** of the whole H1-filter-H2 cascade. The same is also true for the mixed mode b-waves and standard SM B-waves. However, it also means that individual elements of matrices $\boldsymbol{S}^{\mathrm{mix}}$ and $\boldsymbol{S}^{\mathrm{cas}}$ are equivalent. Therefore, SM matrix $\boldsymbol{S}^{\mathrm{cas}}$ can be determined by the simple matrix equation:

$$\boldsymbol{S}^{\mathrm{cas}} = \boldsymbol{S}^{\mathrm{mix}} = \boldsymbol{M}\,\boldsymbol{S}^{\mathrm{filter}}\boldsymbol{M}^{-1}. \tag{3.1.25}$$

It should be emphasized that individual elements of matrices $\boldsymbol{S}^{\mathrm{mix}}$ and $\boldsymbol{S}^{\mathrm{cas}}$ are related to different characteristic impedances. The common mode elements of the $\boldsymbol{S}^{\mathrm{mix}}$ matrix are related to CM impedance of 25 Ω and the differential mode elements to DM impedance of 100 Ω. On the other hand, all elements of the S-matrix $\boldsymbol{S}^{\mathrm{cas}}$ are related to SM transmission lines with standard characteristic impedances 50 Ω. This property of the $\boldsymbol{S}^{\mathrm{cas}}$ matrix constitutes a significant advantage and enables us to apply common microwave formulas developed for the analysis of two-ports characterized by standard S-parameters, as presented, e.g., in [25] or [26], for subsequent IL_{min} calculations.

To analyze minimum insertion losses IL^{43}_{min} for CM→CM, IL^{21}_{min} for DM→DM, IL^{23}_{min} for CM→DM, and IL^{41}_{min} for DM→CM of the EMI/RFI filters in question, it is necessary to derive degenerated two-port S-matrices $\boldsymbol{S}^{\mathrm{D43}}$ for CM→CM, $\boldsymbol{S}^{\mathrm{D21}}$ for DM→DM, $\boldsymbol{S}^{\mathrm{D41}}$ for DM→CM, and $\boldsymbol{S}^{\mathrm{D23}}$ for CM→DM. All these two-port matrices can be derived from the four-port S-matrix $\boldsymbol{S}^{\mathrm{cas}}$ by reducing ports loaded by reflection coefficients Γ_s and Γ_t. When searching for the worst-case insertion losses IL^{ji}_{minW}, these terminating reflection coefficients should show unity amplitudes that lead to 100 % reflection of the converted modes back into the filter structure. Subsequently, the formula (3.1.15) to compute IL^{ji}_{min} values can be employed to analyze all individual cases. The desired worst-case IL^{ji}_{minW} values are then the object of an optimization process using phases of the concerned reflection coefficients at each frequency point.

Using only ports i and j of the H1-filter-H2 cascade, while the other two ports s and t are terminated with general impedances, reduces the four-port S-matrix $\boldsymbol{S}^{\mathrm{cas}}$ to a degenerated two-port S-matrix $\boldsymbol{S}^{\mathrm{D}ji}$, see Figure 3.6(c). Values of indices i and j correspond to values of the chosen input and output ports of the H1-filter-H2 cascade, respectively. Table 3.1 shows all practically important combinations of ports i and j corresponding to the degenerated two-port S-matrices $\boldsymbol{S}^{\mathrm{D43}}$, $\boldsymbol{S}^{\mathrm{D21}}$, $\boldsymbol{S}^{\mathrm{D41}}$, $\boldsymbol{S}^{\mathrm{D23}}$.

The derivation of the corresponding formulas are shown for the degenerated two-port, described by S-matrix $\boldsymbol{S}^{\mathrm{D41}}$, with the Port **1** input and Port **4** output, see Figure 3.6.

Standard four-port S-parameters of the H1-filter-H2 cascade are defined at reference planes according to Figure 3.6(b), and can be expressed using (3.1.26)–(3.1.29).

$$B_1 = S^{\mathrm{cas}}_{11}A_1 + S^{\mathrm{cas}}_{12}A_2 + S^{\mathrm{cas}}_{13}A_3 + S^{\mathrm{cas}}_{14}A_4 \tag{3.1.26}$$
$$B_2 = S^{\mathrm{cas}}_{21}A_1 + S^{\mathrm{cas}}_{22}A_2 + S^{\mathrm{cas}}_{23}A_3 + S^{\mathrm{cas}}_{24}A_4 \tag{3.1.27}$$

$$B_3 = S_{31}^{\text{cas}} A_1 + S_{32}^{\text{cas}} A_2 + S_{33}^{\text{cas}} A_3 + S_{34}^{\text{cas}} A_4 \tag{3.1.28}$$
$$B_4 = S_{41}^{\text{cas}} A_1 + S_{42}^{\text{cas}} A_2 + S_{43}^{\text{cas}} A_3 + S_{44}^{\text{cas}} A_4 \tag{3.1.29}$$

Transmission between Port **1** and Port **4**, corresponding to the DM→CM conversion, is influenced by general reflection coefficients Γ_{P2} and Γ_{P3} terminating at Ports **2** and **3**, see Figure 3.6(c). Both reflection coefficients are defined by (3.1.30) and (3.1.31):

$$\Gamma_{\text{P2}} = A_2/B_2 \Rightarrow A_2 = \Gamma_{\text{P2}} B_2 \tag{3.1.30}$$
$$\Gamma_{\text{P3}} = A_3/B_3 \Rightarrow A_3 = \Gamma_{\text{P3}} B_3. \tag{3.1.31}$$

Subsequently, B_2 and B_3 can be derived from (3.1.27) and (3.1.28) using conditions (3.1.30) and (3.1.31).

$$B_2 = S_{21}^{\text{cas}} A_1 D_3 + S_{24}^{\text{cas}} A_4 D_3 + S_{23}^{\text{cas}} S_{31}^{\text{cas}} A_1 \Gamma_{\text{P3}} D_2 D_3 + S_{23}^{\text{cas}} S_{34}^{\text{cas}} A_4 \Gamma_{\text{P3}} D_2 D_3 \tag{3.1.32}$$
$$B_3 = S_{31}^{\text{cas}} A_1 D_4 + S_{34}^{\text{cas}} A_4 D_4 + S_{32}^{\text{cas}} S_{21}^{\text{cas}} A_1 \Gamma_{\text{P2}} D_1 D_4 + S_{32}^{\text{cas}} S_{24}^{\text{cas}} A_4 \Gamma_{\text{P2}} D_1 D_4 \tag{3.1.33}$$

Complex constants D_1, D_2, D_3 and D_4 are given by (3.1.34)–(3.1.37).

$$D_1 = \frac{1}{1 - S_{22}^{\text{cas}} \Gamma_{\text{P2}}} \tag{3.1.34}$$
$$D_2 = \frac{1}{1 - S_{33}^{\text{cas}} \Gamma_{\text{P3}}} \tag{3.1.35}$$
$$D_3 = \frac{1}{1 - S_{22}^{\text{cas}} \Gamma_{\text{P2}} - S_{23}^{\text{cas}} S_{32}^{\text{cas}} \Gamma_{\text{P2}} \Gamma_{\text{P3}} D_2} \tag{3.1.36}$$
$$D_4 = \frac{1}{1 - S_{33}^{\text{cas}} \Gamma_{\text{P3}} - S_{23}^{\text{cas}} S_{32}^{\text{cas}} \Gamma_{\text{P2}} \Gamma_{\text{P3}} D_1} \tag{3.1.37}$$

Notice that both B_2 and B_3 are functions of A_1, A_4, Γ_{P2}, and Γ_{P3} only. These two equations can be used to obtain the final formulas (3.1.38), (3.1.39) for B_1 and B_4. The S-parameters of the degenerated two-port, described by S-matrix $\boldsymbol{S}^{\text{D41}}$, are given by (3.1.40)–(3.1.41). Comparing (3.1.40) and (3.1.41) with (3.1.38) and (3.1.39), the individual elements of the $\boldsymbol{S}^{\text{D41}}$ matrix, formulas (3.1.42)–(3.1.45), can be derived.

$$\begin{aligned} B_1 = A_1 (& S_{11}^{\text{cas}} + S_{12}^{\text{cas}} S_{21}^{\text{cas}} \Gamma_{\text{P2}} D_3 + S_{13}^{\text{cas}} S_{31}^{\text{cas}} \Gamma_{\text{P3}} D_4 + \\ & S_{12}^{\text{cas}} S_{23}^{\text{cas}} S_{31}^{\text{cas}} \Gamma_{\text{P2}} \Gamma_{\text{P3}} D_2 D_3 + S_{13}^{\text{cas}} S_{32}^{\text{cas}} S_{21}^{\text{cas}} \Gamma_{\text{P2}} \Gamma_{\text{P3}} D_1 D_4) + \\ & A_4 (S_{14}^{\text{cas}} + S_{12}^{\text{cas}} S_{24}^{\text{cas}} \Gamma_{\text{P2}} D_3 + S_{13}^{\text{cas}} S_{34}^{\text{cas}} \Gamma_{\text{P3}} D_4 + \\ & S_{12}^{\text{cas}} S_{23}^{\text{cas}} S_{34}^{\text{cas}} \Gamma_{\text{P2}} \Gamma_{\text{P3}} D_2 D_3 + S_{13}^{\text{cas}} S_{32}^{\text{cas}} S_{24}^{\text{cas}} \Gamma_{\text{P2}} \Gamma_{\text{P3}} D_1 D_4) \end{aligned} \tag{3.1.38}$$

$$\begin{aligned} B_4 = A_1 (& S_{41}^{\text{cas}} + S_{42}^{\text{cas}} S_{21}^{\text{cas}} \Gamma_{\text{P2}} D_3 + S_{43}^{\text{cas}} S_{31}^{\text{cas}} \Gamma_{\text{P3}} D_4 + \\ & S_{42}^{\text{cas}} S_{23}^{\text{cas}} S_{31}^{\text{cas}} \Gamma_{\text{P2}} \Gamma_{\text{P3}} D_2 D_3 + S_{43}^{\text{cas}} S_{32}^{\text{cas}} S_{21}^{\text{cas}} \Gamma_{\text{P2}} \Gamma_{\text{P3}} D_1 D_4) + \\ & + A_4 (S_{44}^{\text{cas}} + S_{42}^{\text{cas}} S_{24}^{\text{cas}} \Gamma_{\text{P2}} D_3 + S_{43}^{\text{cas}} S_{34}^{\text{cas}} \Gamma_{\text{P3}} D_4 + \\ & S_{42}^{\text{cas}} S_{23}^{\text{cas}} S_{34}^{\text{cas}} \Gamma_{\text{P2}} \Gamma_{\text{P3}} D_2 D_3 + S_{43}^{\text{cas}} S_{32}^{\text{cas}} S_{24}^{\text{cas}} \Gamma_{\text{P2}} \Gamma_{\text{P3}} D_1 D_4) \end{aligned} \tag{3.1.39}$$

$$B_1 = S_{11}^{\text{D41}} A_1 + S_{14}^{\text{D41}} A_4 \tag{3.1.40}$$
$$B_4 = S_{41}^{\text{D41}} A_1 + S_{44}^{\text{D41}} A_4 \tag{3.1.41}$$

$$S_{11}^{\mathrm{D41}} = S_{11}^{\mathrm{cas}} + S_{12}^{\mathrm{cas}} S_{21}^{\mathrm{cas}} \Gamma_{\mathrm{P2}} D_3 + S_{13}^{\mathrm{cas}} S_{31}^{\mathrm{cas}} \Gamma_{\mathrm{P3}} D_4 + \Gamma_{\mathrm{P2}} \Gamma_{\mathrm{P3}} \left(S_{12}^{\mathrm{cas}} S_{23}^{\mathrm{cas}} S_{31}^{\mathrm{cas}} D_2 D_3 + S_{13}^{\mathrm{cas}} S_{32}^{\mathrm{cas}} S_{21}^{\mathrm{cas}} D_1 D_4 \right) \tag{3.1.42}$$

$$S_{14}^{\mathrm{D41}} = S_{14}^{\mathrm{cas}} + S_{12}^{\mathrm{cas}} S_{24}^{\mathrm{cas}} \Gamma_{\mathrm{P2}} D_3 + S_{13}^{\mathrm{cas}} S_{34}^{\mathrm{cas}} \Gamma_{\mathrm{P3}} D_4 + \Gamma_{\mathrm{P2}} \Gamma_{\mathrm{P3}} \left(S_{12}^{\mathrm{cas}} S_{23}^{\mathrm{cas}} S_{34}^{\mathrm{cas}} D_2 D_3 + S_{13}^{\mathrm{cas}} S_{32}^{\mathrm{cas}} S_{24}^{\mathrm{cas}} D_1 D_4 \right) \tag{3.1.43}$$

$$S_{41}^{\mathrm{D41}} = S_{41}^{\mathrm{cas}} + S_{42}^{\mathrm{cas}} S_{21}^{\mathrm{cas}} \Gamma_{\mathrm{P2}} D_3 + S_{43}^{\mathrm{cas}} S_{31}^{\mathrm{cas}} \Gamma_{\mathrm{P3}} D_4 + \Gamma_{\mathrm{P2}} \Gamma_{\mathrm{P3}} \left(S_{42}^{\mathrm{cas}} S_{23}^{\mathrm{cas}} S_{31}^{\mathrm{cas}} D_2 D_3 + S_{43}^{\mathrm{cas}} S_{32}^{\mathrm{cas}} S_{21}^{\mathrm{cas}} D_1 D_4 \right) \tag{3.1.44}$$

$$S_{44}^{\mathrm{D41}} = S_{44}^{\mathrm{cas}} + S_{42}^{\mathrm{cas}} S_{24}^{\mathrm{cas}} \Gamma_{\mathrm{P2}} D_3 + S_{43}^{\mathrm{cas}} S_{34}^{\mathrm{cas}} \Gamma_{\mathrm{P3}} D_4 + \Gamma_{\mathrm{P2}} \Gamma_{\mathrm{P3}} \left(S_{42}^{\mathrm{cas}} S_{23}^{\mathrm{cas}} S_{34}^{\mathrm{cas}} D_2 D_3 + S_{43}^{\mathrm{cas}} S_{32}^{\mathrm{cas}} S_{24}^{\mathrm{cas}} D_1 D_4 \right) \tag{3.1.45}$$

$$\boldsymbol{S}^{\mathrm{D41}} = \begin{pmatrix} S_{11}^{\mathrm{D41}} & S_{14}^{\mathrm{D41}} \\ S_{41}^{\mathrm{D41}} & S_{44}^{\mathrm{D41}} \end{pmatrix} \tag{3.1.46}$$

It is clear that all elements of the $\boldsymbol{S}^{\mathrm{D41}}$ matrix (3.1.46) depend on the same complex constants D_1, D_2, D_3, and D_4, as well as reflection coefficients Γ_{P2} and Γ_{P3}, and have a similar form. Moreover, the degenerated S-matrices $\boldsymbol{S}^{\mathrm{D43}}$, $\boldsymbol{S}^{\mathrm{D21}}$ and $\boldsymbol{S}^{\mathrm{D23}}$ can be derived by a similar procedure and show the same form of equations. Therefore, it is possible to express a single equation (3.1.47) which describes the individual elements of all degenerated two-port S-matrices $\boldsymbol{S}^{\mathrm{D}ji}$.

$$S_{uv}^{\mathrm{D}ji} = S_{uv}^{\mathrm{cas}} + S_{vs}^{\mathrm{cas}} S_{sv}^{\mathrm{cas}} \Gamma_s H_{st} + S_{ut}^{\mathrm{cas}} S_{tv}^{\mathrm{cas}} \Gamma_t H_{ts} + \Gamma_s \Gamma_t \left(S_{us}^{\mathrm{cas}} S_{tv}^{\mathrm{cas}} S_{st}^{\mathrm{cas}} H_{st} H_t + S_{ut}^{\mathrm{cas}} S_{ts}^{\mathrm{cas}} S_{sv}^{\mathrm{cas}} H_{ts} H_s \right) \tag{3.1.47}$$

$$u \in \{i, j\}, v \in \{i, j\} \tag{3.1.48}$$

$$\boldsymbol{S}^{\mathrm{D}ji} = \begin{pmatrix} S_{u=i,v=i}^{\mathrm{D}ji} & S_{u=i,v=j}^{\mathrm{D}ji} \\ S_{u=j,v=i}^{\mathrm{D}ji} & S_{u=j,v=j}^{\mathrm{D}ji} \end{pmatrix} = \begin{pmatrix} S_{ii}^{\mathrm{D}ji} & S_{ij}^{\mathrm{D}ji} \\ S_{ji}^{\mathrm{D}ji} & S_{jj}^{\mathrm{D}ji} \end{pmatrix} \tag{3.1.49}$$

$$H_t = \frac{1}{1 - S_{tt}^{\mathrm{cas}} \Gamma_t} \tag{3.1.50}$$

$$H_s = \frac{1}{1 - S_{ss}^{\mathrm{cas}} \Gamma_s} \tag{3.1.51}$$

$$H_{st} = \frac{1}{1 - S_{ss}^{\mathrm{cas}} \Gamma_s - S_{st}^{\mathrm{cas}} S_{ts}^{\mathrm{cas}} \Gamma_s \Gamma_t H_t} \tag{3.1.52}$$

$$H_{ts} = \frac{1}{1 - S_{tt}^{\mathrm{cas}} \Gamma_t - S_{st}^{\mathrm{cas}} S_{ts}^{\mathrm{cas}} \Gamma_s \Gamma_t H_s} \tag{3.1.53}$$

Indices s and t correspond to the unused ports of the H1-filter-H2 cascade terminated with reflection coefficients Γ_s and Γ_t, respectively. Their values, the same as the values of the i and j indices, depend on the chosen measurement type, see Table 3.1. To compute all four elements of the degenerated S-matrix $\boldsymbol{S}^{\mathrm{D}ji}$, with input port i and output port j, indices u and v must attain values according to (3.1.48), while the resulting matrix is organized according to (3.1.49). Auxiliary complex variables H_{st}, H_{ts}, H_t, and H_s are defined by formulas (3.1.50)–(3.1.53).

This general approach for characterization of a professional three-wire EMI/RFI filters in their stop-band in terms of the minimum insertion loss values was published in [24].

3.2 Extreme impedances - interferometric method analysis

The main purpose of this section is to quantitatively analyze the microwave measurements of extreme impedances based on interferometric approaches in terms of fundamental limits influencing both the achievable DUT measurement accuracy and precision. Phenomena as mounting repeatability of a standard or a DUT, calibration standards characterization or selection, phase noise, noise floor, and real hardware influence are studied in detail by means of two independent methods, Monte Carlo simulations (MCS) and the law of uncertainty propagation (LUP).

First, a general measurement model, describing interferometric measurement methods including the influence of different sources of uncertainties, will be developed and, subsequently, used in a simplified form for illustration of uncertainties propagation and derivation of basic limits influencing the measurements.

3.2.1 Measurement model derivation

The goal is to derive, in contrast to (2.2.1) and (2.2.3), a more general equation, describing the transmission coefficient T_{21} of interferometric approaches that could be used for an illustrative demonstration of interferometric methods behavior and limits. To achieve generality the measurement model is expanded by sources of high-level multiplicative noise and low-level additive noise since they influence every measurement and, especially, achievable DUT measurement accuracy and precision. High-level multiplicative noise – e.g., phase noise and phase stability of coaxial cables – is directly proportional to the magnitude of a useful signal that is generated by a microwave generator. On the other hand, low-level additive noise does not depend on the state of the useful signal, e.g., the noise floor that is generated internally in RF devices and materials by the random motion of charges or charge carriers, [31].

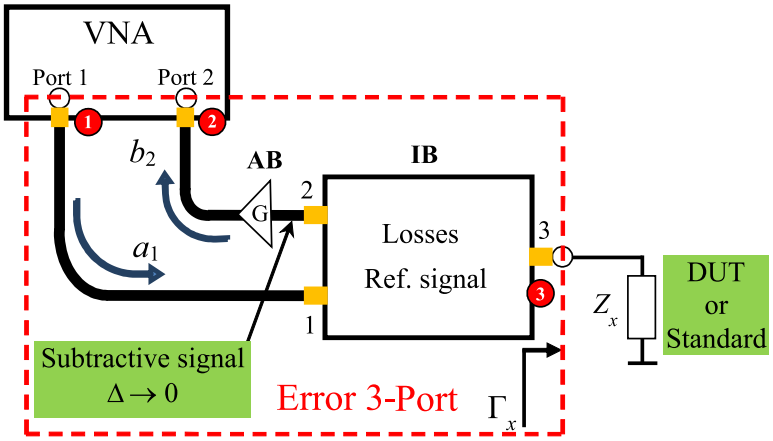

Figure 3.7: General setup for a microwave measurement of extreme impedances Z_x.

The general measurement setup consists of a VNA, a measured impedance Z_x, an amplification box (**AB**), and an interferometric box (**IB**), see Figure 3.7. The interferometric box (**IB**) can be any lossless or low loss circuit that can produce an extremely small differential signal Δ, containing information about Γ_x at its respective port 2.

The **AB** is a two-port created by an amplifier(s) operating in a linear regime, typically with low noise amplifiers (LNAs). On the other hand, the **IB** is generally an N-port,

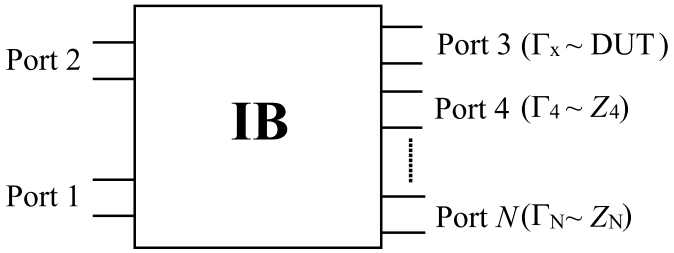

Figure 3.8: Interferometric box.

$N \geq 3$, see Figure 3.8, whose transmission coefficient Δ between ports Port 1 and Port 2 is given by the interference of at least two signals – a signal corresponding to the measured coefficient Γ_x and any resulting interfering reference signal.

From the resulting DUT measurement uncertainty point of view, the goal is to create as small Δ as possible with hardware that is stable in time and does not cause any additional uncertainty of the transmission coefficient Δ except the finite mounting repeatability of measured Γ_x. Therefore, all possible hardware solutions of the **IB** can be, in principle, degenerated to a general three-port. Consequently, the whole measurement setup can be described by the connection of one three-port **IB** and one two-port **AB**, see the measurement model in Figure 3.9.

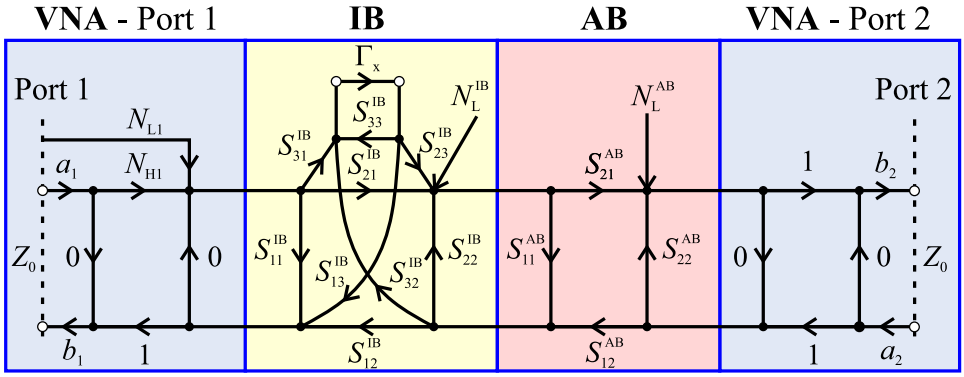

Figure 3.9: General measurement model, corresponding to the measurement setup in Figure 3.7, including the implementation of high-level multiplicative noise N_H and low-level additive noise N_L.

To derive the general transmission coefficient depending on high-level multiplicative noise N_{H} and low-level additive noise N_{L} the measurement model was expanded, see Figure 3.9. A similar noise implementation was proposed in METAS, see [32,33]. Unlike [32], more detailed implementation based rather on physical nature of the noise sources is proposed to see the true potential of interferometric approaches. Most importantly, an implementation of the VNA reference channel and its dependence on noise sources is proposed in order to derive the DUT uncertainty dependence on $a_{1\mathrm{R}}$ in following section. N_{H} characterizes the phase noise of microwave synthesizer at the Port 1 and since it is directly proportional to the generated signal, it is simply defined as a Gaussian-distributed signal with unity mean vector, (3.2.1), suffering from an error/uncertaitny. N_{L} characterizes the noise floor generated by the VNA at the Port 1. $N_{\mathrm{L}}^{\mathbf{IB}}$ and $N_{\mathrm{L}}^{\mathbf{AB}}$ stand for noise voltages generated internally by networks **IB** and **AB**, respectively. $N_{\mathrm{L}}^{\mathrm{T}}$ and $N_{\mathrm{L}}^{\mathrm{R}}$ characterize ad-

ditive sources of noise caused by VNA receivers in the test and the reference channel, respectively. All sources of additive noise, N_{L}, are signals with zero average value but nonzero root mean square (rms) value, see [31]. They do not depend on the state of the generated signal and create the source of the error/uncertainty only, therefore, they are defined as Gaussian-distributed signals with zero mean vectors, (3.2.1), suffering from an error/uncertainty. It should be noted that noise sources N_{H} and N_{L} are assumed to be the same in both the test and the reference channel since they are derived from the same microwave source.

$$\begin{aligned} \mu\left(N_{\mathrm{H}}\right) &= 1e^{j0} \\ \mu\left(N_{\mathrm{L}}\right) &= 0e^{j0} \end{aligned} \tag{3.2.1}$$

Based on the measurement model in Figure 3.9 it is possible to derive, using the well-known Mason's rule, a more general equation for the transmission coefficient:

$$T_{21}^{\mathrm{G}} = \frac{b_2}{a_{1\mathrm{R}}} = \frac{S_{21}^{\mathrm{IB}'} S_{21}^{\mathrm{AB}'} \left(N_{\mathrm{H}} a_1 + N_{\mathrm{L}}\right) + S_{21}^{\mathrm{AB}'} N_{\mathrm{L}}^{\mathrm{IB}} + N_{\mathrm{L}}^{\mathrm{AB}} + N_{\mathrm{L}}^{T}}{a_{1\mathrm{R}}}. \tag{3.2.2}$$

The exact expression of $a_{1\mathrm{R}}$ and its dependence on incident wave a_1, transmission coefficient S_{21}^{R} of the reference channel, and noise sources $N_{\mathrm{H}}, N_{\mathrm{L}}$, and $N_{\mathrm{L}}^{\mathrm{R}}$, is shown in Figure 3.9. Nevertheless, such a detailed expression goes beyond the scope of this thesis and it is insignificant for uncertainty analysis purposes performed in the following section. Therefore, only $a_{1\mathrm{R}}$ suffering from an uncertainty will be further assumed. Parameter $S_{21}^{\mathrm{IB}'}$ in (3.2.2) expresses the small subtractive signal created by **IB** with respect to the 50-Ω impedance at its respective port 2

$$S_{21}^{\mathrm{IB}'} = \frac{S_{21}^{\mathrm{IB}} \left(1 - S_{33}^{\mathrm{IB}} \Gamma_{\mathrm{x}}\right) + S_{31}^{\mathrm{IB}} S_{23}^{\mathrm{IB}} \Gamma_{\mathrm{x}}}{1 - S_{33}^{\mathrm{IB}} \Gamma_{\mathrm{x}}}, \tag{3.2.3}$$

and parameter $S_{21}^{\mathrm{AB}'}$ in (3.2.2) stands for the transmission coefficient of **AB** including the impedance mismatch at its respective port 1.

$$S_{21}^{\mathrm{AB}'} = \frac{S_{21}^{\mathrm{AB}} \left(1 - S_{33}^{\mathrm{IB}} \Gamma_{\mathrm{x}}\right)}{1 - S_{33}^{\mathrm{IB}} \Gamma_{\mathrm{x}} - S_{11}^{\mathrm{AB}} \left[S_{22}^{\mathrm{IB}} + \Gamma_{\mathrm{x}} \left(S_{32}^{\mathrm{IB}} S_{23}^{\mathrm{IB}} - S_{22}^{\mathrm{IB}} S_{33}^{\mathrm{IB}}\right)\right]} \tag{3.2.4}$$

The equation (3.2.2) is a general expression of transmission coefficient T_{21}^{G} describing the realistic behavior of the VNA measurement. The useful signal is characterized by the first term $S_{21}^{\mathrm{IB}'} S_{21}^{\mathrm{AB}'} N_{\mathrm{H}}$ only and the rest represents the noise floor at port 2 of the VNA. Both signals exist independently of each other and depend on the **IB** and **AB** hardware.

3.2.2 Simplified transmission coefficient analysis

The goal of this section is to demonstrate, by means of uncertainty analysis, the behavior and limits of the interferometric measurement method described by (3.2.2). To simply explain and illustrate the limits of the method studied it is necessary to assume partly ideal hardware and simplify (3.2.2) neglecting terms of low importance. Therefore, an ideally matched **AB** $\left(S_{11}^{\mathrm{AB}} \to 0\right)$ and ideally matched **IB** respective port 3 $\left(S_{33}^{\mathrm{IB}} \to 0\right)$ are assumed. It enables to neglect the $S_{21}^{\mathrm{AB}'}$ dependence on Γ_{x} and partly $S_{21}^{\mathrm{IB}'}$ dependence on Γ_{x}, see (3.2.5).

$$\begin{aligned} S_{21}^{\mathrm{IB}'} &= S_{21}^{\mathrm{IB}} + S_{31}^{\mathrm{IB}} S_{23}^{\mathrm{IB}} \Gamma_{\mathrm{x}} \\ S_{21}^{\mathrm{AB}'} &= S_{21}^{\mathrm{AB}} \end{aligned} \tag{3.2.5}$$

Both simplifications are fulfilled, for instance, for an ideal amplifier and ideal 180° 3dB hybrid in Figure 2.2. After the substitution of (3.2.5) into (3.2.2) the simplified transmission coefficient can be expressed as:

$$T_{21}^{'} = \frac{b_2^{'}}{a_{1\mathrm{R}}} = \frac{S_{21}^{\mathrm{AB}} \left(S_{21}^{\mathrm{IB}} + \Gamma_{\mathrm{x}} S_{31}^{\mathrm{IB}} S_{23}^{\mathrm{IB}} \right) \left(N_{\mathrm{H}} a_1 + N_{\mathrm{L}} \right) + S_{21}^{\mathrm{AB}} N_{\mathrm{L}}^{\mathrm{IB}} + N_{\mathrm{L}}^{\mathrm{AB}} + N_{\mathrm{L}}^{T}}{a_{1\mathrm{R}}}. \tag{3.2.6}$$

Further, three substitutions $S_{21}^{\mathrm{AB}} = G$, $S_{21}^{\mathrm{IB}} = S_{\mathrm{ref}}$, and $S_{31}^{\mathrm{IB}} S_{23}^{\mathrm{IB}} = \frac{1}{A} e^{j\varphi}$ will be used to simplify the notation of (3.2.6) for subsequent analysis. The S-parameter S_{21}^{IB} expresses interfering signal S_{ref} and is generally created by both the internal transmission between **IB** respective ports, Port 1 and Port 2, and the contribution of impedances $Z_4, Z_5, ..., Z_N$ connected to Ports $4, 5, ..., N$, see the general schematic of the **IB** in Figure 3.8. The transmission coefficient $S_{31}^{\mathrm{IB}} S_{23}^{\mathrm{IB}}$ through the **IB** that corresponds to the measured Γ_{x} signal will be further expressed using scalar quantity A representing a decrease of the Γ_{x} path inside the **IB** structure and a corresponding phase shift φ. Using all substitutions the equation (3.2.6) simplifies to:

$$T_{21}^{\prime} = \frac{G \left(S_{\mathrm{ref}} + \frac{\Gamma_x}{A} e^{j\varphi} \right) \left(N_{\mathrm{H}} a_1 + N_{\mathrm{L}} \right) + G N_{\mathrm{L}}^{\mathrm{IB}} + N_{\mathrm{L}}^{\mathrm{AB}} + N_{\mathrm{L}}^{T}}{a_{1\mathrm{R}}}. \tag{3.2.7}$$

Finally, using substitution

$$\Delta = S_{\mathrm{ref}} + \frac{\Gamma_{\mathrm{x}}}{A} e^{j\varphi}, \tag{3.2.8}$$

(3.2.7) can be rewritten as

$$T_{21}^{'} = \frac{1}{a_{1\mathrm{R}}} \left[G\Delta \left(N_{\mathrm{H}} a_1 + N_{\mathrm{L}} \right) + G N_{\mathrm{L}}^{\mathbf{IB}} + N_{\mathrm{L}}^{\mathbf{AB}} + N_{\mathrm{L}}^{T} \right], \tag{3.2.9}$$

where parameter Δ, introduced in previous Section 3.2.1, expresses small subtractive signal given by interference of S_{ref} and Γ_{x} signal. The equation (3.2.9) represents the desired simplified measured transmission coefficient suitable for the uncertainty analysis.

To analyze the method in terms of measurement accuracy and precision it is suitable to work with uncertainties u using variance-covariance matrices $\mathbf{V}(Y)$ of complex quantities $Y = a + jb$ in a rectangular coordinate system Re-Im, see [34].

$$\mathbf{V}(Y) = \begin{pmatrix} u(a)^2 & u(a,b) \\ u(b,a) & u(b)^2 \end{pmatrix}. \tag{3.2.10}$$

Uncertainties $u(a)$ and $u(b)$ in the real and the imaginary part of Y, respectively, are square root of the variances $u(a)^2$ and $u(b)^2$ in $\mathbf{V}(Y)$. $u(a,b) = u(b,a)$ and expresses the correlation between real and imaginary part of Y. It will be further supposed that all quantities Y have a bivariate normal/Gaussian distribution $Y \sim N_2(\mu(Y), \mathbf{V}(Y))$ described by mean vector $\mu(Y)$ and a variance-covariance matrix $\mathbf{V}(Y)$. In this two-dimensional case the multivariate probability distribution, [35], generally forms an ellipse in the Re-Im plane.

To analyze (3.2.7), the dependence of T'_{21} uncertainty expressed by $\mathbf{V}\left(T'_{21}\right)$ on all quantities, that influence measured T'_{21} and suffer from uncertainties, is derived. Further, the propagation of $\mathbf{V}\left(T'_{21}\right)$ into resulting uncertainty $\mathbf{V}\left(\Gamma_{\mathrm{x}}\right)$ of measured Γ_{x} is derived and the result is compared with (2.2.2).

For uncertainty analysis purposes T'_{21} must be separated into two equations f_1 and f_2 for the real and imaginary parts. Both f_1 and f_2 are functions of input variables $\mathbf{x} = \left\{\Gamma_x, S_{\mathrm{ref}}, G, A, N_{\mathrm{H}}, N_{\mathrm{L}}, N_{\mathrm{L}}^{\mathrm{IB}}, N_{\mathrm{L}}^{\mathrm{AB}}, N_{\mathrm{L}}^{\mathrm{T}}, a_1, a_{1\mathrm{R}}\right\}$:

$$T'_{21} = f\left(\mathbf{x}\right) = f_1\left(\mathbf{x}\right) + \mathrm{j}f_2\left(\mathbf{x}\right). \tag{3.2.11}$$

This analysis specifically includes the influence of the phase noise of the microwave synthesizer expressed by unity mean vector $\mu\left(N_{\mathrm{H}}\right) = 1e^{j0}$ and $\mathbf{V}\left(N_{\mathrm{H}}\right)$ and the noise floor at the Port 1 given by zero mean vector $\mu\left(N_{\mathrm{L}}\right) = 0e^{j0}$ and $\mathbf{V}\left(N_{\mathrm{L}}\right)$, see noise definition (3.2.1) in Section 3.2.1. Further, the noises produced internally by **IB** and **AB** hardware that are expressed by zero mean vectors $\mu\left(N_{\mathrm{L}}^{\mathrm{IB}}\right) = 0e^{j0}$ and $\mu\left(N_{\mathrm{L}}^{\mathrm{AB}}\right) = 0e^{j0}$ and their variance-covariance matrices $\mathbf{V}\left(N_{\mathrm{L}}^{\mathrm{IB}}\right)$ and $\mathbf{V}\left(N_{\mathrm{L}}^{\mathrm{AB}}\right)$, respectively, are also included. Moreover, the additional measurement uncertainty of the VNA receiver in the test channel expressed by $\mu\left(N_{\mathrm{L}}^{\mathrm{T}}\right) = 0e^{j0}$ and $\mathbf{V}\left(N_{\mathrm{L}}^{\mathrm{T}}\right)$ and the influence of the reference channel expressed by $\mu\left(a_{1\mathrm{R}}\right) = a_{1\mathrm{R}}$ and $\mathbf{V}\left(a_{1\mathrm{R}}\right)$ are taken into an account. Finally, mounting repeatability of a DUT connection expressed by $\mu\left(\Gamma_{\mathrm{x}}\right) = \Gamma_{\mathrm{x}}$ and $\mathbf{V}^{\mathrm{MR}}\left(\Gamma_{\mathrm{x}}\right)$ is assumed.

To compute the T'_{21} measurement uncertainty expressed by $\mathbf{V}\left(T'_{21}\right)$ the LUP in matrix form is applied:

$$\mathbf{V}\left(T'_{21}\right) = \mathbf{J}\left(T'_{21}\right)\mathbf{V}\left(\mathbf{x}_1\right)\mathbf{J}\left(T'_{21}\right)^{\mathrm{T}}. \tag{3.2.12}$$

The matrix $\mathbf{V}\left(\mathbf{x}_1\right)$ is a variance-covariance matrix of input quantities suffering from uncertainties $\mathbf{x}_1 = \left\{\Gamma_x, N_{\mathrm{H}}, N_{\mathrm{L}}, N_{\mathrm{L}}^{\mathrm{IB}}, N_{\mathrm{L}}^{\mathrm{AB}}, N_{\mathrm{L}}^{\mathrm{T}}, a_{1\mathrm{R}}\right\} \subseteq \mathbf{x}$. Further, $\mathbf{V}\left(\mathbf{x}_1\right)$ is a diagonal matrix since individual input quantities $\mathbf{x}_1$ are supposed to be mutually not correlated, see (3.2.13). The other quantities $S_{\mathrm{ref}}, G, A, a_1$ do not have to be included since they are supposed to be constant and have zero variance-covariance matrices.

$$\mathbf{V}\left(\mathbf{x}_1\right) = \begin{pmatrix} \mathbf{V}^{\mathrm{MR}}\left(\Gamma_{\mathrm{x}}\right) & \cdots & 0 \\ \vdots & \ddots & \vdots \\ 0 & \cdots & \mathbf{V}\left(a_{1\mathrm{R}}\right) \end{pmatrix} \tag{3.2.13}$$

The jacobian matrix $\mathbf{J}\left(T'_{21}\right)$ in (3.2.12) is the matrix of first-order partial derivatives of $T_{21}^{\mathrm{G}'}$ with respect to $\mathbf{x}_1$ and is given by

$$\mathbf{J}\left(T'_{21}\right) = \frac{\partial T'_{21}}{\partial \mathbf{x}_1} = \begin{pmatrix} \frac{\partial T'_{21}}{\partial \Gamma_{\mathrm{x}}} & \cdots & \frac{\partial T'_{21}}{\partial a_{1\mathrm{R}}} \end{pmatrix}. \tag{3.2.14}$$

The result of each partial derivative in (3.2.14) is a 2x2 matrix. After the substitution of (3.2.13) and (3.2.14) into (3.2.12) the variance-covariance matrix $\mathbf{V}\left(T'_{21}\right)$ can be expressed as:

$$\begin{aligned} \mathbf{V}\left(T'_{21}\right) = &\left(\frac{\partial T'_{21}}{\partial \Gamma_{\mathrm{x}}}\right)\mathbf{V}^{\mathrm{MR}}\left(\Gamma_{\mathrm{x}}\right)\left(\frac{\partial T'_{21}}{\partial \Gamma_{\mathrm{x}}}\right)^{\mathrm{T}} + \ldots \\ +&\left(\frac{\partial T'_{21}}{\partial N_{\mathrm{L}}^{\mathrm{T}}}\right)\mathbf{V}\left(N_{\mathrm{L}}^{\mathrm{T}}\right)\left(\frac{\partial T'_{21}}{\partial N_{\mathrm{L}}^{\mathrm{T}}}\right)^{\mathrm{T}} + \left(\frac{\partial T'_{21}}{\partial a_{1\mathrm{R}}}\right)\mathbf{V}\left(a_{1\mathrm{R}}\right)\left(\frac{\partial T'_{21}}{\partial a_{1\mathrm{R}}}\right)^{\mathrm{T}}. \end{aligned} \tag{3.2.15}$$

The last two terms including $\mathbf{V}\left(N_{\mathrm{L}}^{\mathrm{T}}\right)$ and $\mathbf{V}\left(a_{1\mathrm{R}}\right)$ in (3.2.15) contribute to the measurement uncertainty caused mostly by the VNA itself and are further addressed as VNA measurement uncertainty expressed by variance-covariance matrix $\mathbf{V}^{\mathrm{VNA}}$. In most practical applications $\mathbf{V}^{\mathrm{VNA}}$ is dominantly influenced by the phase noise in the reference channel. It should be noted that the contribution of $\mathbf{V}\left(a_{1\mathrm{R}}\right)$ to $\mathbf{V}^{\mathrm{VNA}}$ also depends on the **IB** and **AB** hardware used in the test channel due to the partial derivative of $T_{21}^{'}$ with respect to $a_{1\mathrm{R}}$ in (3.2.15). The exact expression of $\mathbf{V}^{\mathrm{VNA}}$ is beyond the scope of this thesis and, therefore, it is omitted. To get the final equation for $\mathbf{V}\left(T_{21}^{'}\right)$ all partial derivatives in (3.2.15) must be computed, see (3.2.16).

$$\begin{aligned}\mathbf{V}\left(T_{21}^{'}\right) = \tfrac{|G|^2}{A^2}\left[\tfrac{|a_1|^2}{|a_{1\mathrm{R}}|^2}\tilde{\mathbf{V}}^{\mathrm{MR}}\left(\Gamma_{\mathrm{x}}\right)\right] + \\ +|G\Delta|^2\left[\tfrac{|a_1|^2}{|a_{1\mathrm{R}}|^2}\tilde{\mathbf{V}}\left(N_{\mathrm{H}}\right) + \tfrac{1}{|a_{1\mathrm{R}}|^2}\tilde{\mathbf{V}}\left(N_{\mathrm{L}}\right)\right] + \\ +\tfrac{|G|^2}{|a_{1\mathrm{R}}|^2}\tilde{\mathbf{V}}\left(N_{\mathrm{L}}^{\mathbf{IB}}\right) + \tfrac{1}{|a_{1\mathrm{R}}|^2}\tilde{\mathbf{V}}\left(N_{\mathrm{L}}^{\mathbf{AB}}\right) + \mathbf{V}^{\mathrm{VNA}}\end{aligned} \tag{3.2.16}$$

The notation with a tilde, for instance $\tilde{\mathbf{V}}^{\mathrm{MR}}\left(\Gamma_{\mathrm{x}}\right)$, expresses the rotation of the joint probability distribution (an ellipse), given by $\mathbf{V}^{\mathrm{MR}}$, around the origin of the Re-Im coordinate system. An example of a computation of the first term in (3.2.15) is shown in Appendix A. It can be seen that $\mathbf{V}\left(T_{21}^{'}\right)$ is strongly dependent on amplifier gain G.

Further, when $\mathbf{V}\left(T_{21}^{'}\right)$ dependence on all uncertainty sources is known, Γ_{x} can be expressed from (3.2.7)

$$\Gamma_{\mathrm{x}} = \frac{A}{G}\frac{1}{e^{j\varphi}}\left(\frac{a_{1\mathrm{R}}T_{21}^{'} - GN_{\mathrm{L}}^{\mathbf{IB}} - N_{\mathrm{L}}^{\mathbf{AB}} - N_{\mathrm{L}}^{\mathrm{T}}}{\left(N_{\mathrm{H}}a_1 + N_{\mathrm{L}}\right)} - GS_{\mathrm{ref}}\right) \tag{3.2.17}$$

and, subsequently, only the uncertainty propagation of $T_{21}^{'}$, expressed by $\mu\left(T_{21}^{'}\right) = T_{21}^{'}$ and $\mathbf{V}\left(T_{21}^{'}\right)$, through mean values of all remaining parameters influencing Γ_{x} is computed to derive the correct $\mathbf{V}\left(\Gamma_{\mathrm{x}}\right)$. Since the mean values of noise sources are equal to ones or zeros, see (3.2.1), all noise sources N_{H} and N_{L} in (3.2.17) can be omitted and Γ_{x} can be expressed as a function of the **IB** and **AB** hardware only:

$$\Gamma_{\mathrm{x}} = \frac{A}{a_1}\frac{1}{e^{j\varphi}}\left(\frac{T_{21}^{'}a_{1\mathrm{R}}}{G} - S_{\mathrm{ref}}a_1\right). \tag{3.2.18}$$

Now, $\mathbf{V}\left(\Gamma_{\mathrm{x}}\right)$ can be computed using

$$\mathbf{V}\left(\Gamma_{\mathrm{x}}\right) = \left(\frac{\partial\Gamma_{\mathrm{x}}}{\partial T_{21}^{'}}\right)\mathbf{V}\left(T_{21}^{'}\right)\left(\frac{\partial\Gamma_{\mathrm{x}}}{\partial T_{21}^{'}}\right)^{\mathrm{T}} = \ldots = \frac{A^2}{|G|^2}\frac{|a_{1\mathrm{R}}|^2}{|a_1|^2}\tilde{\mathbf{V}}\left(T_{21}^{'}\right). \tag{3.2.19}$$

Since the notation $\tilde{\mathbf{V}}\left(T_{21}^{'}\right)$ in (3.2.19) represents only the rotation of the joint probability distribution, given by $\mathbf{V}\left(T_{21}^{'}\right)$, this transformation can be omitted to simplify the equation for $\mathbf{V}\left(\Gamma_{\mathrm{x}}\right)$:

$$\mathbf{V}\left(\Gamma_{\mathrm{x}}\right) \approx \frac{A^2}{|G|^2}\frac{|a_{1\mathrm{R}}|^2}{|a_1|^2}\mathbf{V}\left(T_{21}^{'}\right). \tag{3.2.20}$$

After substitution of (3.2.16) into (3.2.20) the resulting uncertainty of measured reflection coefficient Γ_{x} can be expressed as:

$$\begin{array}{c}\mathbf{V}\left(\Gamma_{\mathrm{x}}\right)\approx A^{2}|\Delta|^{2}\left[\tilde{\mathbf{V}}\left(N_{\mathrm{H}}\right)+\frac{1}{|a_{1}|^{2}}\tilde{\mathbf{V}}\left(N_{\mathrm{L}}\right)\right]+\tilde{\mathbf{V}}^{\mathrm{MR}}\left(\Gamma_{\mathrm{x}}\right)+\\ +\frac{A^{2}}{|a_{1}|^{2}}\tilde{\mathbf{V}}\left(N_{\mathrm{L}}^{\mathrm{IB}}\right)+\frac{A^{2}}{|G|^{2}|a_{1}|^{2}}\left[\mathbf{V}\left(N_{\mathrm{L}}^{\mathrm{AB}}\right)+|a_{1\mathrm{R}}|^{2}\mathbf{V}^{\mathrm{VNA}}\right]\end{array}. \tag{3.2.21}$$

Now let us examine the resulting $\mathbf{V}\left(\Gamma_{\mathrm{x}}\right)$, compare it with the result of (2.2.2) and, subsequently, state general recommendations for microwave measurements based on the interferometric approaches. It can be seen in (3.2.20) that resulting uncertainties in the real and imaginary parts of Γ_{x}, included in $\mathbf{V}\left(\Gamma_{\mathrm{x}}\right)$, are $A/\left|G\right|$ times smaller than the uncertainties in $\mathbf{V}\left(T_{21}^{'}\right)$ since the uncertainty is the square root of the variance, as explained below (3.2.10). The factor $A/\left|G\right|$ should lie in the open interval $(0,1)$, otherwise the method does not suppress $\mathbf{V}\left(T_{21}^{'}\right)$. To clearly express the achievable suppression the uncertainty suppression limit SL^{HW} is defined as a multiplicative inverse of $A/\left|G\right|$:

$$SL^{\mathrm{HW}}=\frac{|G|}{A}. \tag{3.2.22}$$

SL^{HW} influences in (3.2.21) only the VNA measurement uncertainty $\mathbf{V}^{\mathrm{VNA}}$ caused predominantly by the phase noise in the VNA reference channel and $\mathbf{V}\left(N_{\mathrm{L}}^{\mathrm{AB}}\right)$ expressing the noise voltage generated at the output of **AB**, see [31] for more information about the noise generated by the amplifier. SL^{HW} depends on the properties of the chosen **IB** and **AB** hardware and has been already derived in [6], see (2.2.2), for an ideal amplifier and ideal 3dB 180° hybrid. Nevertheless, (2.2.2) cannot be treated as interferometric method performance since there are other sources of uncertainties present in the VNA test channel that can substantially influence the resulting $\mathbf{V}\left(\Gamma_{\mathrm{x}}\right)$. For instance, the uncertainty given by mounting repeatability, that is expressed by $\tilde{\mathbf{V}}^{\mathrm{MR}}\left(\Gamma_{\mathrm{x}}\right)$ in (3.2.21), cannot be suppressed by the method itself and will always create a lower bound for $\mathbf{V}\left(\Gamma_{\mathrm{x}}\right)$.

Further, $\tilde{\mathbf{V}}\left(N_{\mathrm{H}}\right)$ and $\tilde{\mathbf{V}}\left(N_{\mathrm{L}}\right)$ in (3.2.21), corresponding to uncertainties given by the phase noise and the noise floor at the VNA port 1, are being suppressed by $A\left|\Delta\right|$. The factor $A\left|\Delta\right|\in(0,1)$, otherwise, the interferometric method does not work. Similar to SL^{HW},the suppression limit SL^{IB} is defined as the multiplicative inverse of $A\left|\Delta\right|$:

$$SL^{\mathrm{IB}}=\frac{1}{A\left|\Delta\right|}=\frac{1}{A\left|S_{\mathrm{ref}}+\frac{\Gamma_{\mathrm{x}}}{A}e^{j\varphi}\right|}. \tag{3.2.23}$$

SL^{IB} is a fundamental suppression limit given by the IB hardware only. SL^{IB} shows the suppression of N_{H} and N_{L} in the VNA test channel. It can be deduced from (3.2.23) that without presence of an interfering signal S_{ref} the suppression limit $\left|SL^{\mathrm{IB}}\right|=1/|\Gamma_{\mathrm{x}}|\cong 1$ for high reflective DUTs and the method does not suppress N_{H} and N_{L}. To achieve high SL^{IB} the subtractive signal Δ and **IB** losses A should be as small as possible. To fulfil both conditions the **IB** must be lowloss and S_{ref} must be very similar in magnitude to the Γ_{x} signal and simultaneously to be out-of-phase with Γ_{x} signal.

$\tilde{\mathbf{V}}\left(N_{\mathrm{L}}^{\mathrm{IB}}\right)$ expresses uncertainty given by the noise voltage generated at the output of **IB** in (3.2.21). $\tilde{\mathbf{V}}\left(N_{\mathrm{L}}^{\mathrm{IB}}\right)$ is directly proportional to the **IB** dissipative losses and cannot be suppressed by the interferometric method. Since the dissipative losses are required to be as small as possible for **IB** hardware, $\tilde{\mathbf{V}}\left(N_{\mathrm{L}}^{\mathrm{IB}}\right)$ can be, in practically most cases, neglected among other sources of uncertainty.

Now, let us summarize the achieved results and state some practical measurement requirements and recommendations:

Generally speaking, the combination of **IB** and **AB** hardware enables to achieve better VNA measurement sensitivity/precision and suppresses sources of random errors in the VNA test channel in contrast to a common one-port reflection coefficient measurement. Due to the ability of noise suppression, it is possible to use a wider IF bandwidth and perform faster measurements and, at the same time, achieve comparable or even better measurement sensitivity in comparison to a common one-port measurement.

In the case of absolute measurements, where it is required to know the value of Γ_{x} accurately, the application of the interferometric method has a meaning only when the uncertainty given by by $\tilde{\mathbf{V}}^{\mathrm{MR}}(\Gamma_{\mathrm{x}})$ is substantially smaller than $\tilde{\mathbf{V}}(N_{\mathrm{H}})$, $\tilde{\mathbf{V}}(N_{\mathrm{L}})$ or $\mathbf{V}^{\mathrm{VNA}}$ in (3.2.21). From a measurement point of view, the measured Γ_{x}/DUTs must differ in reflection coefficient by at least one order more than the uncertainty caused by the mounting repeatability of the connection $\tilde{\mathbf{V}}^{\mathrm{MR}}(\Gamma_{\mathrm{x}})$ used, otherwise, the VNA will not distinguish them. Further, the value of the parameter $|\Delta|$, which depends on **IB** hardware and differences between measured Γ_{x}/DUTs and reference impedance Γ_{ref}, should be chosen so that $\tilde{\mathbf{V}}(N_{\mathrm{H}})$ and $\tilde{\mathbf{V}}(N_{\mathrm{L}})$ are suppressed below the level of $\tilde{\mathbf{V}}^{\mathrm{MR}}(\Gamma_{\mathrm{x}})$. Finally, the value of $|G|$ should be sufficiently high so that $\mathbf{V}^{\mathrm{VNA}}$ in (3.2.21) is suppressed below the level of $\tilde{\mathbf{V}}^{\mathrm{MR}}(\Gamma_{\mathrm{x}})$. The value of $|G\Delta|$ should be adjusted in the range of the transmission coefficients where the VNA measures most precisely, typically $T_{21}^{'} \in \langle 0, -40 \rangle$ dB, see e.g., the specification for ZVA 67 [36].

In the case of relative measurements, where it is not necessary to repeatedly connect the measured Γ_{x}/DUT, i.e., NSMM, and it is only required to distinguish several very similar Γ_{x}, the **IB** hardware should create as small $|\Delta|$ as possible since mounting repeatability $\tilde{\mathbf{V}}^{\mathrm{MR}}(\Gamma_{\mathrm{x}})$ does not limit $\mathbf{V}(\Gamma_{\mathrm{x}})$. Parameter $|\Delta|$ directly influences the improvement in measurement precision, see derived SL^{IB} in (3.2.23). Nevertheless, there is a lower bound for $|\Delta|$, even for ideal **IB**, and it is given by the noise generated internally by **AB**, i.e., $|G\Delta| \gg \mathbf{V}\left(N_{\mathrm{L}}^{\mathrm{AB}}\right)$. It means that the amplified subtractive signal $|G\Delta|$ must be higher than the amplified noise voltage, $\mathbf{V}\left(N_{\mathrm{L}}^{\mathrm{AB}}\right)$, generated by the **AB** itself. Parameter G of the **AB** should be chosen identically to the case of absolute measurements.

In conclusion, it should be noted that this analytical approach does not enable the calibration process that significantly influences the resulting DUT uncertainty to be included. On the other hand, it qualitatively expresses the fundamental uncertainty suppression coefficients and their dependence on the **IB** and **AB** hardware.

4 Results

This chapter presents achieved results. First part dedicated to the evaluation of minimum insertion loss of EMI/RFI filters in their stop band was published in journals [23, 24] and follows in work [7, 8] that was originally initiated by the National Security Authority in Czech Republic. Second part focused on extreme impedances measurement using interferometric approaches was supported by the European Metrology Research Programme (EMRP) - project SIB62 - and developed in cooperation with Czech Metrology Institute. Work related to a development and fabrication of calibration/verification standards, necessary for precise microwave measurement of extreme impedances, was published in conference papers [37–40] and is here only briefly mentioned due to the unsatisfactory results. Further, a virtual measurement, confirming derived theory related to the achievable measurement precision and accuracy, is presented and has been recently submitted to a journal.

4.1 EMI/RFI filters

A theoretical background for EMI/RFI filters characterization in their stop band in terms of the minimum insertion loss was introduced in Chapter 3. The presented approach is based on measured S-parameters evaluation.

Generally speaking, S-parameter measurements require a well-defined connection of any related EMI/RFI filter to suitable RF connectors with precisely defined Z_0 impedance. Since the filters are manufactured in a form that enables a simple and robust connection to standard (often thick) power-lines, it may be a technical problem. Some recommendations for the realization of proper adapters between 50 Ω measurement coaxial connectors and filter terminals can be found in [8]. The same adaptors were also used for the measurement of the real EMI/RFI filter.

Generally, any particular 3D configuration of wires connected to filter terminals influences overall filter parameters at high MHz or GHz frequencies. Determining EMI/RFI filter parameters, including the proposed Γ_{opt} method, corresponds to one specific wire configuration which cannot be changed throughout the measurements. On the other hand, the proposed method is valid for any specific wire configuration.

To eliminate this problem during the verification of the developed measurement-evaluation method a test filter formed by a cascade of three Mini-Circuits low-pass filters (VLF-800+, VLF-630+, and VLF-160+) equipped with SMA connectors was used. This combination shows extremely high insertion loss IL in the stop-band up to 20 GHz, enables a well-defined connection to the VNA, and simulates the non-symmetrical EMI/RFI filter with unequal S_{11} and S_{22} and, therefore, Γ_{Gw} and Γ_{Lw} values. All measurements were performed by the VNA Agilent PNA E8364A in a frequency band ranging from 6 GHz to 12 GHz resulting from the properties of the available tuners, and from the filter itself, as described in Section 4.1.2.

4.1.1 IL_{min} determination, in comparison with IEEE standard

In the first step, the two-port S-parameter measurements of the test filter in question were performed. The measured S-parameters were, subsequently, processed in an AWR Microwave Office (AWR MO) environment, see results in Figure 4.1(a) and Figure 4.1(b).

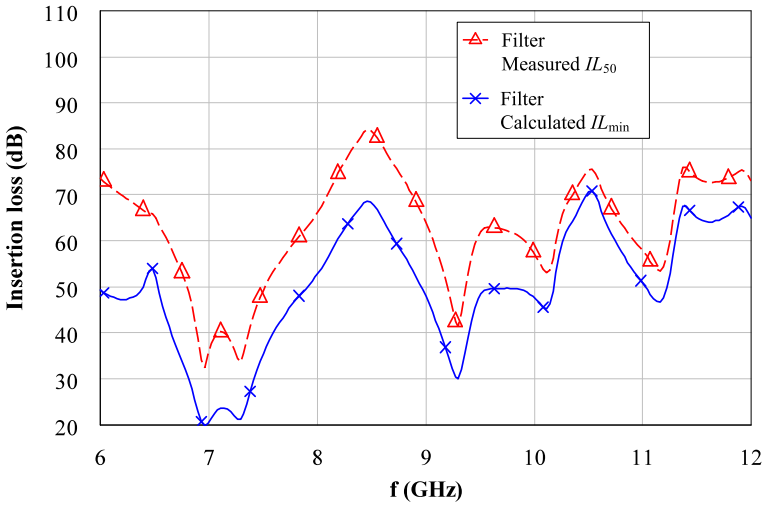

(a)

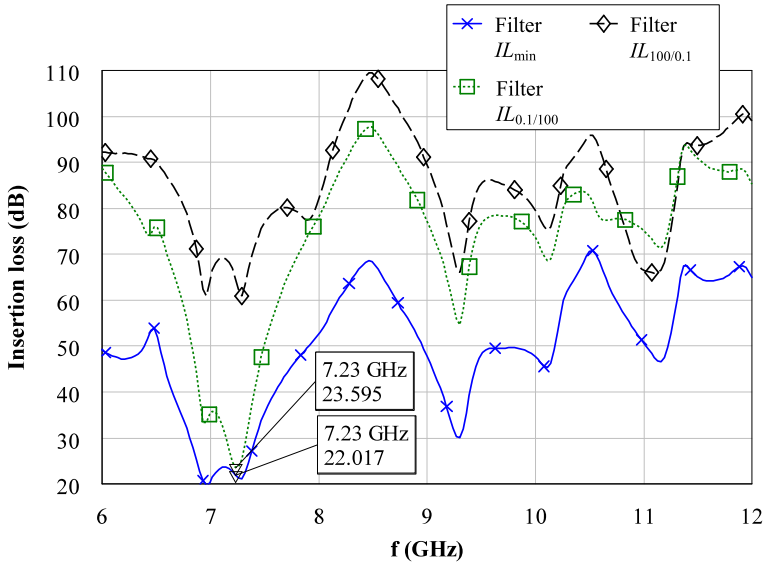

(b)

Figure 4.1: Obtained results in the AWR MO environment: a) Comparison of the Γ_{opt} *method (*IL_{min}*) with 50 Ω measurements (*IL_{50}*); b) Comparison of the* IL_{min} *with a virtual measurement ("mismatched-impedance test") performed according to the IEEE standard.*

The worst-case (minimum insertion loss) IL_{min} calculated values, according to 3.1.15, were compared to the mismatched-impedance test, as per [2], and extrapolated to this frequency band using AWR MO. The 0.1 Ω/100 Ω trace in Figure 4.1(b) corresponds to $Z_{\text{G}} = 0.1\ \Omega$ and $Z_{\text{L}} = 100\ \Omega$, while the 100 Ω/0.1 Ω trace corresponds to $Z_{\text{G}} = 100\ \Omega$ and $Z_{\text{L}} = 0.1\ \Omega$.

Figure 4.1(a) shows that the IL_{50} measurement corresponding to $Z_{\text{G}} = Z_{\text{L}} = 50\ \Omega$ says little about the properties of EMI/RFI filters operating in a general impedance environment. The measured-calculated IL_{min} values are 5–25 dB lower than the IL_{50} values derived directly from S-parameters. In addition, it can be clearly seen that a simple extrapolation of the mismatched-impedance test method (0.1 Ω/100 Ω) up to the microwave

frequency band is not applicable. It almost reveals the worst-case behavior, but only at a narrow band around the frequency of 7.23 GHz, see Figure 4.1(b). At other frequencies the difference from $IL_{\min}$ ranges from 10 to 40 dB. The opposite combination 100 Ω/0.1 Ω completely fails, the difference being 20–40 dB.

4.1.2 Γ_{opt} method validation

A series of measurements simulating worst-case operational states was performed in the frequency range of 6 GHz to 12 GHz to verify the proposed Γ_{opt} method. Two MT983A01 Maury Microwave Automated tuners realizing worst-case reflection coefficients Γ_{Gw} and Γ_{Lw} were connected to the input and the output of the test filter and the worst-case behavior was measured at six discrete frequency points, see Figure 4.2 and Figure 4.3.

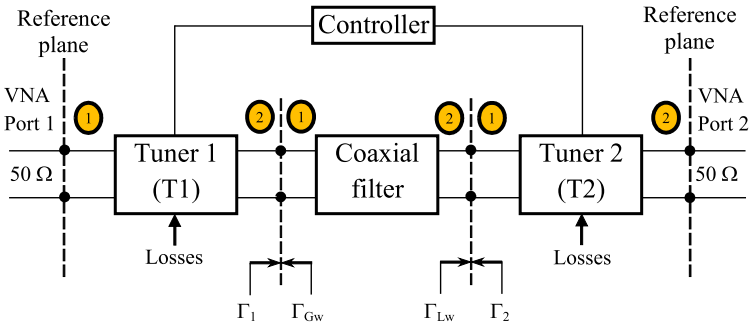

Figure 4.2: Block diagram of the measurement.

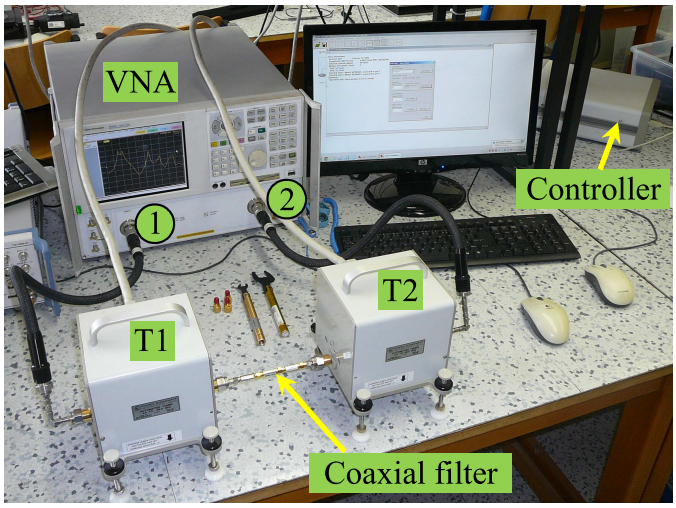

Figure 4.3: Experimental measurement setup.

The whole measurement procedure can be summarized in several steps:

First, reflection coefficients Γ_{Gw} and Γ_{Lw} were calculated from (3.1.5) and (3.1.6) using measured test filter S-parameters, as seen in Table 4.1. It should be emphasized that Γ_{Gw} and Γ_{Lw} values presented in this table were settable by the available impedance tuners.

Second, the tuners were measured one-by-one by a calibrated VNA and desired reflection coefficients were adjusted at their ports which were subsequently connected to the

filter, as shown in Figure 4.4. Since it is only possible to set the tuners to realize reflection coefficients Γ_{Gw} and Γ_{Lw} at a single frequency, the adjusting (measurement) procedure had to be repeated for all six frequency points. The corresponding S-parameters of the tuners were saved for subsequent corrections.

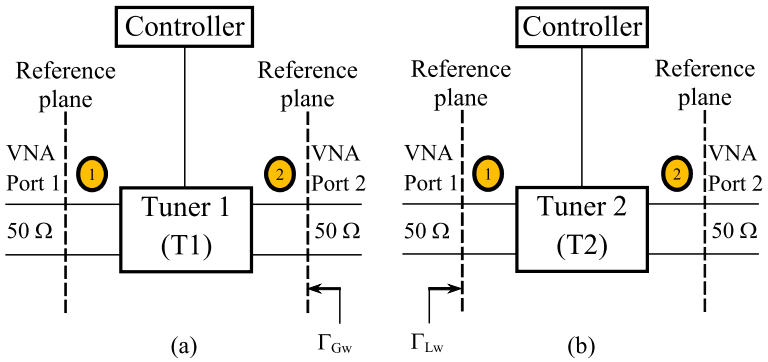

Figure 4.4: Tuner adjusted for worst-case reflection coefficients: a) Γ_{Gw} is realized by T_1 at port 2; b) Γ_{Lw} is realized by T_2 at port 1.

Third, a measurement of the whole tuner-filter-tuner cascade IL was performed at chosen frequency points. The tuners were set according to Table 4.1 and the corresponding IL_{M} values were measured, as can be seen in Figure 4.2 and Figure 4.3.

Table 4.1: Calculated worst-case reflection coefficients Γ_{Gw} and Γ_{Lw}

f (GHz)	$\lvert\Gamma_{\mathrm{Gw}}\rvert$ (−)	$\arg(\Gamma_{\mathrm{Gw}})$ (°)	$\lvert\Gamma_{\mathrm{Lw}}\rvert$ (−)	$\arg(\Gamma_{\mathrm{Lw}})$ (°)
7.02	0.95	165.2	0.87	-36.6
8.01	0.95	-125.0	0.69	-155.1
9.21	0.90	-34.4	0.89	8.5
9.81	0.88	20.0	0.85	69.0
10.41	0.68	123.7	0.68	127.9
11.61	0.86	44.5	0.69	-83.5

Fourth, the measured IL_{M} value of the whole cascade is influenced by tuner losses. These losses are a relatively strong function of Γ_{Gw} and Γ_{Lw} values and this is why an additional correction of the measurement, with respect to added insertion losses IL_{T1} and IL_{T2} caused by tuners T1 and T2, is necessary. To find the correct values of experimentally achieved minimum insertion loss IL_{minE}, previously saved S-parameters of the tuners were applied.

In order to calculate the added IL_{T1} and IL_{T2} caused by the tuners in the adjusted states, it is necessary to load the tuners with impedances corresponding to a real measurement, see Figure 4.2. It means that tuners must "see" the input or output reflection coefficients Γ_1 or Γ_2 realized by the test filter and the second tuner at one port and 50 Ω impedance at their second port, as seen in Figure 4.5. Since the $S_{12} = S_{21}$ parameters of the test filter are very low, input and output reflection coefficients Γ_1 and Γ_2 of the test

filter loaded by tuners are practically equal to S_{11} and S_{22} of the filter itself. To simulate the tuner-filter transitions, the ideal lossless LTUNER models in the AWR MO environment were used and their values set to Γ_1 and Γ_2 (filter S_{11} and S_{22}), see Figure 4.5. The calculated IL_{T1}, IL_{T2} and IL_{minE} values can be seen in Table 4.2.

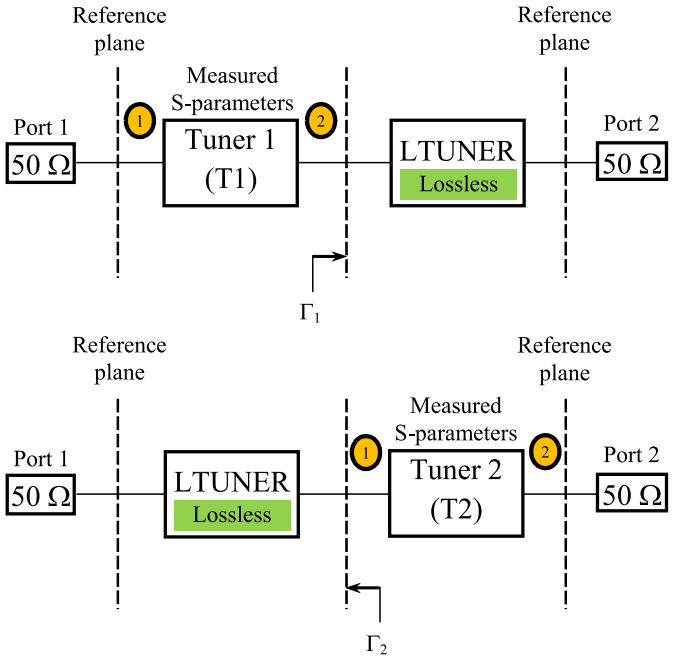

Figure 4.5: AWR MO models used to determine added attenuations IL_{T1} and IL_{T2} caused by tuners.

Table 4.2: Experimentally achieved results at six frequency points.

f (GHz)	IL_{M} (dB)	IL_{min} (dB)	IL_{T2} (dB)	IL_{T1} (dB)	IL_{T} (dB)	IL_{minE} (dB)	δ (dB)
7.02	32.24	21.54	2.72	4.61	7.33	24.91	3.37
8.01	59.10	53.11	1.33	4.64	5.97	53.13	0.02
9.21	41.77	34.60	3.16	2.30	5.46	36.31	1.71
9.81	57.81	49.63	4.89	1.48	6.37	51.44	1.81
10.41	68.97	66.80	1.33	0.80	2.13	66.84	0.04
11.61	70.61	64.07	2.38	3.32	5.69	64.92	0.85

Table 4.2 and Figure 4.6 summarize the values of all the important parameters measured or calculated during the experimental work. It directly includes the measured-calculated values IL_{M} of the whole cascade (without correction), the measured-calculated insertion loss IL_{T1} of T1, the measured-calculated insertion loss IL_{T2} of T2, the sum of both insertion losses $IL_{\mathrm{T}} = IL_{\mathrm{T1}} + IL_{\mathrm{T2}}$, and $IL_{\mathrm{minE}} = IL_{\mathrm{M}} - IL_{\mathrm{T}}$ values together with the IL_{min} values calculated from the measured filter S-parameters according to formula (3.1.15). The obtained $\delta = |IL_{\mathrm{minE}} - IL_{\mathrm{min}}|$ difference between the computed IL_{min} values and the experimentally achieved IL_{minE} values ranges from nearly zero to 3.37 dB. Taking

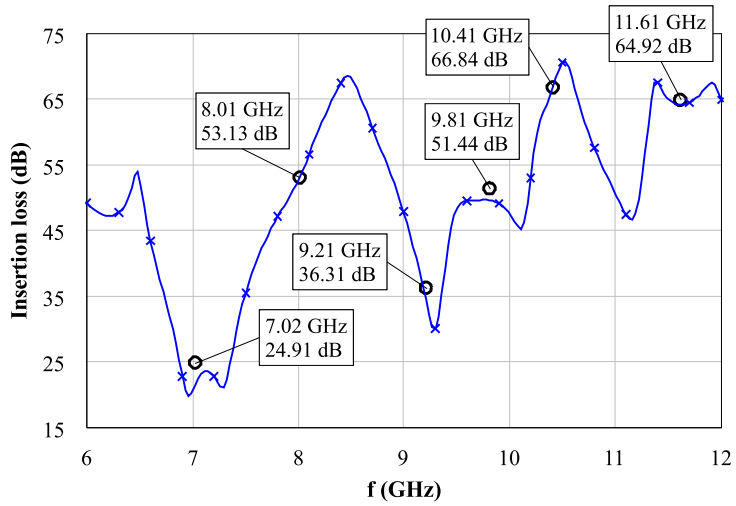

Figure 4.6: Experimentally achieved IL_{minE} values (depicted by "○") compared with calculated IL_{min} values (depicted by "×").

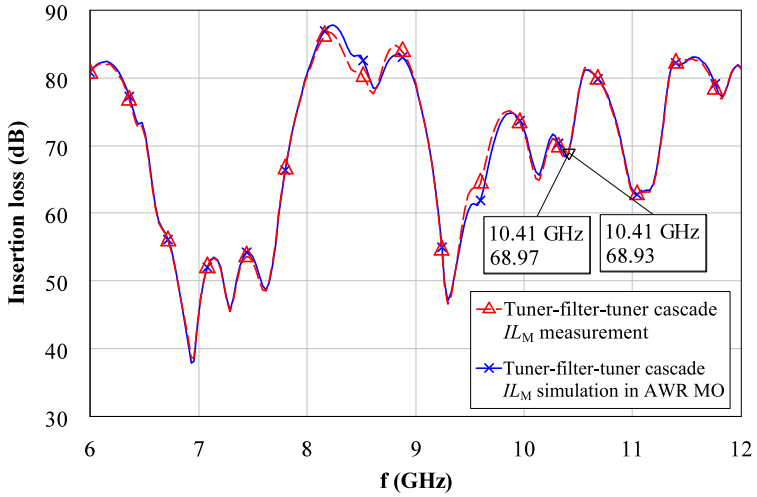

Figure 4.7: Comparison of the measured IL_{M} values of the tuner-filter-tuner cascade with a simulation of the whole cascade performed in an AWR MO environment using independently measured S-parameters of individual blocks (T1, test filter, T2) for particular adjusted states of tuners at the frequency 10.41 GHz.

into account that IL_{minE} and IL_{min} values range from 21 to almost 67 dB the differences are small enough to be acceptable.

Finally, the precision and accuracy of the performed measurements were verified by comparing the measured-calculated IL_{M} of the whole cascade for specific adjusted state of tuners at 10.41 GHz, with the corresponding IL_{M} simulation of the cascade performed from independently measured S-parameters of individual blocks: T1 and T2 for specifically adjusted states at 10.41 GHz and the test filter, as can be seen in Figure 4.7. Despite possible temperature drifts (all measurements were rather time-consuming), VNA measurement uncertainty, the mounting repeatability of both connectors and tuner settings, it can be seen that both traces are in good agreement.

4.1.3 Professional EMI/RFI filter characterization

This section describes evaluation procedure of a professional SKY1FL16DMA2 (SKYBERGTECH) single-phase three-wire (European standard) interference filter using the approach developed in Section 3.1.2. The filter in question, see Figure 4.8, is analyzed in terms of the worst-case scenario (minimum insertion loss in its stop band).

This filter is designated for the interconnection of power-line cables and power electronic devices (up to 16 A) or screened chambers. Its simplified inner structure has been already described in Section 3.1.2 and depicted in Figure 3.2. An opened filter terminal box with a standard three power-line conductor connection can be seen in Figure 4.9.

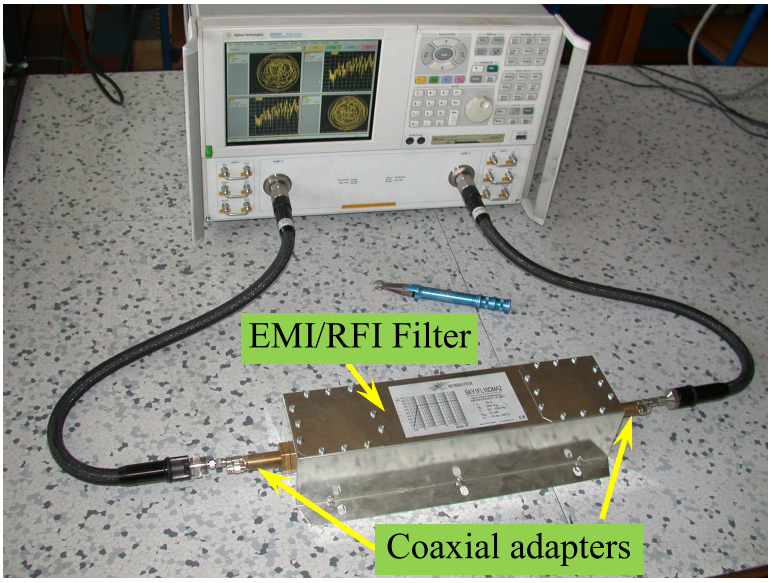

Figure 4.8: SKY1FL16DMA2 single-phase EMI/RFI filter connected through SMA adapters to the VNA.

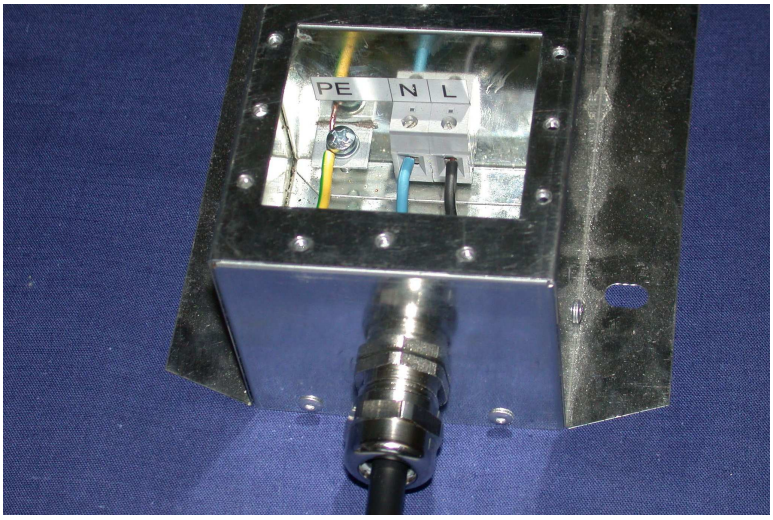

Figure 4.9: Opened box with PE, L and N terminals and connected power-line cable wires.

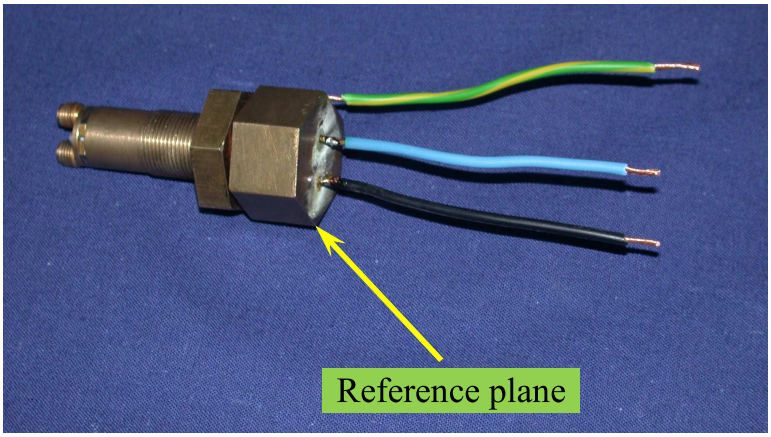

Figure 4.10: Coaxial 50-Ω SMA adapter.

For the filter S-parameters measurement two 50-Ω SMA adapters, enabling the connection of filter terminals to the VNA and manufactured according to [8], were used, as seen in Figure 4.10. Both adapters contain in their body a pair of 50-Ω coaxial lines equipped with SMA connectors on one side. On the other side, the inner conductors of the coaxial lines are extended by short sections of power-line wires enabling their connection to the filter terminals. The insertion loss of each adapter is below 0.4 dB at 10 GHz. Reference measurement planes can be set at the end of adapter coaxial lines, see Figure 4.10. The adapters were fixed to the filter box replacing the power cables bushings in Figure 4.9, see Figure 4.8. The interconnecting wires were shaped in the same way as conductors of the power-line cable when connected to the filter terminals, see Figure 4.9. The filter four-port S-parameters were measured by the two-port VNA in a frequency range from 1 GHz to 10 GHz. Six individual two-port S-parameter measurements were performed. Adaptor ports unconnected to the VNA were always terminated by 50-Ω SMA loads. From these measurements, the standard four-port S-parameter matrix with 50-Ω reference impedance at all ports was compiled.

Subsequently, this S-parameter matrix was used to determine the required CM and DM parameters of the concerned filter.

First, the filter analysis was performed using the AWR MO simulator, as described in Section 3.1.2, by using one of its common power-divider models and a constant phase-shift model. For the determination of IL, IL_{min} of the concerned filter in terms of CM (IL_{CC} ,IL_{minCC}) and DM (IL_{DD} , IL_{minDD}) and their mutual CM→DM (IL_{DC}, IL_{minDC}) or DM→CM (IL_{CD}, IL_{minCD}) conversions, the four-port S-matrix was connected between two ideal 50-Ω in-phase or out-of-phase power dividers $\mathrm{PD_a}$ and $\mathrm{PD_b}$, as seen in Figure 3.3. Detail description of this S-parameter evaluation approach is stated in Section 3.1.2.

Insertion loss IL_{CC} values of the filter for the CM were determined using two ideal in-phase power dividers (SPLIT2) described by the S-matrix $\mathrm{S^{IP}}$ (3.1.17), see Figure 4.11. Insertion loss IL_{DD} values of the filter for the DM were simulated by means of two ideal out-of-phase power dividers (SPLIT2 + PHASE2) described by the S-matrix $\mathrm{S^{OP}}$ (3.1.18), see Figure 4.12.

Fig 4.11(a) and Figure 4.12(a) show the determined IL_{minCC} and IL_{minDD} frequency dependences of the SKY1FL16DMA2 filter in the frequency band from 1 to 10 GHz. Since the plots are strongly frequency dependent, Figure 4.11(b) and Figure 4.12(b) also include

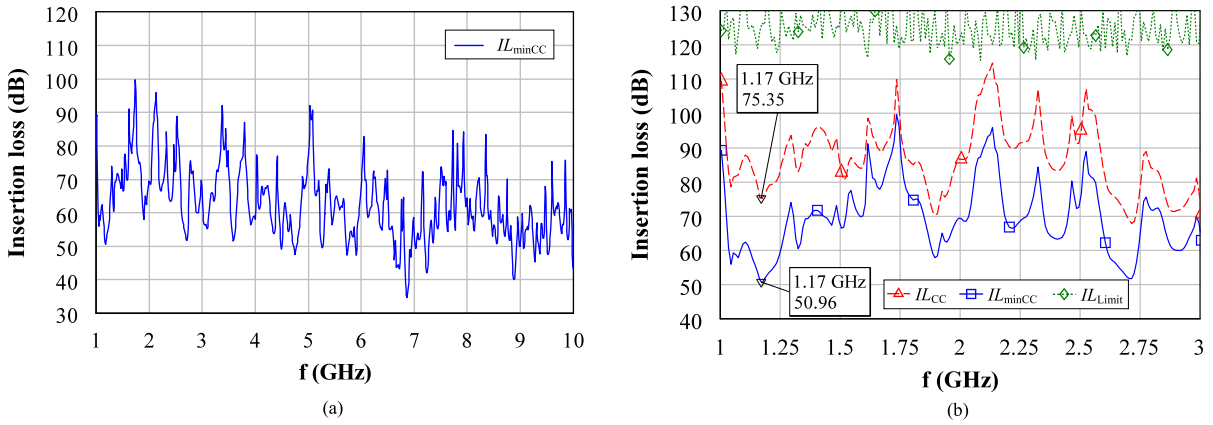

Figure 4.11: SKY1FL16DMA2 parameters: a) Minimum IL_{minCC} insertion loss values for CM at both mixed-mode ports; b) Characterization in a narrow frequency band including IL_{minCC}, IL_{CC} and IL_{Limit} frequency dependences.

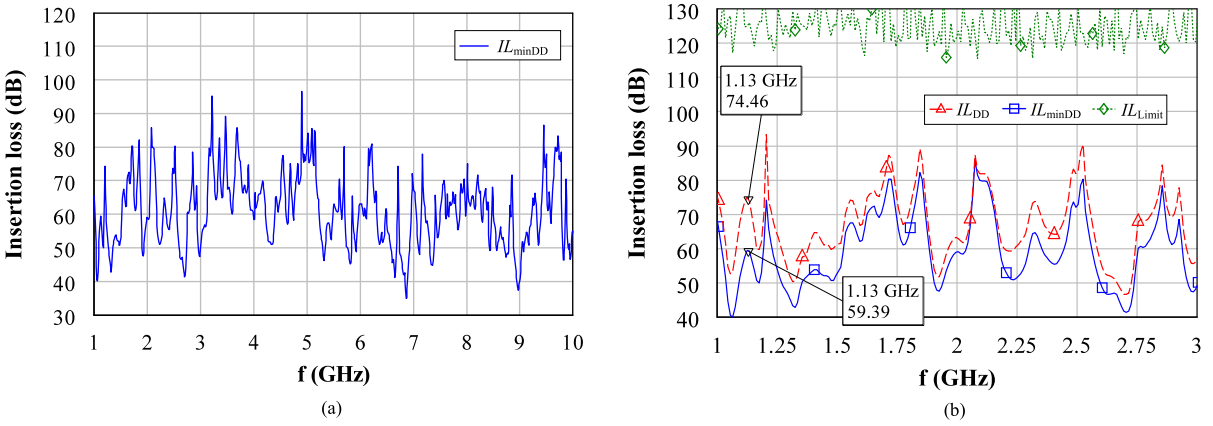

Figure 4.12: SKY1FL16DMA2 parameters: a) Minimum IL_{minDD} insertion loss values for DM at both mixed-mode ports; b) Characterization in a narrow frequency band including IL_{minDD}, IL_{DD} and IL_{Limit} frequency dependences.

the zoomed 1–3-GHz frequency range where differences between IL_{CC} and IL_{minCC}, and between IL_{DD} and IL_{minDD}, can be easily distinguished. To prove that the VNA dynamic range was satisfactory the figures also include the measured VNA noise floor traces IL_{Limit} expressed in the form of maximum measurable *IL*.

Insertion loss IL_{DC} values of the filter for the CM→DM conversion were calculated using a combination of the in-phase power divider (SPLIT2) at the input and out-of-phase power divider (SPLIT2+PHASE2) at the output of the filter, see Figure 3.4 and Figure 4.13. Insertion loss IL_{CD} values of the filter for the DM→CM conversion were calculated using a combination of the out-of-phase power divider (SPLIT2 + PHASE2) at the input and the in-phase power divider (SPLIT2) at the output of the filter, see Figure 4.14.

The presented graphs show that the developed method is applicable for determining all noteworthy parameters of practical EMI/RFI filters up to high microwave frequencies. The graphs also indicate that, as concerns all CM→CM, DM→DM, CM→DM and DM→CM

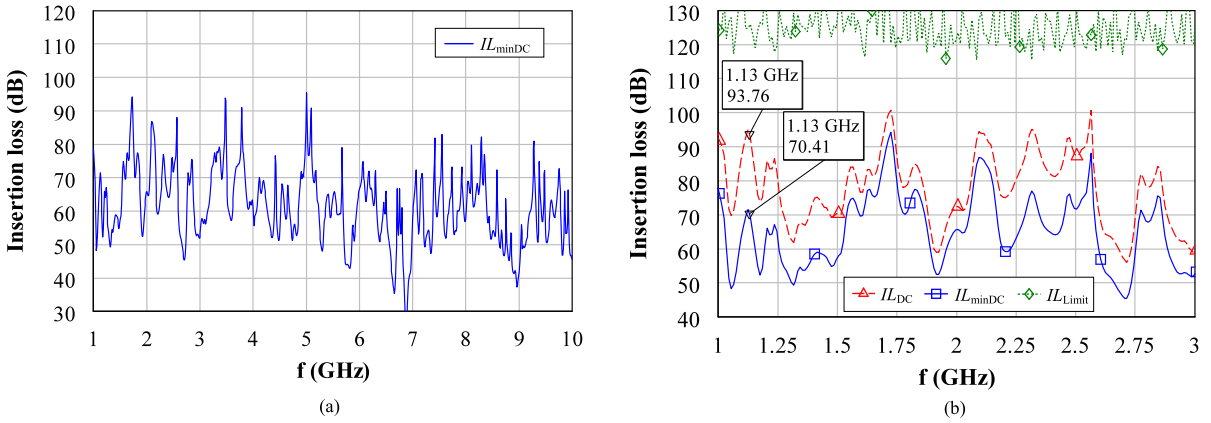

Figure 4.13: SKY1FL16DMA2 filter parameters: a) Minimum IL_{minDC} insertion loss values for CM to DM conversion; b) Characterization in a narrow frequency band including IL_{minDC}, IL_{DC} and IL_{Limit} frequency dependences.

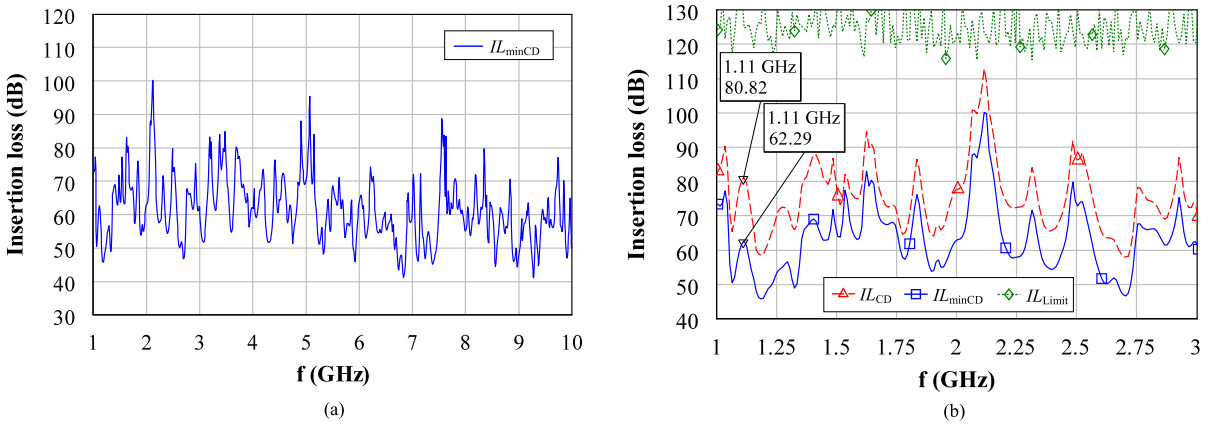

Figure 4.14: SKY1FL16DMA2 filter parameters: a) Minimum IL_{minCD} insertion loss values for DM to CM conversion; b) Characterization in a narrow frequency band including IL_{minCD}, IL_{CD} and IL_{Limit} frequency dependences.

modes, the minimum IL_{minCC} and IL_{minDD} as well as IL_{minDC} and IL_{minCD} insertion loss values can substantially differ from the IL_{CC}, IL_{DD}, IL_{DC} and IL_{CD} values. In the given case, this difference attains, for example, 24 dB at 1.17 GHz in the case of IL_{CC}, 15 dB at 1.13 GHz in case of IL_{DD}, 23 dB at 1.13 GHz in case of IL_{DC}, and 18 dB at 1.11 GHz in case of IL_{CD}.

All obtained results show that the minimum insertion loss values can be even more than 20 dB lower in comparison to insertion loss values corresponding to standard mixed-mode reference impedances. However, this method does not enable to determine the real worst-case minimum insertion loss values of a concerned EMI/RFI filter since it neglects reflections of converted modes at the filter input and output ports, as explained in detail in Section 3.1.2.

4.1.4 Professional EMI/RFI filter characterization - advanced method

This section describes evaluation of the professional SKY1FL16DMA2 (SKYBERGTECH) single-phase three-wire (European standard) interference filter using advanced method developed in Section 3.1.3.

The filter is characterized by its measured four-port SM S-parameters and by using (3.1.23), (3.1.25) and (3.1.47)–(3.1.53), these four-port SM S-parameters were converted to four degenerated two-port SM matrices $\boldsymbol{S}^{\mathrm{D}43}$ for CM→CM, $\boldsymbol{S}^{\mathrm{D}21}$ for DM→DM, $\boldsymbol{S}^{\mathrm{D}41}$ for DM→CM, and $\boldsymbol{S}^{\mathrm{D}23}$ for CM→DM. To enable calculations of individual IL^{43}_{min}, IL^{21}_{min}, IL^{41}_{min}, and IL^{23}_{min} values using one common equation (3.1.15), two-port matrices $\boldsymbol{S}^{ji}$ with reduced indices were created, see (4.1.1). Input port 1 of a two-port, described by $\boldsymbol{S}^{ji}$ matrix, corresponds to index i, while its output port 2 corresponds to index j. Table 3.1 shows the relations among all measurement types, with IL^{ji}_{min} to be calculated, and how they correspond to degenerated two-port matrices $\boldsymbol{S}^{\mathrm{D}ji}$, and two-port matrices with reduced indices $\boldsymbol{S}^{ji}$.

$$\boldsymbol{S}^{\mathrm{D}ji} = \begin{pmatrix} S^{\mathrm{D}ji}_{ii} & S^{\mathrm{D}ji}_{ij} \\ S^{\mathrm{D}ji}_{ji} & S^{\mathrm{D}ji}_{jj} \end{pmatrix} = \boldsymbol{S}^{ji} = \begin{pmatrix} S^{ji}_{11} & S^{ji}_{12} \\ S^{ji}_{21} & S^{ji}_{22} \end{pmatrix} \tag{4.1.1}$$

The formula (3.1.15) is simple, yet practical IL^{ji}_{min} calculations became unexpectedly complicated. A detailed analysis showed that when evaluating denominator $k - \sqrt{k^2 - 1}$, calculations are influenced by the number of available decimal points. Since k of the EMI/RFI filters can attain extremely high values (tens of thousands), the value of the denominator approaches zero which leads to unreliable results.

If necessary, this problem can be solved using a different approach as IL^{ji}_{min} is inversely proportional to the maximum available gain G_{tmax} (4.1.2), see [25] or [26].

$$G^{ji}_{\mathrm{tmax}} = \frac{(1-|\Gamma_{\mathrm{Lw}}|^2)\left|S^{ji}_{21}\right|^2(1-|\Gamma_{\mathrm{Gw}}|^2)}{\left|\left(1-S^{ji}_{11}\Gamma_{\mathrm{Gw}}\right)\left(1-S^{ji}_{22}\Gamma_{\mathrm{Lw}}\right)-S^{ji}_{12}S^{ji}_{21}\Gamma_{\mathrm{Gw}}\Gamma_{\mathrm{Lw}}\right|^2} \tag{4.1.2}$$

In Section 3.1.1, Γ_{Gw} and Γ_{Lw} were defined as the worst-case reflection coefficients and can be computed from elements of $\boldsymbol{S}^{ji}$ using (3.1.5)–(3.1.11). Finally, IL^{ji}_{min} can be computed using (3.1.15):

$$IL^{ji}_{\mathrm{min}} = \frac{1}{G^{ji}_{\mathrm{tmax}}}. \tag{4.1.3}$$

For a complete evaluation of the SKY1FL16DMA2 filter, the IL^{ji}_{min} calculation process was repeated for all two-port S-matrices $\boldsymbol{S}^{43}$, $\boldsymbol{S}^{21}$, $\boldsymbol{S}^{23}$, and $\boldsymbol{S}^{41}$; this was necessitated by the numerous combinations of reflection coefficients Γ_s and Γ_t corresponding to terminating impedances Z_s and Z_t of unused ports in Figure 3.6. To find the worst-case IL^{ji}_{minW} values, amplitudes of the reflection coefficients $|\Gamma_s|$ and $|\Gamma_t|$ were set to unity and only the phases of the reflection coefficients $\arg(\Gamma_s)$ and $\arg(\Gamma_t)$ were changed using an optimization process in the ⟨-180° 180°) interval. This corresponds to a maximum reflection of the converted modes back into the filter structure and finding the optimum phasing which leads to the highest impact on the concerned transmission.

The following graphs depict the IL^{ji}_{minW} values achieved for all CM/DM combinations, see Figures 4.15–4.18(a).

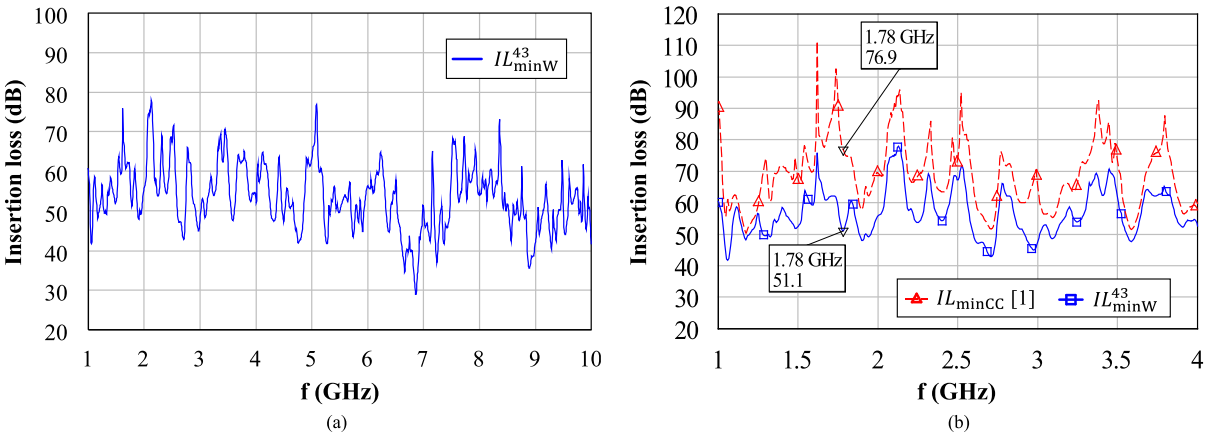

Figure 4.15: CM→CM analysis of the SKY1FL16DMA2 filter: a) Computed worst-case IL^{43}_{minW} insertion loss values; b) Characterization in a narrower frequency band including IL_{minCC} values achieved in Section 4.1.3.

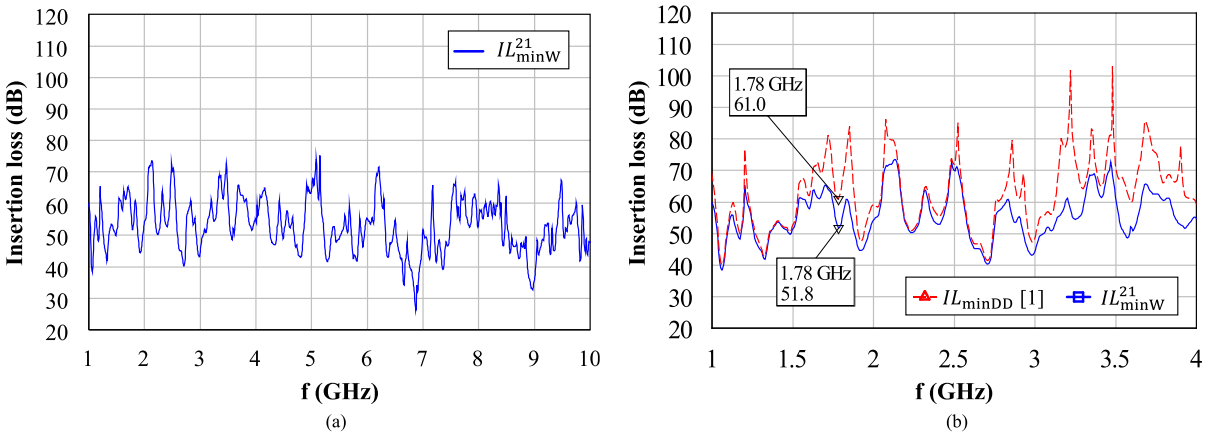

Figure 4.16: DM→DM analysis of the SKY1FL16DMA2 filter: a) Computed worst-case IL^{21}_{minW} insertion loss values; b) Characterization in a narrower frequency band including IL_{minDD} values achieved in Section 4.1.3.

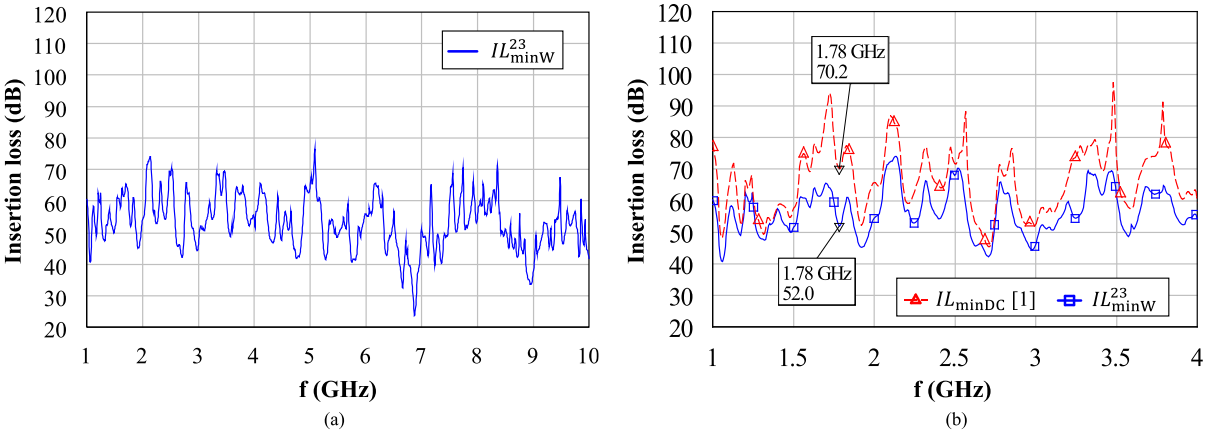

Figure 4.17: CM→DM analysis of the SKY1FL16DMA2 filter: a) Computed worst-case IL^{23}_{minW} insertion loss values; b) Characterization in a narrower frequency band including IL_{minDC} values achieved in Section 4.1.3.

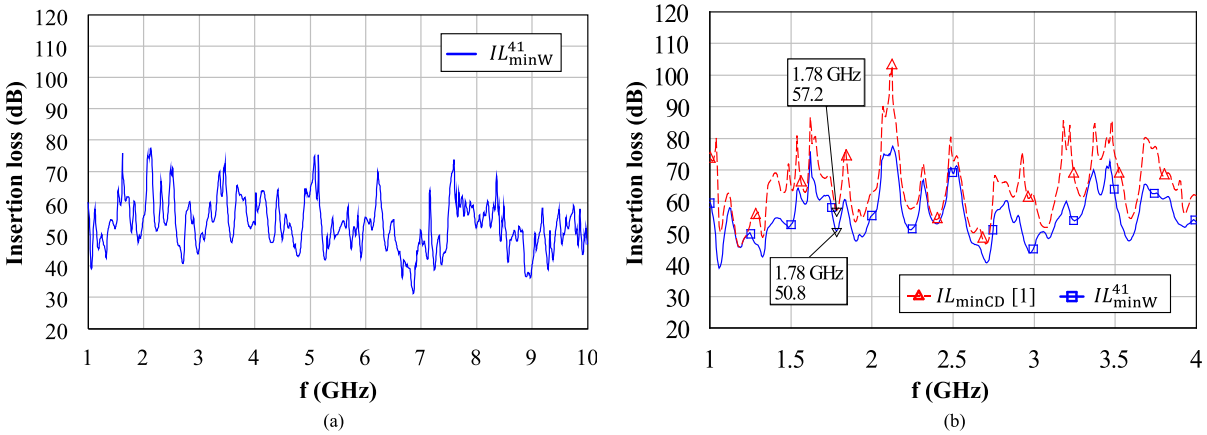

Figure 4.18: DM→CM analysis of the SKY1FL16DMA2 filter: a) Computed worst-case IL^{41}_{minW} insertion loss values; b) Characterization in a narrower frequency band including IL_{minCD} values achieved in Section 4.1.3.

Figures 4.15–4.18(b) show the differences between IL^{ji}_{minW} and IL_{min} values, calculated according to the technique described in Section 3.1.2, in the zoomed frequency band of 1 GHz to 4 GHz.

It can be clearly seen that the IL^{ji}_{minW} values corresponding to $|\Gamma_s| = 1$ and $|\Gamma_t| = 1$ can be more than 20 dB lower than IL_{min} values corresponding to $|\Gamma_s| = 0$ and $|\Gamma_t| = 0$. This confirms a significant potential influence of the reflected converted modes on the EMI/RFI filter parameters.

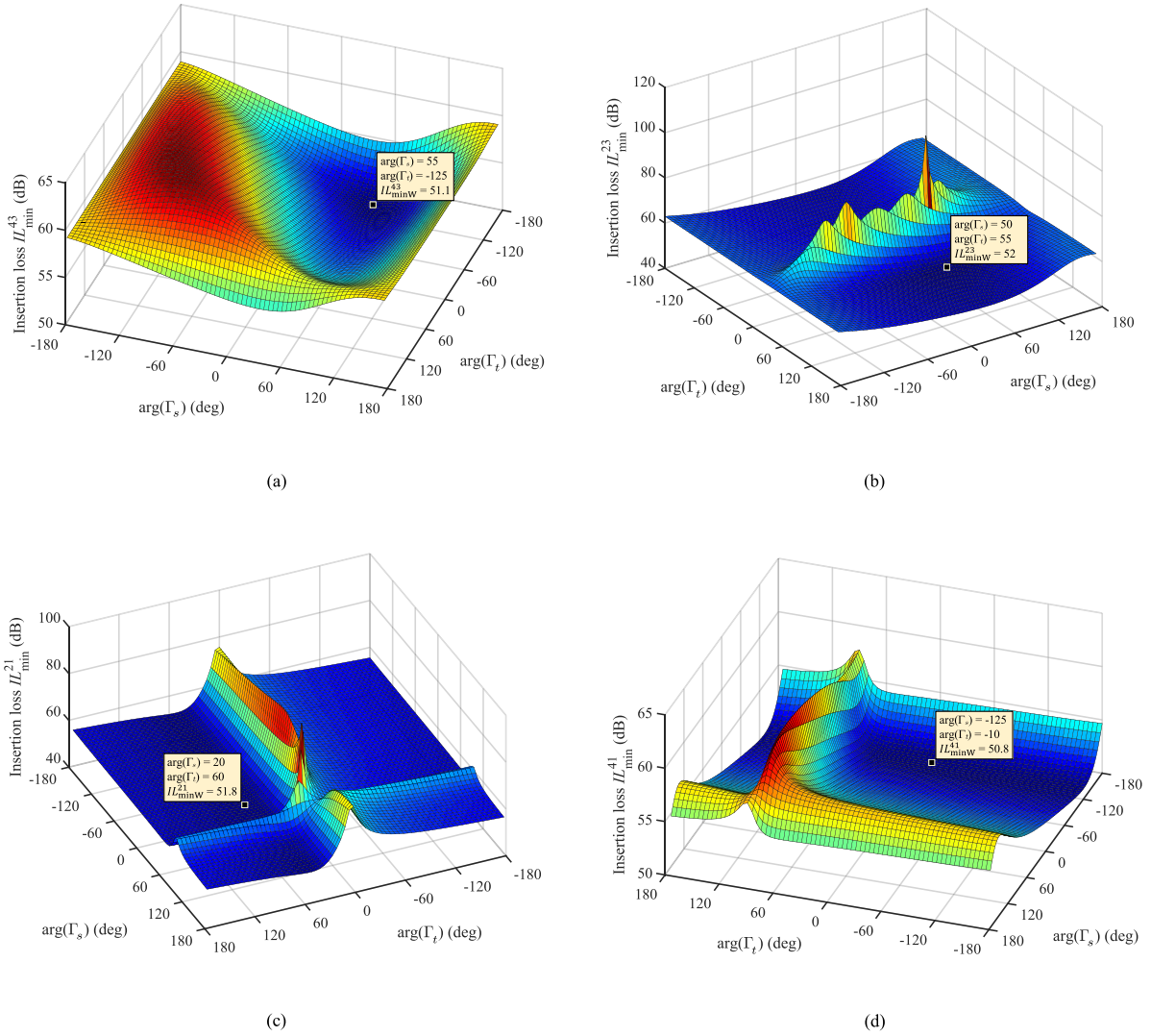

Figure 4.19: IL^{ji}_{min} values for all CM/DM combinations at single frequency point of 1.78 GHz for different phase combinations of reflection coefficients Γ_s and Γ_t: a) IL^{43}_{min} values for a CM→CM transmission; b) IL^{23}_{min} values for a CM→DM conversion; c) IL^{21}_{min} values for a DM→DM transmission; d) IL^{41}_{min} values for a DM→CM transmission.

From a practical point of view, it is important to estimate how probable an occurrence of this effect is. Figure 4.19 shows examples of the IL^{ji}_{min} dependencies on a combination of phases of reflection coefficients $|\Gamma_s| = 1$ and $|\Gamma_t| = 1$ for CM and DM and their conversions at the chosen frequency point of 1.78 GHz. The probability that IL^{43}_{min} values for CM→CM will be more than 20 dB lower than $IL_{\mathrm{minCC}} = 76.9$ dB is 47 %. In addition,

the IL^{43}_{min} values are more than 10 dB lower than the IL_{minCC} value in all tested cases. The probability that IL^{23}_{min} values for CM→DM will be 10 dB lower than $IL_{\mathrm{minDC}} = 70.2$ dB is 61 %. On the other hand, the differences between IL^{21}_{minW} and IL_{minDD} for DM→DM and IL^{41}_{minW} and IL_{minCD} for DM→CM are smaller than 10 dB but still significant. The above described values show that reflections of the converted modes must be taken into account.

To demonstrate the advantages of the advanced method over the approach developed in Section 3.1.2, a AWR MO circuit model, corresponding to a possible measurement setup, was created and related virtual measurements were performed. The AWR MO model is illustrated in Figure 4.20. This circuit also allows comparison of the results of the new method with results corresponding to a "nominal impedance method", which relates to condition that all modes "see" their nominal impedances at the corresponding ports. In Figure 3.5, SM "sees" 50 Ω at Ports **1**–**4**, while CM "sees" 25 Ω and DM "sees" 100 Ω at the mixed-mode ports p_{43a} and p_{43b}. The "nominal impedance method" can be understood as a better defined arrangement of the asymmetrical and symmetrical test circuits suggested in the European standard [1, Ch. 5.2.3 and Ch. 5.2.4] and in the IEEE standard [2, Ch. 10.8].

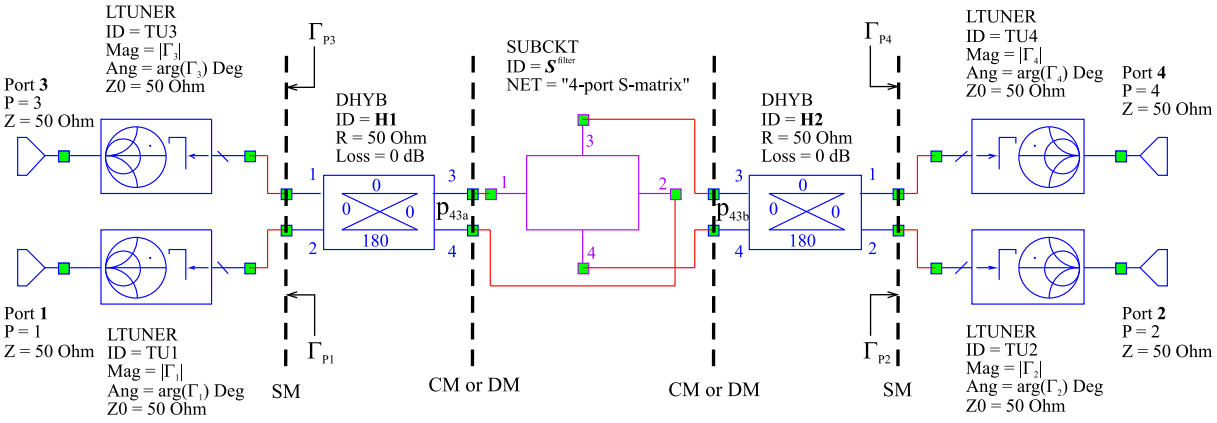

Figure 4.20: Virtual measurement in AWR MO.

The proposed model is based on the structure defined in Figure 3.5, in addition to S-parameters of the measured filter and two ideal 180° hybrids, four LTUNER ideal impedance tuners are connected between hybrid ports and outer circuit ports. Each LTUNER transforms 50 Ω impedance at outer Ports **1**–**4** to a reflection coefficient with arbitrarily adjustable amplitude and phase. These reflection coefficients are defined with respect to $Z_0 = 50\ \Omega$ and are marked Γ_{P1} to Γ_{P4}. The particular values of Γ_{P} can be found in Tables 4.3–4.5. As an example, the CM→CM transmission was considered and the related insertion loss values were calculated at three different frequencies for all methods mentioned above.

Table 4.3 corresponds to the CM→CM measurement and the "nominal impedance method". This means 25-Ω loading of CM and 100-Ω loading of DM at both filter's mixed mode ports. At SM Ports **1**–**4**, this corresponds to $\Gamma_{\mathrm{P1}} = \Gamma_{\mathrm{P2}} = \Gamma_{\mathrm{P3}} = \Gamma_{\mathrm{P4}} = 0$. These settings cause high reflections of CM at both filter's mixed-mode ports and full absorption of the energy converted into DM in outer terminations formed by Port **1** and Port **2**. Therefore the "nominal impedance method", compared to the technique developed

Table 4.3: Insertion losses IL^{43}_{NIM} determined by the "nominal impedance method"

	Frequency (GHz)		
Reflection coefficient	1.4	1.78	3.19
Γ_{P1}	0	0	0
Γ_{P2}	0	0	0
Γ_{P3}	0	0	0
Γ_{P4}	0	0	0
$IL^{43}_{\mathrm{NIM}} = IL_{\mathrm{CC}}$ (dB)	95.7	85.7	74.7

Table 4.4: Insertion losses IL^{43}_{min} determined according to the technique used in 4.1.3

	Frequency (GHz)		
Reflection coefficient	1.4	1.78	3.19
Γ_{P1}	0	0	0
Γ_{P2}	0	0	0
Γ_{P3}	$0.97e^{\mathrm{j}(-13^\circ)}$	$0.85e^{\mathrm{j}(85^\circ)}$	$0.66e^{\mathrm{j}(128^\circ)}$
Γ_{P4}	$0.96e^{\mathrm{j}(-3^\circ)}$	$0.73e^{\mathrm{j}(31^\circ)}$	$0.87e^{\mathrm{j}(95^\circ)}$
$IL^{43}_{\mathrm{min}} = IL_{\mathrm{minCC}}$ (dB)	71.9	76.9	66.1

Table 4.5: Insertion losses IL^{43}_{minW} determined by the new method

	Frequency (GHz)		
Reflection coefficient	1.4	1.78	3.19
Γ_{P1}	$1e^{\mathrm{j}(39^\circ)}$	$1e^{\mathrm{j}(55^\circ)}$	$1e^{\mathrm{j}(2^\circ)}$
Γ_{P2}	$1e^{\mathrm{j}(1^\circ)}$	$1e^{\mathrm{j}(-125^\circ)}$	$1e^{\mathrm{j}(19^\circ)}$
Γ_{P3}	$0.97e^{\mathrm{j}(-13^\circ)}$	$0.46e^{\mathrm{j}(9^\circ)}$	$0.88e^{\mathrm{j}(100^\circ)}$
Γ_{P4}	$0.84e^{\mathrm{j}(-3^\circ)}$	$0.76e^{\mathrm{j}(48^\circ)}$	$0.39e^{\mathrm{j}(149^\circ)}$
IL^{43}_{minW} (dB)	58.5	51.1	57.7

in Section 3.1.2 [23] and the advanced method developed in Section 4.1.4, provides the highest insertion loss values IL_{NIM}.

The reflection coefficients defined in Table 4.4 correspond to the CM→CM measurement and the technique described in Sections 3.1.2. The values for Γ_{P3} and Γ_{P4}, found by the "Γ_{opt} method", ensure perfect impedance matching for CM at both filter's mixed mode ports. Setting $\Gamma_{P1} = \Gamma_{P2} = 0$ provides full absorption of DM converted modes. Impedance matching of CM removes reflections and provides more energy into and out from the filter. The result is that the related IL^{43}_{min} values are lower than the IL_{NIM} values.

Table 4.5 summarizes the results of the virtual measurements performed according to the advanced method. Γ_{P3} and Γ_{P4} reflection coefficients are determined by the "Γ_{opt} method" using (3.1.5)-(3.1.6) and ensure impedance matching for CM at both filter's mixed mode ports. Setting $|\Gamma_{P1}| = |\Gamma_{P2}| = 1$ results in 100 % return of energy converted into DM back into the filter. Arg(Γ_{P1}) and arg(Γ_{P2}) are determined by the above mentioned optimization procedure and ensure optimum phasing for the maximum conversion of back reflected energy into CM in the filter structure. All these conditions are fulfilled simultaneously and form a boundary with the lowest possible IL^{43}_{minW} values.

Figure 4.21 illustrates the performed virtual measurements and includes both the *IL* values from Tables 4.3–4.5 and the frequency dependencies corresponding to all three measurement methods. Measurements based on the "nominal impedance method" are overly optimistic and relate little to the filter's behavior in a real impedance environment. On the other hand, the IL^{43}_{minW} values, calculated according to the proposed new method, correspond to the worst-case scenario, and *IL* values of real three-wire EMI/RFI filters will always be above this limit.

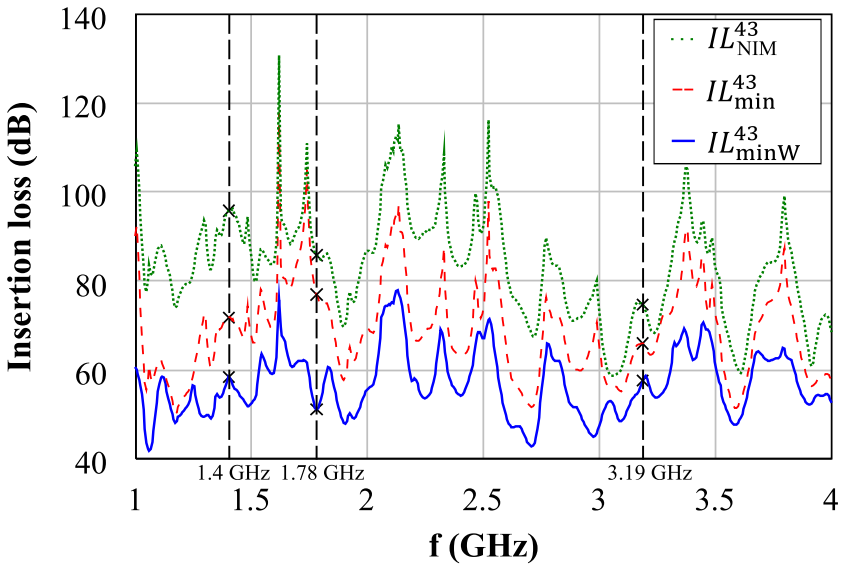

Figure 4.21: CM→CM insertion loss of the SKY1FL16DMA2 filter: Comparison of IL^{43}_{NIM} corresponding to IL_{CC} in Section 4.1.3, IL^{43}_{min} corresponding to IL_{minCC} in Section 4.1.3, IL^{43}_{minW} plots, and AWR MO virtual measurements depicted by "×".

Unlike previously published methods, the advanced method takes into account reflections of the converted CM→DM or DM→CM modes back into the filter structure. When considering 100 % reflections of the converted modes, worst-case minimum insertion losses IL^{ji}_{minW} more than 20 dB lower than the corresponding values presented in Section 4.1.3, were achieved. This work also shows that the occurrence of this phenomenon is high and thus considering this effect is important in practice. The method can be used to measure any filter at any frequency and raises the possibility of improving current measurement standards.

4.2 Extreme impedances - virtual measurement

The main goal of this section is to verify analytically derived formulas in Section 3.2.2 for uncertainties suppression using virtual measurements and numerical calculations. It is focused on the analysis of the error model (2.2.3), developed in [41], by means of the Monte Carlo Simulations (MCS). Specifically, it analyzes the influence of the calibration/correction process, non-ideal microwave components and basic sources of uncertainty on resulting Γ_x measurement uncertainty. MCS can be simply implemented and it enables possible non-linear behavior of the error model (2.2.3) to be revealed in contrast to the law of uncertainty propagation.

In contrast to the simplified transmission coefficient $T_{21}^{'}$ that was analyzed in Section 3.2.2, the error model (2.2.3) describes the behavior of a real measurement setup and enables a calibration/correction process to be included in the analysis. Consequently, the error model analysis should be more realistic in the estimation of the resulting Γ_x measurement uncertainty expressed by covariance matrix $\mathbf{V}(\Gamma_x)$. Error model (2.2.3) describes the relationship between general transmission coefficient T_{21}^{G} and Γ_x. Nevertheless, it cannot be used for the generation of measured data T_{21} without the knowledge of calibration constants C_1, C_2, and C_3. Therefore, the derived general transmission coefficient T_{21}^{G}, (3.2.2), was used to generate simulated measured data T_{21} for MCS analysis. The main goal of this analysis is to extend results achieved in Section 3.2.2 and show the dependence of two basic suppression limits SL^{HW} and SL^{IB} on the choice of calibration and reference standards and the real interferometric box (**IB**) and amplification box (**AB**) hardware. To achieve this goal, only phase noise N_H in the VNA test channel and the noise source caused by the receiver in the VNA test channel N_L^T are taken into account since they are both influenced in (3.2.21) by SL^{IB} and SL^{HW}, respectively, see the resulting T_{21} derived from (3.2.2):

$$T_{21} = \frac{1}{a_{1R}} \left(S_{21}^{IB'} S_{21}^{AB'} N_H a_1 + N_L^T \right). \tag{4.2.1}$$

Additive noise sources $N_L, N_L^{\mathbf{IB}}$, and $N_L^{\mathbf{AB}}$ in (3.2.2) are neglected since their implementation in the analysis would not bring any added value. For MCS purposes (4.2.1) is rewritten into

$$T_{21} = S_{21}^{IB'} S_{21}^{AB'} n + \varepsilon. \tag{4.2.2}$$

The variable n is an estimate of N_H only and neglects the influence of the term a_1/a_{1R}. The result of a_1/a_{1R} is in an ideal case the same for all measurements and, therefore, included in the calibration constants. Nevertheless, for a real VNA the noise sources in the reference channel described by $\mathbf{V}(a_{1R})$ will cause additional T_{21} measurement uncertainty. To simplify the analysis the influence of $\mathbf{V}(a_{1R})$ was included only into the second term of (4.2.2). The variable ε is an estimate of N_L^T/a_{1R} that creates uncertainty u_{VNA} given by the VNA reference channel and the VNA receiver in the test channel.

For the analysis, an area of extremely high impedances in the impedance range from 5 kΩ to 100 kΩ was chosen due to the simplicity of the illustration, see possible locations of DUTs against calibration standards S_i and reference standard Z_{ref} in the zoomed Smith chart in Figure 4.22.

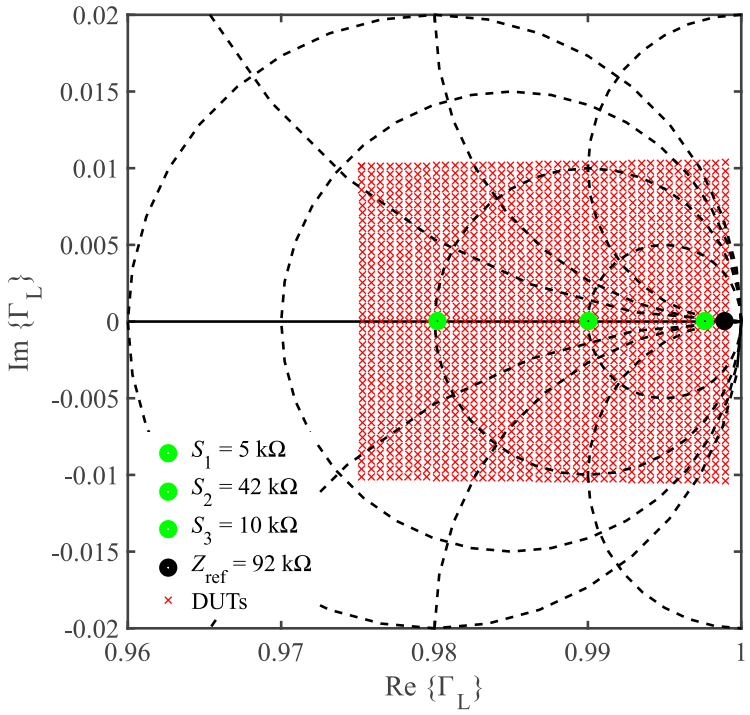

Figure 4.22: Zoomed smith chart - an example of the location of calibration standards S_i, reference standard Z_{ref}, and DUTs in the area of extremely high impedances.

To simulate an **IB** a 180° hybrid and a reference impedance $Z_{\text{x}} \approx Z_{\text{ref}}$, [22], that can produce a small signal Δ in a wide frequency band, were chosen, see Figure 2.2. All these assumptions do not have an impact on the generality of the achieved results.

For the analysis, both S-parameters of an ideally matched and lossless LNA and a 180° hybrid, as well as their real measured S-parameters were considered. All T_{21} measurements were generated in a Matlab environment using (4.2.2).

To evaluate uncertainty propagation through the calibration/correction process the Monte Carlo simulations (MCS) were employed, see Appendix B. Note that the errors in characterization (true) data and in simulated measurements of calibration standards were assumed to be uncorrelated for each standard, as well as among different calibration standards. Nevertheless, the full variance-covariance matrices corresponding to both true data of standards and measured data of standards/DUTs were assumed.

The analysis was performed under the assumptions of frequency independent and normally distributed uncertainties. The author is aware that the assumption of Gaussian distribution does not have to be met in practice, but it is not considered as a problem since the goal of this section is to analyze interferometric approaches from an uncertainty propagation point of view and not to compute exact values of $\mathbf{V}(\Gamma_{\text{x}})$. Moreover, frequency independent uncertainties better reveal the influence of the real **IB** and **AB** hardware.

Due to the assumption of Gaussian distribution of all uncertainties, it was decided to evaluate the "complex" uncertainty in terms of the main semi-major axes of computed ellipses as one "worst-case" factor determining the uncertainty in a complex plane and, subsequently, use this uncertainty for comparison purposes. The eigendecomposition of

Table 4.6: Uncertainties definition

Complex uncertainty	Covariance matrix	Description
u_{VNA}	$\mathbf{V}^{\mathrm{VNA}}$	Measurement uncertainty caused by VNA receiver
u_S	$\mathbf{V}^S(\Gamma_{\mathrm{x}})$	Cal. standard uncertainty
u_{MR}	$\mathbf{V}^{\mathrm{MR}}(\Gamma_{\mathrm{x}})$	Mounting repeatability
u_{DUT}	$\mathbf{V}(\Gamma_{\mathrm{x}})$	Resulting DUT uncertainty
u_{N}	$\mathbf{V}(N_{\mathrm{H}})$	Uncertainty given by phase noise

the variance-covariance matrices $\mathbf{V}(Y)$ was used to extract the semi-major axes of ellipses and, subsequently, to determine the "complex" uncertainties u.

In this analysis author specifically includes the uncertainty given by the phase noise in the VNA test channel N_{H} expressed by u_{N}, the measurement uncertainty caused by the VNA reference channel and the VNA receiver in the test channel expressed by u_{VNA}, the finite mounting repeatability of standard/DUT connections expressed by u_{MR}, and the uncertainty caused by the characterization of the calibration standards expressed by u_S. Table 4.6 summarizes all considered uncertainties and their expression using variance-covariance matrices.

4.2.1 Calibration standards

Calibration/verification and reference standards are necessary part of every measurement and need to be developed for each particular measurement with respect to intended measured DUTs. Further, an application of interferometric approaches requires at least three fully known calibration standards and one reference standard and all must have impedances corresponding to a measured extreme impedance, see Figure 4.22. Therefore, common calibration standard *Open*, *Short*, *Match* cannot be used. Moreover, calibration standards need to be characterized very precisely in order to achieve better measurement accuracy in contrast to common one-port reflection coefficient measurement. To find out achievable precision of the calibration standards characterization calibration standards realizing extremely high impedances were developed and fabricated.

Different configurations of calibration standards realizing extreme impedances were assumed and studied from various points of view, see [37, 38]. Since there are extremely small distinctions in reflected waves from measured DUTs in the area of extreme impedances on 50-Ω transmission lines one of the most significant parameters is the mounting repeatability of calibration standards themselves. As a suitable structure for the design of calibration standards the closed coaxial structure based on microwave connector APC-7, with expected mounting repeatability in the order of 10^{-4}, was chosen. Calibration standards realized by fused silica coaxial line with deposited Cr-Ni resistive strips seemed to be the best solution, see [39].

Subsequent fabrication of calibration standards revealed another very critical factor

and that was the insufficient precision of used technology which causes the standards to exhibit partly random behavior in the amplitude of the reflection coefficient, see [40]. Therefore, the characterization of fabricated standards cannot be, as initially intended, based on precisely measured dimensions and parameters of FS coaxial line with deposited resistive strips and subsequent simulation of the EM model in CST or ANSYS HFSS. In conclusion, these results make impossible to perform real accurate measurements of extremely high impedances.

4.2.2 Calibration/correction process

This section clarifies the influence of the calibration/correction process on the resulting u_{DUT} of all DUTs depicted in Figure 4.22. First, two sensitivity coefficients W_{MR} and W_S examining u_{MR} and u_S propagation, respectively, through the calibration/correction process are defined:

$$\begin{aligned} W_{\mathrm{MR}} &= \left.\frac{u_{\mathrm{DUT}}}{u_{\mathrm{MR}}}\right|_{u_{\mathrm{S}}=u_{\mathrm{VNA}}=u_{\mathrm{N}}=0} \\ W_S &= \left.\frac{u_{\mathrm{DUT}}}{u_{\mathrm{S}}}\right|_{u_{\mathrm{MR}}=u_{\mathrm{VNA}}=u_{\mathrm{N}}=0} \end{aligned} \tag{4.2.3}$$

Coefficients W_{MR} and W_S simply compare the resulting DUT measurement uncertainty u_{DUT} with uncertainties u_{MR} and u_S, respectively, under the condition that all remaining uncertainties are zero. Figure 4.23 shows the resulting W_{MR} and W_S, given by the choice of calibration standards $S_1 = 5\ \mathrm{k\Omega}, S_2 = 10\ \mathrm{k\Omega}, S_3 = 42\ \mathrm{k\Omega}$ and reference standard/impedance $Z_{\mathrm{ref}} = 92\ \mathrm{k\Omega}$.

Both coefficients W_{MR} and W_S are determined by equations for calibration and correction only. They do not depend either on **IB** and **AB** hardware parameters or the frequency chosen. It can be seen in Figure 4.23 that W_S is approx. equal or higher than one and W_{MR} is approx. equal or higher than 1.25 which means that the interferometric method cannot suppress uncertainties u_{MR} and u_S. Both u_{MR} and u_S limit achievable measurement accuracy during absolute measurements and, moreover, their influence on the resulting u_{DUT} depends on the DUT position with respect to calibration standards.

Further, it was found that the location of calibration standards significantly influences the interferometric method performance contrary to the reference impedance location. Calibration standards uniformly distributed over the supposed measured impedance area seems to be the best solution.

Second, achievable suppression of measurement uncertainty u_{VNA} and uncertainty given by presence of phase noise u_{N} for ideal hardware (Ideal 180° hybrid – $A = 2$, ideal amplifier – $G = 30$) is analyzed under the assumption that other remaining uncertainties are zero. Suppression coefficients S^{VNA} and S^{Noise} comparing u_{VNA} and u_{N}, respectively, with the resulting u_{DUT} are simply defined, see (4.2.4). Notice that coefficients S^{VNA} and S^{Noise} are defined in reverse with respect to the definition of sensitivity coefficients W_{MR} and W_S in (4.2.3) since S^{VNA} and S^{Noise} express uncertainty suppression whereas W_{MR} and W_S express an uncertainty increase.

$$\begin{aligned} S^{\mathrm{VNA}} &= \left.\frac{u_{\mathrm{VNA}}}{u_{\mathrm{DUT}}}\right|_{u_{\mathrm{MR}}=u_{\mathrm{S}}=u_{\mathrm{N}}=0} \\ S^{\mathrm{Noise}} &= \left.\frac{u_{\mathrm{N}}}{u_{\mathrm{DUT}}}\right|_{u_{\mathrm{MR}}=u_{\mathrm{S}}=u_{\mathrm{VNA}}=0} \end{aligned} \tag{4.2.4}$$

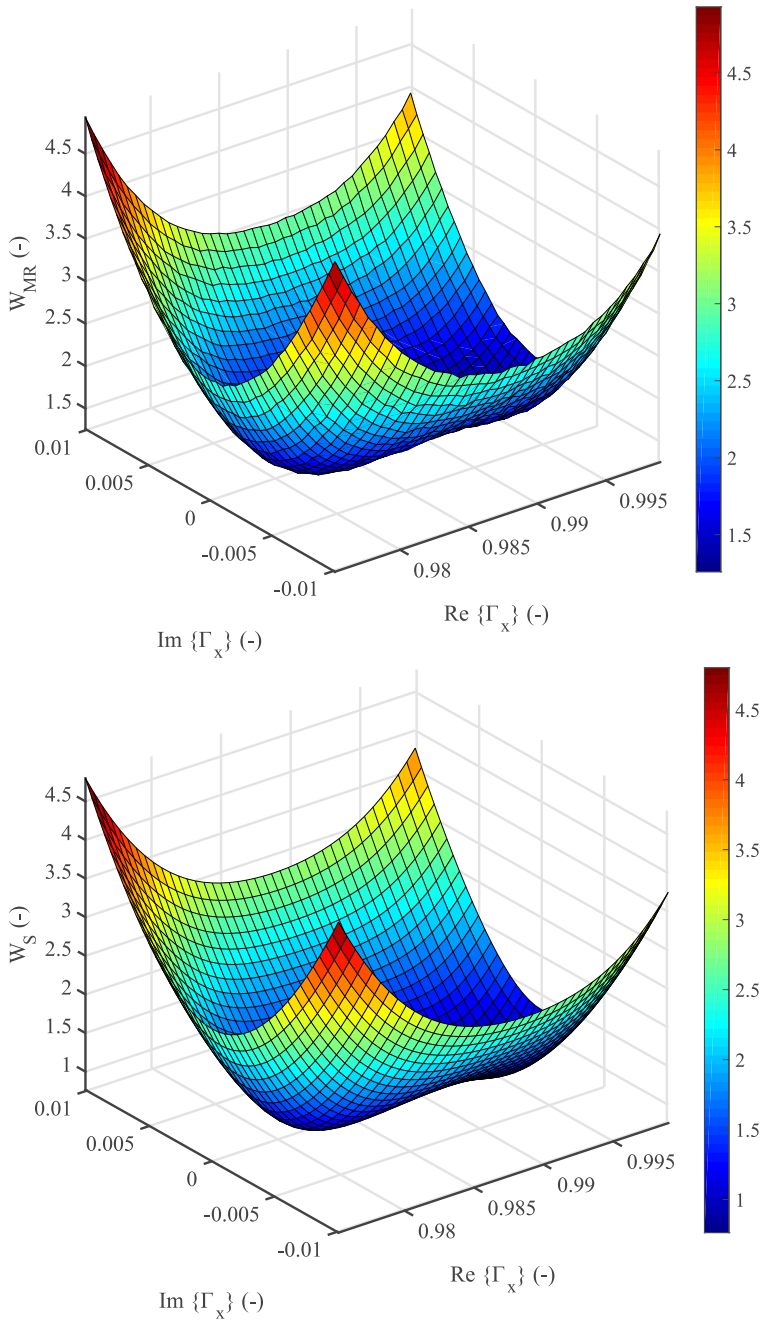

Figure 4.23: Coefficients W_{MR} and W_{S} corresponding to a scenario – $S_1 = 5\ k\Omega$, $S_2 = 10\ k\Omega$, $S_3 = 42\ k\Omega$, and $Z_{\mathrm{ref}} = 92\ k\Omega$.

S^{VNA} is an equivalent to SL^{HW}, (3.2.22), suppressing $\mathbf{V}^{\mathrm{VNA}}$ determined predominantly by the phase noise in the VNA reference channel, see (3.2.21). S^{Noise} is an equivalent to SL^{IB}, (3.2.23), suppressing high-level multiplicative noise $\mathbf{V}(N_{\mathrm{H}})$ and low-level additive noise $\mathbf{V}(N_{\mathrm{L}})$ in the VNA test channel, see (3.2.21). Figure 4.24 shows the achieved S^{VNA} and S^{Noise} for ideal **IB** and **AB** hardware.

S^{VNA} should be directly proportional to the gain of **AB**, nevertheless, the results in Figure 4.24 show that S^{VNA} is also function of DUT position. Moreover, the achieved

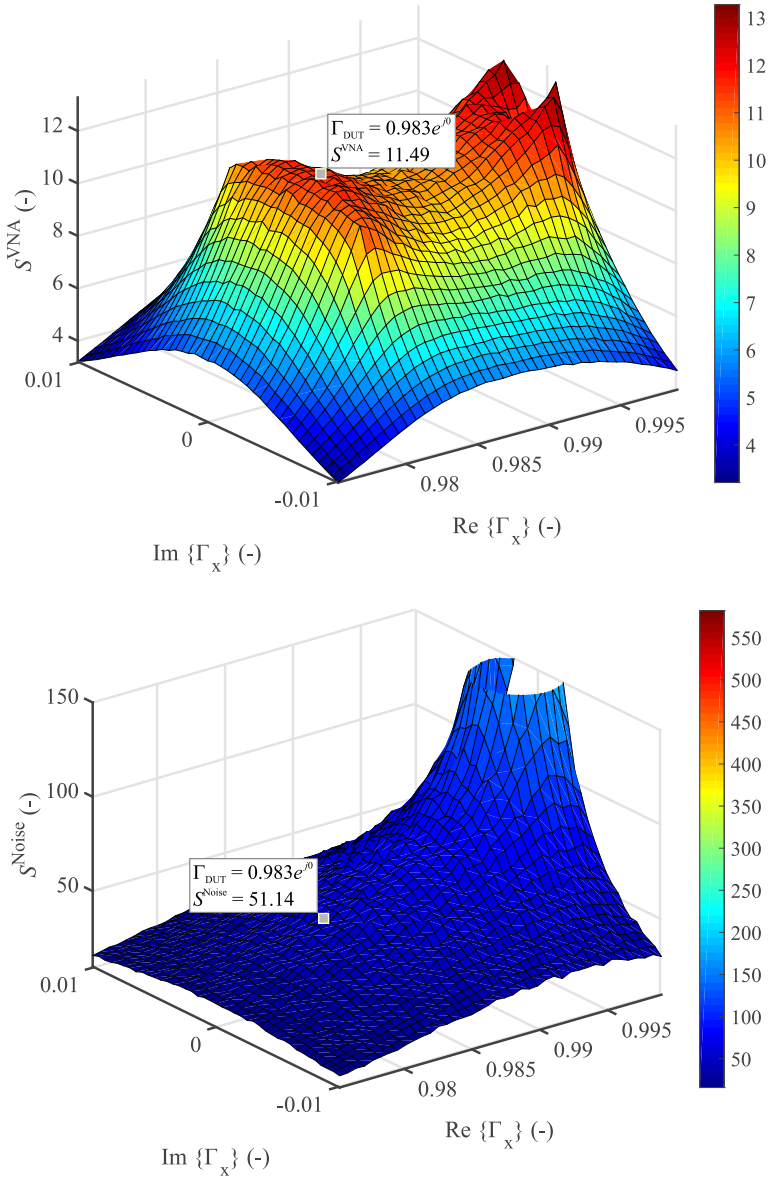

*Figure 4.24: Resulting suppression coefficients corresponding to ideal **IB** and **AB** hardware and the scenario ($S_1 = 5\ k\Omega$, $S_2 = 10\ k\Omega$, $S_3 = 42\ k\Omega$, and $Z_{ref} = 92\ k\Omega$): S^{VNA} expressing the achieved u_{VNA} suppression and S^{Noise} expressing the achieved u_N suppression.*

S^{VNA} is smaller than the theoretical limit $SL^{HW} = 15$, computed using (3.2.22), even for ideal **IB** and **AB** hardware due to the influence of the calibration/correction process, see W_{MR} and W_S in Figure 4.23.

The achieved suppression of multiplicative (phase) noise S^{Noise} is inversely proportional to the subtractive signal Δ that is directly given by the differences between Z_{ref} and measured DUTs in the case of ideal **IB**. Therefore, S^{Noise} is highest for DUTs close to the reference impedance Z_{ref}. The phase noise suppression improves VNA measurement stability, and, thus, S^{Noise} is an extremely important parameter in the case of relative measurements where u_{MR} and u_S do not influence the measurement.

In conclusion, the calibration/correction process, together with the choice of calibration and reference standards, strongly influences the propagation of uncertainties u_{MR}, u_S, and u_{VNA}, whereas the propagation of u_{N} is primarily given by the choice of reference impedance Z_{ref} and **IB** hardware. Finally, the contribution of all uncertainties into the resulting u_{DUT} is a function of DUT position towards calibration and reference standards.

4.2.3 Real hardware

The goal of this section is to show resulting u_{DUT} dependence on the properties of real hardware. For uncertainty analysis, the microwave coaxial connectors APC-7 were chosen because of their superior mounting repeatability among other coaxial connectors. This connector should be able to achieve repeatability of return loss $|\Delta S_{11}| = 78$ dB according to the IEEE standard for precision coaxial connectors [42] which is approx. $2{\cdot}10^{-4}$ in linear scale, therefore, $u_{\mathrm{MR}} = 3.3 \cdot 10^{-5}$ under the assumption that $|\Delta S_{11}| = 6 \cdot u_{\mathrm{MR}}$. Further, calibration standard uncertainty u_{S} is assumed to be the same as u_{MR}. In an ideal case u_{S} should be at least one order smaller than u_{MR} in order not to contribute to the resulting u_{DUT}. Finally, the uncertainty caused by phase noise $u_{\mathrm{N}} = 0.0003/3$ (approx. -70 dB), which corresponds to the IF bandwidth IF = 10 kHz, and $u_{\mathrm{VNA}} = 0.002$ are assumed.

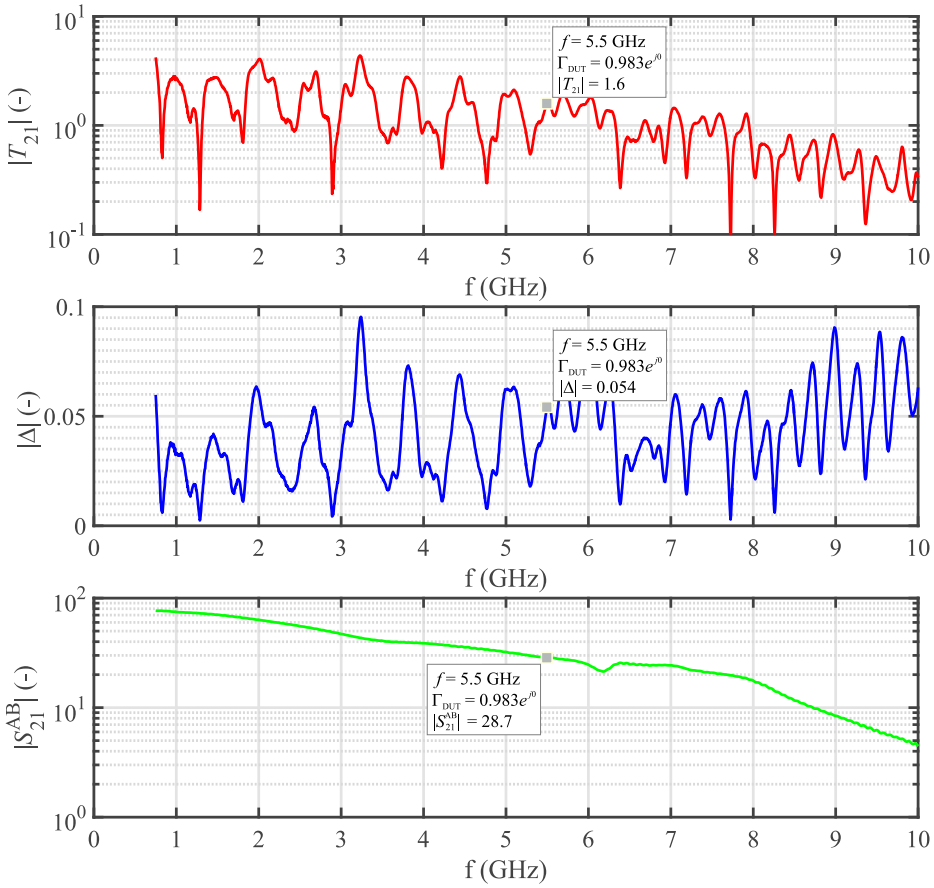

*Figure 4.25: Synthetically generated measurement employing measured S-parameters of 180° Hybrid and a cascade of three amplifiers for the chosen DUT: Transmission coefficient $|T_{21}|$; Subtractive signal $|\Delta|$ created by the **IB**; Parameter $\left|S_{21}^{\mathrm{AB}}\right|$ of the **AB**.*

The measured S-parameters of 180° hybrid (*ET Industries - model J-0776-180*) and a cascade of three amplifiers (*Mini-Circuits - ZX60-8008E-S+, Gali-1+, Gali-2+*) were used for the T_{21} generation in the Matlab environment. Figure 4.25 shows a synthetically derived $|T_{21}|$ measurement, corresponding subtractive signal $|\Delta|$, and parameter $\left|S_{21}^{\mathrm{AB}}\right|$. The generated data correspond to a chosen DUT with an impedance value of 5.9 kΩ ($\Gamma_{\mathrm{x}} = 0.983$) and the same choice of calibration and reference standards as in the previous section – $S_1 = 5$ kΩ, $S_2 = 10$ kΩ, $S_3 = 42$ kΩ and $Z_{\mathrm{ref}} \cong 92$ kΩ ($\Gamma_{\mathrm{ref}} \cong 0.999$).

The real **IB** limits achievable $|\Delta|$ due to its parasitic properties, namely the internal transmission between **IB** respective ports 1 and 2, see Figure 3.8. Therefore, $|\Delta|$ values in Figure 4.25 are, in most cases, higher than the differences between the chosen Γ_{ref} and Γ_{x} (DUT) that is approx. 0.016 in this particular case. Moreover, the parameter A of a real **IB** fluctuates between values 2 and 4 for the real 180° hybrid and the real **AB** has frequency dependent gain G.

For comparative purposes, frequency 5.5 GHz was selected to depict the resulting S^{VNA}, S^{Noise}, and U_{DUT} corresponding to coverage factor value of three, see Figure 4.26 and Figure 4.27. In this case the cascade of three amplifiers has comparable gain $|G| \cong 29$ with the gain $G = 30$ of ideal **AB** hardware used in previous Section 4.2.2.

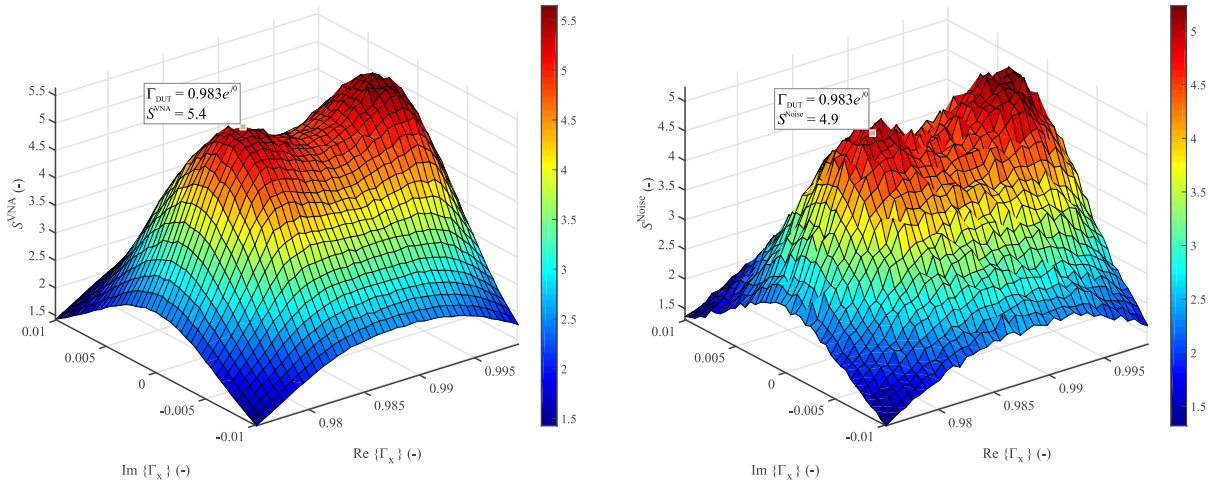

*Figure 4.26: Resulting suppression coefficients corresponding to the scenario ($S_1 = 5$ kΩ, $S_2 = 10$ kΩ, $S_3 = 42$ kΩ, and $Z_{\mathrm{ref}} = 92$ kΩ), with frequency value of 5.5 GHz, and the real **IB** and **AB** hardware – a cascade of three amplifiers ($G \cong 30$) and a real 180° hybrid: a) S^{VNA} expressing the u_{VNA} suppression; b) S^{Noise} expressing u_{N} suppression.*

The achieved S^{VNA} in Figure 4.26 is smaller than S^{VNA} for the ideal hardware in Section 4.2.2. Specifically, for the DUT with an impedance value of 5.9 kΩ ($\Gamma_{\mathrm{x}} = 0.983$) the value of $S^{\mathrm{VNA}} = 5.4$ is approx. two times smaller than $S^{\mathrm{VNA}} = 11.49$ for ideal hardware. This indicates higher losses A caused by nonideal properties of the 180° hybrid used, see the equation (3.2.22) for SL^{HW} that is equivalent to S^{VNA}. On the other hand, the achieved S^{Noise} in Figure 4.26 is dramatically smaller in contrast to S^{Noise} for the ideal hardware in Section 4.2.2 due to the above mentioned parasitic properties of real **IB** and higher losses A. Namely, for the DUT with an impedance value of 5.9 kΩ ($\Gamma_{\mathrm{x}} = 0.983$) the value of the subtractive signal is $|\Delta| = 0.054$, see Figure 4.25, and the value of $S^{\mathrm{Noise}} = 4.9$, see Figure 4.26. The achieved S^{Noise} is approx. ten times smaller than $S^{\mathrm{Noise}} = 51$ for ideal hardware.

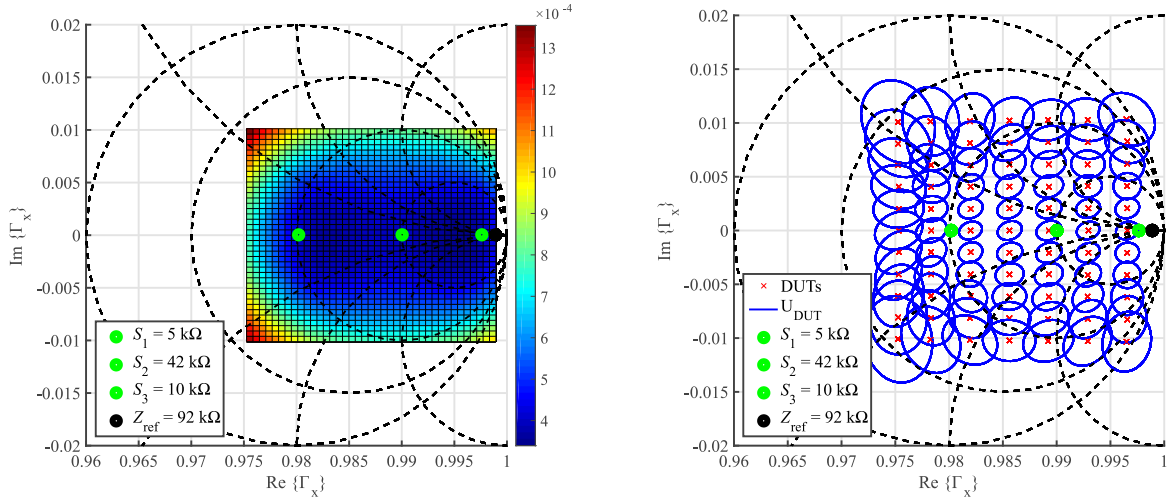

*Figure 4.27: Resulting u_{DUT} corresponding to the scenario ($S_1 = 5\ k\Omega$, $S_2 = 10\ k\Omega$, $S_3 = 42\ k\Omega$, and $Z_{\mathrm{ref}} = 92\ k\Omega$), the chosen frequency 5.5 GHz and real **IB** and **AB** hardware – a cascade of three amplifiers ($G \cong 30$) and a real 180° hybrid: a) u_{DUT} expressed by color map; b) U_{DUT}, describing 99% confidence intervals, expressed in the form of ellipses.*

Figure 4.27 shows an example of the resulting measurement uncertainty of chosen DUTs at 5.5 GHz in the form of a color map and ellipses illustrating 99% confidence intervals.

It can be clearly seen that the interferometric method works only for a small range of DUTs with very similar impedances to the chosen calibration standards and reference impedance. The best achieved u_{DUT} is slightly higher than $u_{\mathrm{S}} = u_{\mathrm{MR}} = 0.0002/6$ that cannot be suppressed by the method itself. On the other hand, both u_{VNA} and u_{N} were suppressed approx. five times even with a 180° hybrid with high parasitic transmission at 5 GHz.

Finally, Figure 4.28 shows the broadband frequency behavior of the resulting uncertainty u_{DUT} for the chosen DUT = 5.9 kΩ. It can be seen that the resulting u_{DUT} is higher at all frequencies than u_{MR} and u_{S} that cannot be suppressed by the interferometric method itself. Further, u_{DUT} is smallest at low frequencies due to the high gain of the cascade of three amplifiers, see Figure 4.25, that implies high S^{VNA} expressing suppression of u_{VNA}. At high frequencies $u_{\mathrm{DUT}} \cong u_{\mathrm{VNA}}$ since the method stops working because of the small gain of the cascade of three amplifiers.

In conclusion, it should be noted that the results correspond to frequency independent and, moreover, idealized parameters of calibration standards and DUTs. Such a behavior of calibration standards and DUTs cannot be met in practice and was used only for illustrative purposes. Nevertheless, it does not have impact on generality of achieved results. On the other hand, real measured S-parameters of **IB** and **AB** hardware were used to reveal the real uncertainty propagation. Note, that the interferometric method will work with any frequency dependence of calibration/reference standards and DUTs as far as they all show the same frequency dependent parameters.

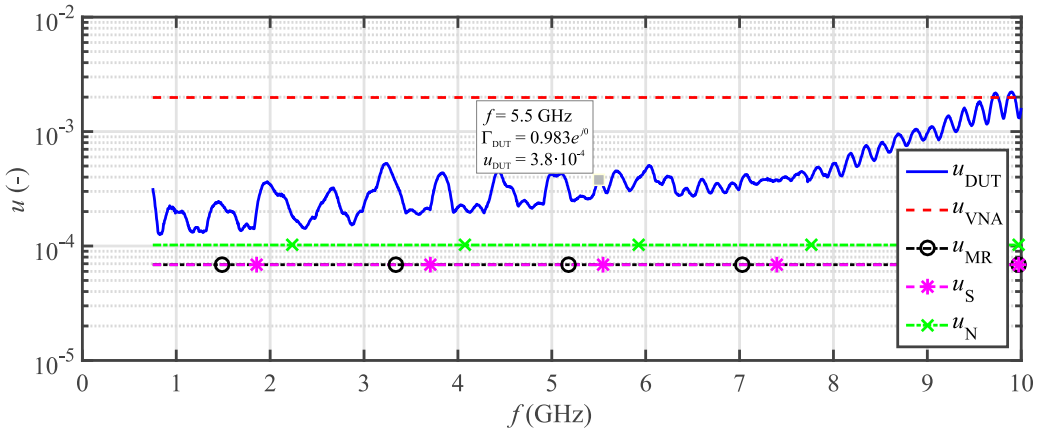

Figure 4.28: Resulting frequency dependent DUT uncertainty u_{DUT} with respect to other uncertainties $u_{\mathrm{VNA}}, u_{\mathrm{MR}}, u_{\mathrm{S}}$, and u_{N}.

5 Conclusion

The objectives of the thesis were accomplished and achieved as follows.

First, microwave measurement approaches for characterization of RFI/EMI filters in their stop band were studied and, subsequently, a new method (called Γ_{opt} method) based on measured S-parameters evaluation was developed, experimentally verified on a cascade of single-ended coaxial filters in the frequency range from 6 to 12 GHz and finally applied to the characterization of a professional three-wire RFI/EMI filter in the frequency range from 1 to 10 GHz. The Γ_{opt} method reliably and unambiguously determines the real worst-case behavior (i.e., minimum insertion loss) of a single-ended filter in its stop band independent of its terminating impedances. Validity of the Γ_{opt} method was verified by experimental measurements where the worst-case power-line and load impedances for single-ended coaxial filter were realized using microwave tuners.

When applying the Γ_{opt} method on a three-wire RFI/EMI filter all common mode (CM), differential mode (DM), and their mutual conversions CM→DM and DM→CM propagating inside its structure were taken into an account and evaluated separately. To evaluate worst-case behavior of all modes and their conversions two approaches were developed.

First approach was solved by the AWR Microwave Office (AWR MO) simulator using a model crated by a cascade consisting of a measured four-port single-ended filter S-matrix and two ideal in-phase and out-of-phase power divides $\mathrm{PD_a}$ and $\mathrm{PD_b}$. By using this technique, all important parameters including CM, DM, CM→DM, and DM→CM were evaluated and, subsequently, minimum insertion losses $IL_{\mathrm{minCC}}, IL_{\mathrm{minDD}}, IL_{\mathrm{minDC}}$, and IL_{minCD} were determined using developed Γ_{opt} method. All obtained results show that the minimum insertion loss values can be even more than 20 dB lower compared to insertion loss values corresponding to standard mixed-mode reference impedances. Nevertheless, this approach neglects reflections of converted modes and do not take possibility of their reflections back into the filter structure. Therefore, the second approach based on application of Γ_{opt} method on parametrized degenerated two-port S-matrices, derived from mixed-mode filter S-matrix, was developed. A single equation describing the individual elements of all degenerated two-port S-matrices was derived. Results show that considering 100 % reflections of the converted modes, causes worst-case minimum insertion losses IL^{ji}_{minW} more than 20 dB lower than the corresponding values achieved with the first approach. The occurrence of this phenomenon is high and considering this effect is important in practice.

Second, microwave interferometric measurement methods, based on two-port VNA measurements, of extreme impedances were studied and analyzed in order to clarify the phenomenon of interference on resulting measurement precision and accuracy and to show basic limits and give general recommendations for practical measurements. A general transmission coefficient T^{G}_{21}, describing interferometric measurements, depending on the interferometric box (**IB**) and amplification box (**AB**) hardware and different noise sources present in the VNA test and reference channel was developed. The law of uncertainty propagation was used to analyze simplified transmission coefficient T'_{21} in order to show what mechanisms are behind the suppression of uncertainties and what are the most important **IB** and **AB** parameters influencing resulting DUT measurement uncertainty. Finally, a virtual measurements, employing real measured S-parameters of 180° hybrid and

a cascade of three amplifiers, in combination with Monte Carlo simulations (MCS) were used to verify and extend previously achieved results. Results show that interferometric methods can improve measurement accuracy by suppressing noise sources in both the VNA test and reference channel. Specifically, they suppress the phase noise u_{N} and the noise floor in the VNA test channel and u_{VNA} representing the influence of the VNA reference channel and VNA receiver in the test channel. Consequently, the microwave measurement employing interferometric methods improves measurement accuracy only if the u_{N} or u_{VNA} dominate over the mounting repeatability of the connection u_{MR} and calibration standard characterization u_{S}. In such a case, it is possible to use a wide IF bandwidth, perform fast measurements, and, at the same time, achieve comparable or even better measurement accuracy in contrast to a precise common one-port measurement. It was also discovered that in the case of relative measurements, where u_{N} is the most limiting factor, it is important to have **IB** hardware that will not limit the subtractive signal Δ created by the signal corresponding to the measured coefficient Γ_{x} and any interfering reference signal S_{ref}. Nevertheless, the amplified subtractive signal must always be higher than the noise generated at the output of **AB**. On the other hand, to achieve the best measurement accuracy during absolute measurements, the parameters of both **AB** and **IB** must be wisely chosen with respect to other limiting factors given mainly by the mounting repeatability of the connection u_{MR} used and the uncertainty of calibration standards characterization u_{S}.

5.1 Author's contribution

Summarization of the most important author's results related to objectives of the thesis:

RFI/EMI filters

- New method (Γ_{opt} method) determining the worst-case behavior (i.e., minimum insertion loss) of single-ended filters in their stop band was developed.
- Γ_{opt} method was experimentally verified on a cascade of single-ended coaxial filters in the frequency range from 6 to 12 GHz.
- An advanced approach, combining the Γ_{opt} method with CM/DM analysis of a filter and an optimization, for determining the worst-case behavior of three-wire RFI/EMI filters in their stop band was developed and applied on professional SKY1FL16DMA2 (SKYBERGTECH) single-phase three-wire (European standard) interference filter.

Interferometric measurements of extreme impedances

- A measurement model, describing interferometric measurements of extreme impedances, including all important sources of uncertainty in both the VNA test and reference channel was developed and general transmission coefficient was derived.
- An analytical solution of uncertainty propagation, illustrating the phenomenon of uncertainty suppression and basic limits influencing the achievable measurement precision and accuracy, was derived for partly simplified transmission coeficient.

- Virtual measurements employing MCS were performed to confirm the derived theory and ascertain the influence of calibration standards and real interferometric hardware on the resulting DUT uncertainty.

5.2 Recommendations for future work

The thesis provides theory for finding the worst-case behavior (i.e., minimum insertion loss) of professional three-wire RFI/EMI filters. Nevertheless, for practical applications is necessary to experimentally verify what are the real impedances or reflection coefficients realized by standard power-lines connected to the filter. Further, a theory necessary for evaluation of three-phase fife-wire RFI/EMI filters or, generally, more than three-wire filters is still missing and need to be derived.

The thesis also provides theoretical background for microwave interferometric measurement methods suitable for extreme impedances measurement. There is still one step missing in these measurements and that is an experimental validation of measurement accuracy and, subsequent, comparison with measurement accuracy of common one-port reflection coefficient measurement. To verify achievable measurement accuracy calibration and reference standards, precisely characterized, must be developed and fabricated.

6 Appendices

A Example of partial derivative computation

The partial derivative of $T_{21}^{'}$ in (3.2.7), with respect to Γ_{x}, equals

$$\frac{\partial T_{21}^{'}}{\partial \Gamma_x} = \frac{\partial \left(\frac{a_1}{a_{1\mathrm{R}}} \frac{G}{A} e^{j\varphi} \Gamma_{\mathrm{x}} \right)}{\partial \Gamma_{\mathrm{x}}} \tag{A.1}$$

since the terms $GS_{\mathrm{ref}}, GN_{\mathrm{L}}^{\mathrm{IB}}$, $N_{\mathrm{L}}^{\mathrm{AB}}$, and $N_{\mathrm{L}}^{\mathrm{T}}$ in (3.2.7) are not a function of Γ_{x} and $N_{\mathrm{H}} a_1 + N_{\mathrm{L}} = a_1$ for the mean values of N_{H} and N_{L}. Further,

$$\Gamma_{\mathrm{x}} = a + jb, \tag{A.2}$$

and

$$e^{j[\varphi + \arg(G/A) + \arg(a_1/a_{1\mathrm{R}})]} = e^{j\Phi} = x + jy \tag{A.3}$$

are defined and, subsequently, substituted into the numerator of (A.1):

$$\begin{gathered} \frac{a_1}{a_{1\mathrm{R}}} \frac{G}{A} e^{j\varphi} \Gamma_{\mathrm{x}} = \\ = \frac{|a_1|}{|a_{1\mathrm{R}}|} \frac{|G|}{A} \left[(xa - yb) + j\left(xb + ya \right) \right] = f_1 + j f_2 \end{gathered} . \tag{A.4}$$

Now the partial derivative of $T_{21}^{'}$, with respect to Γ_{x}, can be computed using:

$$\left(\frac{\partial T_{21}^{'}}{\partial \Gamma_{\mathrm{x}}} \right) = \begin{pmatrix} \frac{\partial f_1}{\partial a} & \frac{\partial f_1}{\partial b} \\ \frac{\partial f_2}{\partial a} & \frac{\partial f_2}{\partial b} \end{pmatrix} = \frac{|a_1|}{|a_{1\mathrm{R}}|} \frac{|G|}{A} \begin{pmatrix} x & -y \\ y & x \end{pmatrix}. \tag{A.5}$$

Further, the first term in (3.2.15) in Section 3.2.2 equals to

$$\begin{gathered} \left(\frac{\partial T_{21}^{'}}{\partial \Gamma_{\mathrm{x}}} \right) \mathbf{V}^{\mathrm{MR}} \left(\Gamma_{\mathrm{x}} \right) \left(\frac{\partial T_{21}^{'}}{\partial \Gamma_{\mathrm{x}}} \right)^{\mathrm{T}} = \\ = \frac{|a_1|^2}{|a_{1\mathrm{R}}|^2} \frac{|G|^2}{A^2} \begin{pmatrix} x & -y \\ y & x \end{pmatrix} \mathbf{V}^{\mathrm{MR}} \left(\Gamma_{\mathrm{x}} \right) \begin{pmatrix} x & -y \\ y & x \end{pmatrix}^{\mathrm{T}} = \\ = \frac{|a_1|^2}{|a_{1\mathrm{R}}|^2} \frac{|G|^2}{A^2} \tilde{\mathbf{V}}^{\mathrm{MR}} \left(\Gamma_{\mathrm{x}} \right) \end{gathered} , \tag{A.6}$$

where matrix

$$\begin{pmatrix} x & -y \\ y & x \end{pmatrix} \approx x + jy = e^{j\Phi} = \cos\Phi + j \sin\Phi \tag{A.7}$$

is a matrix representation of the complex number $x + jy$ and represents a rotation matrix in (A.6). $\tilde{\mathbf{V}}^{\mathrm{MR}} \left(\Gamma_{\mathrm{x}} \right)$ expresses the rotation of the joint probability distribution (an ellipse), given by $\mathbf{V}^{\mathrm{MR}} \left(\Gamma_{\mathrm{x}} \right)$. The rotation is given by the parameter $\Phi = \varphi + \arg\left(G/A \right) + \arg\left(a_1/a_{1\mathrm{R}} \right)$, see Figure 6.1.

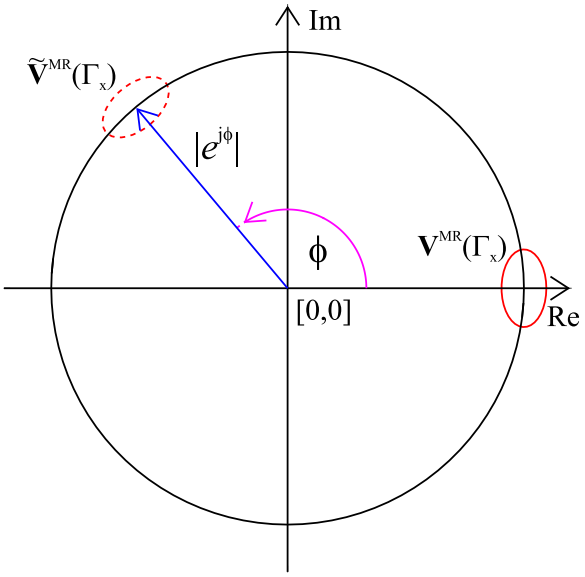

Figure 6.1: Illustration of variance-covariance matrix $\mathbf{V}(\Gamma_{\mathrm{x}})$ *rotation in Re-Im plane.*

B Monte Carlo Simulations (MCS)

To perform MCS at one frequency point three calibration standards having a bivariate Gaussian distribution $S_i \sim N_2(\mu_{S_i}, \mathbf{V}(S_i))$, where $i = 1, 2, 3$ must be defined. The parameter μ_{S_i} denotes population mean vector, and $\mathbf{V}(S_i)$ stand for population variance-covariance matrix. All calibration standards S_i are represented as two large software-generated random samples s_i^{S} and s_i^{MR} each of $N = 1 \cdot 10^4$ observations

$$\begin{aligned} s_i^{\mathrm{S}} &= \left(s_{i1}^{\mathrm{S}}, s_{i2}^{\mathrm{S}}, \ldots, s_{ij}^{\mathrm{S}}, \ldots, s_{iN}^{\mathrm{S}}\right) \\ s_i^{\mathrm{MR}} &= \left(s_{i1}^{\mathrm{MR}}, s_{i2}^{\mathrm{MR}}, \ldots, s_{ij}^{\mathrm{MR}}, \ldots, s_{iN}^{\mathrm{MR}}\right) \end{aligned}, \tag{B.1}$$

where $j = 1, 2, \ldots, N$. s_i^{S} is an estimate of the quantity $S_i \sim N_2\left(\mu_{S_i}, \mathbf{V}^{\mathrm{S}}(S_i)\right)$ including uncertainty caused by the characterization of calibration standard u_s and is used for calibration constants computation. s_i^{MR} stands for an estimate of the quantity $S_i \sim N_2\left(\mu_{S_i}, \mathbf{V}^{\mathrm{MR}}(S_i)\right)$, including the uncertainty caused by mounting repeatability u_{MR}, and is used for the generation of measured values.

Further, estimates m_i of calibration standards measurements $M_i \sim N_2(\mu_{M_i}, \mathbf{V}(M_i))$ are derived using

$$m_i = S_{21}^{\mathrm{IB}'} S_{21}^{\mathrm{AB}'} n_i + \varepsilon_i, \tag{B.2}$$

where $n_i = (n_{i1}, n_{i2}, \ldots, n_{ij}, \ldots, n_{iN})$ is an estimate of phase noise $N_{\mathrm{H}} \sim N_2(1, \mathbf{V}(N_{\mathrm{H}}))$ described by the unity mean vector and variance-covariance matrix $\mathbf{V}(N_{\mathrm{H}})$ expressing u_{N}. $\varepsilon_i = (\varepsilon_{i1}, \varepsilon_{i2}, \ldots, \varepsilon_{ij}, \ldots, \varepsilon_{iN})$ is an estimate of uncertainty u_{VNA} having $N_2\left(0, \mathbf{V}^{\mathrm{VNA}}\right)$. $\mathbf{V}^{\mathrm{VNA}}$ is mainly caused by the phase noise in the VNA reference channel and must be assigned to each derived m_i. The product $S_{21}^{\mathrm{IB}'} S_{21}^{\mathrm{AB}'}$ in (B.2) is a function of Γ_{x}, see (3.2.2)-(3.2.4). For generation m_i a substitution $\Gamma_{\mathrm{x}} = s_i^{\mathrm{MR}}$ was used since the mounting repeatability always influences the measured data.

In the next step, estimates c_i of calibration constants C_i are computed from three equations given by the error model:

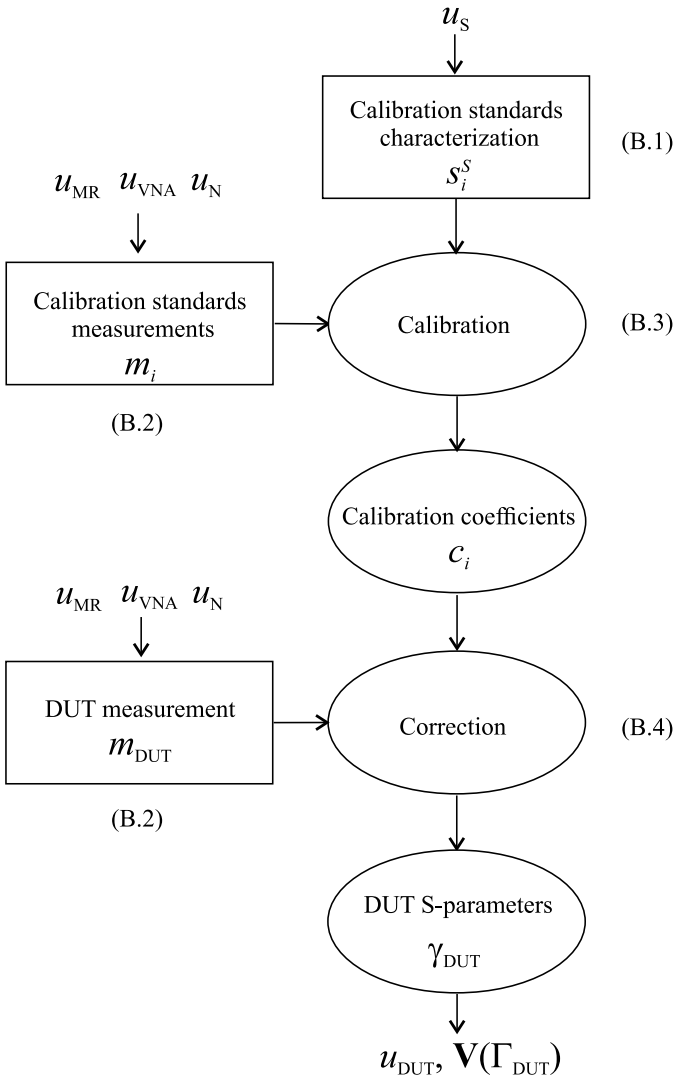

Figure 6.2: Flow chart describing the computation of the resulting uncertainty u_{DUT} using MCS.

$$m_i = \frac{c_1 + c_2 s_i^{\mathrm{S}}}{1 - c_3 s_i^{\mathrm{S}}}. \tag{B.3}$$

Subsequently, to perform the verification process it is necessary to first generate an estimate m_{DUT} of quantity M_{DUT}, expressing the DUT measurement, using the same procedure as for m_i. Further, an estimate γ_{DUT} of the reflection coefficient Γ_{DUT} of the measured DUT is evaluated using:

$$\gamma_{\mathrm{DUT}} = \frac{m_{\mathrm{DUT}} - c_1}{c_2 + c_3 m_{\mathrm{DUT}}}. \tag{B.4}$$

The last step is to compute a variance-covariance matrix $\mathbf{V}\left(\Gamma_{\mathrm{DUT}}\right)$ in rectangular coordinate system Re-Im and use it for complex uncertainty and ellipse parameters extraction. The whole process is described using the flow chart shown in Figure 6.2.

References

[1] *Methods of measurement of the suppression characteristics of passive EMC filtering devices*, European Standard EN 55017, 2011.

[2] *IEEE Standard for Methods of Measurement of Radio-Frequency Power-Line Interference Filter in the Range of 100 Hz to 10 GHz*, IEEE Electromagnetic Compatibility Society, IEEE Standard 1560-2005, 2006.

[3] *Method of Insertion Loss Measurement*, MIL-STD-220B, 2000.

[4] *Requirements for the Control of Electromagnetic Interference Characteristics of Subsystems and Equipment*, MIL-STD-461E, 1999.

[5] M. Randus, "Methods for measurement of extreme impedances."

[6] M. Randus and K. Hoffman, "A simple method for extreme impedances measurement," *72nd Digest of 2007 ARFTG Int. Conf.*, December 2007.

[7] K. Hoffmann and Z. Skvor, "On radio interference filter measurement," *62nd ARFTG Microw. Meas. Conf.*, pp. 227–231, December 2003.

[8] ——, "First results of microwave measurement of broadband radio interference filters," *64th ARFTG Microw. Meas. Conf.*, pp. 139–142, December 2004.

[9] L. N. R. P. K. Piwowarczyk, M. Wnuk and M. Butan, "Emc filters attenuation measuring method," *PIERS Proc.*, pp. 82–86, March 2012.

[10] J. G. Kraemer, "S-parameter characterization for emi filters," *IEEE Int. Symp. on Electromagn. Compat.*, vol. 1, pp. 361–366, August 2003.

[11] B. Audone and L. Bolla, "Insertion loss of mismatched emi suppressors," *IEEE Trans. Electromagn. Compat.*, vol. EMC-20, no. 3, pp. 384–389, August 1978.

[12] S. M. Vakil, "A technique for determination of filter insertion loss as a function of arbitrary generator and load impedances," *IEEE Trans. Electromagn. Compat.*, vol. EMC-20, no. 3, pp. 273–278, May 1978.

[13] C. Rutherglen, D. Jain, and P. J. Burke, "Rf resistance and inductance of massively parallel single walled carbon nanotubes: Direct, broadband measurements and near perfect 50 ohm impedance matching," *Applied Physics Letters*, vol. 93, no. 8, pp. 1–3, August 2008.

[14] J. M. Salter, N. M. Ridler, and P. M. Harris, "Over-determined calibration schemes for rf network analysers employing generalised distance regression," *62nd ARFTG Microw. Meas. Conf.*, pp. 127–142, December 2003.

[15] J. Hoffmann, P. Leuchtmann, J. Reufenacht, and R. Vahldieck, "A stable bayesian vector network analyzer calibration algorithm," *IEEE Trans. Microw. Theory Techn.*, vol. 57, no. 4, pp. 869–880, November 2009.

[16] Z. Yu, C. Rutherglen, and P. J. Burke, "Scaling of the microwave and dc conductance of metallic single-walled carbon nanotubes," *Nanostructure Integration Techniques for Manufacturable Devices, Circuits, and Systems: Interfaces, Interconnects, and Nanosystems*, vol. 6003, no. 1, pp. 1–7, November 2005.

[17] A. Imtiaz, T. M. Wallis, and P. Kabos, "Near-field scanning microwave microscopy: An emerging research tool for nanoscale metrology," *IEEE Microw. Mag.*, vol. 15, no. 1, pp. 52–64, January 2014.

[18] H. Bakli, K. Haddadi, and T. Lasri, "Interferometric technique for scanning near-field microwave microscopy applications," *IEEE Trans. Instrum. Meas.*, vol. 63, no. 5, pp. 1281–1286, May 2014.

[19] A. Lewandowski, D. LeGolvan, R. A. Ginley, T. M. Wallis, A. Imtiaz, and P. Kabos, "Wideband measurement of extreme impedances with a multistate reflectometer," *72nd ARFTG Microw. Meas. Symp.*, pp. 45–49, December 2008.

[20] H. Happy, K. Haddadi, D. Théron, T. Lasri, and G. Dambrine, "Measurement techniques for rf nanoelectronic devices: New equipment to overcome the problems of impedance and scale mismatch," *IEEE Microw. Mag.*, vol. 15, no. 1, pp. 30–39, January 2014.

[21] F. Mubarak, R. Romano, and M. Spirito, "Evaluation and modeling of measurement resolution of a vector network analyzer for extreme impedance measurements," *86th ARFTG Microw. Meas. Conf.*, pp. 87–89, December 2015.

[22] M. Randus and K. Hoffman, "A simple method for extreme impedances measurement – experimental testing," *72nd ARFTG Microw. Meas. Symp.*, pp. 40–44, December 2008.

[23] M. Haase, K. Hoffmann, and P. Hudec, "General method for characterization of power-line emi/rfi filters based on s-parameter evaluation," *IEEE Trans. Electromagn. Compat.*, vol. 58, no. 5, pp. 1465–1474, July 2016.

[24] ——, "Advanced evaluation of minimum insertion loss of power-line emi/rfi filters in rf and microwave frequency bands," *IEEE Trans. Electromagn. Compat.*, vol. 59, no. 6, pp. 1887–1896, May 2017.

[25] G. Vendelin, *Design of Amplifiers and Oscillators by the S-parameter Method*. New York, NY, USA: Wiley, 1982.

[26] T. T. Ha, *Solid-State Microwave Amplifier Design*. USA: Wiley, 1981.

[27] B. S. W. R. Eisenstadt and B. M. Thompson, *in Microwave Differential Circuit Design Using Mixed-Mode S-Parameters*. Boston, MA, USA: Artech House, 2006.

[28] D. E. Bockelman and W. R. Eisenstadt, "Pure-mode network analyzer for on-wafer measurements of mixed-mode s-parameters of differential circuits," *IEEE Trans. Microw. Theory Techn.*, vol. 45, no. 7, pp. 1071–1077, July 1997.

[29] ——, "Combined differential and common-mode scattering parameters: Theory and simulations," *IEEE Trans. Microw. Theory Techn.*, vol. 43, no. 7, pp. 1530–1539, July 1995.

[30] K. C. Gupta, R. Garg, and R. Chadha, *Computer-Aided Design of Microwave Circuits*. New York, NY, USA: Artech House, 1981.

[31] D. M. Pozar, *Microwave Engineering, 4th edition*. Wiley, 2011.

[32] M. Zeier, J. Hoffmann, P. Hürlimann, J. Rüfenacht, D. Stalder, and M. Wollensack, "Contemporary evaluation of measurement uncertainties in vector network analysis," *Technisches Messen*, vol. 84, no. 5, January 2017.

[33] ——, "Establishing traceability for the measurement of scattering parameters in coaxial line systems," *Metrologia*, vol. 55, no. 1, January 2018.

[34] N. M. Ridler and M. J. Salter, "Evaluating and expressing uncertainty in complex s-parameter measurements," *56th ARFTG Conf. Digest*, pp. 1–13, December 2000.

[35] *Evaluation of Measurement Data – Guide to the expression of uncertainty in measurement*, Joint Committee for Guides in Metrology, JCGM 101:2008, 2008.

[36] *RS ZVA Vector Network Analyzer Specifications*, Rohde and Schwarz GmbH and Co. KG, 2015.

[37] M. Haase and K. Hoffmann, "Study of calibration standards for extreme impedances measurement," *83rd ARFTG Microw. Meas. Conf.*, pp. 1–6, June 2014.

[38] K. H. M. Haase and Z. Skvor, "Microstrip open — problematic calibration standard," *85th ARFTG Microw. Meas. Conf.*, May 2015.

[39] M. Haase and K. Hoffmann, "Calibration/verification standards for measurement of extremely high impedances," *86th ARFTG Microw. Meas. Conf.*, pp. 83–86, December 2015.

[40] K. H. M. Haase and M. Hudlicka, "Traceable high impedance calibration standards," *87th ARFTG Microw. Meas. Conf.*, May 2016.

[41] M. Randus and K. Hoffman, "A method for direct impedance measurement in microwave and millimeter-wave bands," *IEEE Trans. Microw. Theory Techn.*, vol. 59, no. 8, pp. 2123–2130, May 2011.

[42] *IEEE Standard for Precision Coaxial Connectors (DC to 110 Ghz)*, IEEE Instrumentation and Measurement Society, IEEE Standard 287TM-2007, 2007.

List of Figures

List of Tables